POLITECNICO DI MILANO

Facoltà di Ingegneria Industriale

Corso di Laurea in
Ingegneria Meccanica

OPTIMAL FEEDBACK CONTROL OF TURBULENT CHANNEL FLOW THROUGH WALL-BASED SENSORS AND ACTUATORS

Relatore:	**Ing. Francesco BRAGHIN**
Co-relatore:	**Prof. Maurizio QUADRIO**

Tesi di Laurea di:
Daniele CAVAGLIERI Matr. 721285

Anno accademico 2009/2010

A mia nonna

Abstract

The aim of the present work is to assess the performances of feedback control applied to turbulent channel flow for drag reduction by means of wall shear stresses and wall pressure sensors and zero-net-mass-flux blowing/suction MEMS actuators at walls.

The problem is addressed starting from Navier-Stokes equations, which are manipulated in order to obtain a linear time-invariant model of the channel flow. Such model is then exploited in order to implement a full-information LQR controller into Direct Numerical Simulations. The following step concerns the implementation of a more likely measurement-based controller. The design procedure that has been developed is mainly based on optimal output feedback control. Results have indicated the necessity of implementing a state observer.

The following part of the work deals with the design of an optimal compensator based on wall measurements. This phase is carried out leveraging a frequency-based Wiener-Hopf control technique previously developed to reduce the drag in a plane channel flow using a single-input single-output approach. This strategy has then been extended to multi-output configuration, where all wall measurements are available. Simulations with different control penalties and measurement noise have shown that performances decrease, albeit remaining still positive, when an observer is introduced and benefits arising from multiple measurements information concern an improved robustness with respect to measurement noise.

These results have suggested that a linear control approach is sufficient to successfully manipulate a turbulent channel flow, but state estimation must take into account also nonlinear effects taking place in the flow in order to obtain reliable information and future efforts in feedback flow control field will have to be addressed in this direction.

Key words: Turbulence, Control, DNS, Plane Channel Flow, LQR, Wiener-Hopf

Sommario

Obiettivo del presente lavoro di tesi è quello di valutare le prestazioni dell'applicazione di un controllo in feedback per ridurre l'attrito a parete in un flusso turbolento utilizzando sensori di attrito e pressione a parete, combinati con attuatori MEMS a iniezione e aspirazione, montati a parete.

Il problema è affrontato partendo dalle equazioni di Navier-Stokes, dalle quali viene estrapolato un modello lineare tempo-invariante del flusso. Tale modello rappresenta il punto di partenza per l'implementazione di un controllore LQR in simulazioni DNS, supponendo l'intera conoscenza dello stato del sistema. Il passo successivo ha riguardato l'implementazione di un più verisimile controllore basato esclusivamente sulle misure a parete. La fase di progettazione è stata condotta basandosi sulla teoria della retroazione ottima della misura. I risultati hanno evidenziato la necessità di ricostruire lo stato del sistema attraverso un osservatore.

L'ultima parte del lavoro riguarda la progettazione di un compensatore ottimo basato sulle misure a parete. Questa fase è stata condotta sfruttando una tecnica di controllo alla Wiener-Hopf nel dominio delle frequenze, precedentemente sviluppata per ridurre l'attrito in un flusso turbolento usando un approccio *single-input single-output*. Questa strategia è stata poi estesa al caso *multi-output*, in cui tutte le misure a parete sono disponibili. Simulazioni DNS con differenti pesi sull'attuazione e sul rumore sulle misure hanno mostrato che le prestazioni si riducono, rimanendo pur sempre positive, quando il controllo LQR lascia il posto ad un controllo basato su un osservatore di stato e che l'utilizzo di più misure garantisce una maggiore robustezza delle prestazioni rispetto al rumore sulla misura.

Questi risultati suggeriscono che un approccio lineare nella progettazione del controllore è sufficiente per manipolare con successo un flusso turbolento. Di contro, la stima dello stato deve essere condotta prendendo in considerazione anche gli effetti non lineari che hanno luogo all'interno del fluido, al fine di ottenere informazioni affidabili e gli sforzi futuri nel campo del *feedback flow control* dovranno essere rivolti in questa direzione.

Parole chiave: Turbolenza, Controllo, DNS, Flusso Piano, LQR, Wiener-Hopf

Estratto della Tesi

Lo studio della turbolenza è oggigiorno oggetto di fervido interesse all'interno della comunità scientifica, in quanto la comprensione del fenomeno fisico è il primo gradino verso la predizione e quindi il controllo del comportamento turbolento di un flusso. Riuscire in questo arduo compito avrebbe implicazioni economiche di notevole portata. Basti pensare che se si riuscisse a ridurre solo del 15% l'attrito viscoso sulla superficie degli aeroplani, allora l'industria aeronautica avrebbe risparmi per più di 15 miliardi di dollari l'anno, derivanti dalla riduzione del carburante impiegato per vincere l'attrito dell'aria.

Il presente lavoro di tesi affronta il problema di definire una logica di controllo in feedback per la riduzione dell'attrito viscoso in uno scenario il più prossimo alla realizzazione applicativa, ovvero considerando attuatori e sensori montati a parete. Prima di addentrarsi nella questione, sono stati delineati i concetti fondamentali della teoria della turbolenza, ponendo l'attenzione soprattutto sulle nozioni di strutture coerenti e di ciclo di parete, veri capisaldi attraverso cui fondare la comprensione dei fenomeni turbolenti che avvengono in prossimità di una superficie investita da fluido. Di seguito, per illustrare la vastità del panorama, sono state descritte le principali tecniche per la riduzione del drag che al giorno d'oggi hanno ricevuto approfondito studio attraverso simulazioni DNS o prove sperimentali.

A questo punto è stata definita una geometria ideale in cui studiare il problema. La scelta di un dominio rettangolare ha permesso di utilizzare un codice DNS particolarmente efficiente per la risoluzione delle equazioni non lineari che governano la dinamica del flusso turbolento, controllato e non controllato. Dopodiché, partendo dalle equazioni di Navier-Stokes e sfruttando le spazio-invarianze derivate dalla simmetria del problema, è stato ottenuto un sistema di equazioni differenziali che, trasformato nel dominio di Fourier, ha portato alla definizioni delle note equazioni differenziali di Orr-Sommerfeld e Squire. Tali equazioni sono state poi discretizzate lungo la direzione normale a parete durante l'implementazione numerica. In questa fase, due diversi approcci sono stati considerati, ovvero le differenze finite e le derivate spettrali. L'applicazione di queste tecniche ad un caso test prima ed al calcolo degli autovalori di un sistema di equazioni di Orr-Sommerfeld e Squire per una coppia di numeri d'onda poi, ha permesso di valutarne criticamente le prestazioni.

Ottenuto il modello lineare, è stato così possibile definire una logica di controllo in

feedback. Siccome il controllo a parete risulta agire sul sistema attraverso le condizioni al contorno dell'equazione differenziale, è stata proposta una tecnica di rilevamento al fine di ottenere la formulazione agli stati del problema. Partendo da questa, è stata poi implementata una strategia di controllo ottimo basata sulla retroazione dell'intero stato del sistema. Tuttavia, non essendo possibile inserire il drag nel funzionale del controllo ottimo, in quanto questo permette la sola definizione di norme quadratiche, l'obiettivo di ridurre l'attrito a parete è stato inseguito indirettamente attraverso la definizione di norme dello stato basate su grandezze significative dal punto di vista della fisica della turbolenza. L'utilizzo di dette norme, combinate con scelte opportune degli ulteriori gradi di libertà che tale schema di controllo consente, ha portato alla progettazione di diversi controllori. I problemi numerici dovute al cattivo condizionamento delle matrici di stato nell'equazione di Riccati del controllo ottimo sono stati superati utilizzando algoritmi *ad hoc* basati su fattorizzazione e successiva risoluzione iterativa. I controllori così ottenuti sono stati poi applicati al controllo di un flusso turbolento per un paio di numeri di Reynolds largamente studiati in letteratura. Uno dei risultati più eclatanti è stata la completa rilaminarizzazione di un flusso turbolento ad un basso numero di Reynolds, usando un controllore con guadagni tempo-invarianti, anche modellando l'eventuale saturazione dell'attuatore.

Poi, al fine di ottenere un controllo maggiormente votato all'implementazione pratica, è stato proposta una logica di controllo basata sulla retroazione ottima della misura. Il confronto tra le norme delle funzioni di trasferimento tra disturbo in ingresso e stato del sistema controllato con retroazione della misura e quelle del sistema controllato con retroazione dello stato ha portato alla constatazione dell'esigenza di ricostruire lo stato attraverso un osservatore.

Il punto di arrivo è stato quindi la definizione di una logica di controllo basata sulla definizione di un compensatore ottenuto attraverso l'accoppiamento di controllore ed osservatore ottimo per la retroazione delle misure disponibili a parete. Per fare questo, è stata sviluppata una logica di controllo nel dominio delle frequenze, detta controllo alla Wiener-Hopf, con cui è stato possibile progettare in un solo passo sia il controllore che l'osservatore. Questo ha comportato un notevole risparmio di tempo, in quanto la risoluzione delle due equazioni di Riccati per controllore ed osservatore nel dominio del tempo è stata sostituita dalla risoluzione di un sistema lineare la cui matrice ha una struttura di Toeplitz, se una sola misura è considerata per la retroazione, mentre ha una struttura di Toeplitz a blocchi se più misure vengono retroazionate. Sfruttando le simmetrie interne a queste matrici, è stato sviluppato un algoritmo per ottenerne la fattorizzazione in un tempo che scala col quadrato delle dimensioni delle matrici. Questo ha rappresentato un notevole miglioramento dal punto di vista del costo computazionale, in quanto utilizzare le consuete tecniche di fattorizzazione che scalano col cubo delle dimensioni delle matrici, avrebbe allungato notevolmente la fase di progettazione del compensatore. I compensatori così ottenuti sono stati poi implementati in simulazioni DNS considerando diversi parametri di controllo e diversi livelli di rumore sulle misure al fine di indagare gli effetti sulla riduzione dell'attrito a parete. I risultati hanno evidenziato che quando viene utilizzato un osservatore di stato si ha una significativa riduzione delle prestazioni, le quali rimangono pur sempre positive. Inoltre, l'utilizzo di misure multiple si è dimostrato avere effetti benefici sulla robustezza della stima rispetto al rumore sulla misura.

Infine sono stati considerati possibili sviluppi futuri, quali l'adozione di uno stimatore non lineare in grado di superare i limite dell'osservatore lineare o la stima della risposta non lineare del sistema, la quale può poi essere utilizzata all'interno della teoria del controllo Wiener-Hopf per progettare un compensatore ottimo per il reale comportamento del fluido piuttosto che per la sua approssimazione lineare.

Contents

List of Figures

List of Tables

Preface

The present thesis addresses the engineering problem of reducing the drag in a turbulent channel flow using blowing/suction actuators and sensors at walls. This research field is a very active and recent one, moreover it must face the difficulty of being at the very intersection of two widely studied disciplines, such as theory of turbulence and system control. This work is meant to develop a feedback control law to be applied in a likely environment by considering a multidisciplinary point of view providing for both these approaches.

The work is organized as follows. Chapter 1 introduces the reader to turbulence theory, by describing many general aspects and the most widely accepted arguments concerning it. In particular, the key concepts of coherent structures and near-wall cycle will be outlined.

Chapter 2 offers an overview of the main approaches to flow control for drag reduction, considering both numerical simulations and experimental tests, with a brief description of the state-of-the-Art sensors and actuators already in use.

Chapter 3 presents the DNS code used for the numerical simulations of the present work, then it describes how to obtain a linear model of the channel flow starting from Navier-Stokes equations. Different techniques, namely finite differences and spectral derivatives, have been developed to discretize the differential equations of the linear system.

Chapter 4 is devoted to the formulation of an optimal state feedback control. Then, the effect of control parameters on drag reduction is investigated for different Reynolds numbers, in order to find the configuration yielding the best performances.

Chapter 5 proposes an optimal output feedback control based on the development of an algorithm for the solution of the nonlinear equation arising from optimal control formulation when only wall-measurements are available for feedback. Performances are compared to those of state feedback relying on some norms of disturbance-to-state transfer functions.

Chapter 6 develops an alternative approach based on state estimation from wall-measurements. The dual problem of controller and observer design is formulated as a single optimal control problem in frequency domain, aiming at developing a compensator for the feedback of multiple wall-measures. The effect of different control parameters is investigated through DNS in order to evaluate actual drag and net drag reduction.

Finally, Chapter 7 summarizes and discusses the main achievements of the present work and outlines possible future developments.

Milan, September 2010
Daniele Cavaglieri

Chapter 1

Fundamentals of Turbulence

Turbulence is the last great unsolved problem of classical physics. By the way, one of the greatest modern physicists, Richard Feynman, used to tell this fable in order to clarify this concept. *"As he laid dying, the modern physicist asked God two questions: Why relativity and why turbulence? I really think* - said the famed physicist, - *He may have an answer to the first question"* [19]. As a matter of fact, no one knows how to solve the well-posed set of partial differential equations that govern turbulent flows. Averaging those highly nonlinear equations to obtain statistical quantities always leads to more unknowns than equations, and an *ad hoc* modeling is necessary to close the problem. The struggle to get a full understanding has been long and around with lots of sweat, few victories and much frustration [20]. This chapter is meant to guide the reader to a deep understanding of this evolving panorama, by discussing the most widely accepted concepts in turbulence theory and introducing some of the main issues that nowadays are still object of fervent research.

Until few decades ago, the most accepted view was that turbulence is essentially a stochastic process having randomly fluctuating velocity field superimposed on a well-defined mean reference flow. In this view, fluctuations are completely random in the sense that there is zero probability for any flow variable of having a particular value, and there is zero energy in any one particular frequency or wavenumber. Now common opinion has significantly changed, as it has been recognized that the behavior of all turbulent shear flows are dominated by quasi-periodic large-scale vortex motions. In order to give an index or rate of turbulence, we use to associate to the fluid dynamics system we are considering a dimensionless number Re, called Reynolds number, which is defined as follows:

$$Re = \frac{\rho U L}{\mu} = \frac{V L}{\nu} \tag{1.1}$$

where ρ is the density of the fluid, μ the dynamic viscosity and $\nu = \mu/\rho$ the kinematic viscosity. U and L are the velocity and length scales of the fluid dynamics problem and they represent the typical dimensions at which significant dynamical phenomena happen in the system. This dimensionless number gives a measure of the ratio of inertial forces $\rho U^2 L^2$ to viscous forces $\mu U^2 L$ and consequently quantifies their relative importance for given flow conditions. Furthermore, Reynolds number plays a key role in describing the velocity field of a flow. As a matter of fact, if two fluid dynamics systems have the same Reynolds number, then their scaled velocity fields are also the same. Reynolds number also characterizes different flow regimes: at low Reynolds numbers viscous forces are dominant and the flow assumes a smooth, constant motion. In this case, the flow is said to be in a laminar regime, while at high Reynolds numbers the fluid is dominated by inertial forces, determining chaotic motion. When this happens, the flow is said to be in a turbulent regime. Furthermore, at intermediate values of Re, the flow may show a laminar condition but it can easily shift to a turbulent state with the introduction of small disturbances into the system. This last scenario represents the transition regime. As for turbulent regime, a constant energy supply is needed for this process to be sustained and this energy is extracted from the mean flow into the largest, most energetic eddies that compose the flow. Afterwards, energy is transferred into smaller and smaller scales until it is dissipated by viscous action in the smallest scales of the flow, called Kolmogorov micro-scales, in the name of the scientist who first postulated their existence on the basis of physical argumentations. In wall flows, the phenomenon of dissipation through this energy cascade process takes place in the very neighborhood of the wall. We call this region boundary layer. Furthermore, the thickness δ of this layer provides a good measure of the largest eddies in the flow, while the smallest scale is called the viscous wall unit, which is of the order of Kolmogorov length scale. Since in the near-wall region viscous forces dominate over inertia, the shear stresses τ of the fluid are mainly represented by their viscous component. Furthermore, since no-slip boundary condition imposes null velocity at wall, the inertial stresses, also called Reynolds stresses, are zero and wall shear stresses are determined as

$$\tau_w = \rho\nu \left.\frac{\partial \bar{U}}{\partial y}\right|_w - \cancel{\rho\overline{uv}|_w} = \rho\nu \left.\frac{\partial \bar{U}}{\partial y}\right|_w \tag{1.2}$$

where $\bar{U}$ is the mean streamwise velocity, u and v are streamwise and spanwise fluctuations of velocity, respectively, and y denotes the wall-normal direction. The observation that viscous stresses dominate the wall region allows to choose a proper viscous time-scale t_ν by taking

$$t_\nu = \left(\left.\frac{\partial \bar{U}}{\partial y}\right|_w \right)^{-1} \tag{1.3}$$

The viscous time-scale is then easily derived from dimensional analysis

$$l_\nu = \sqrt{\nu\, t_\nu} = \sqrt{\frac{\nu}{\left.\frac{\partial \bar{U}}{\partial y}\right|_w}} \tag{1.4}$$

The wall velocity scale follows directly from Equations (1.3) and (1.4)

$$u_\tau = \frac{l_\nu}{t_\nu} = \sqrt{\nu \frac{\partial \bar{U}}{\partial y}\bigg|_w} = \sqrt{\frac{\tau_w}{\rho}} \tag{1.5}$$

So, near-wall flow can be represented using dimensionless wall units, obtained after scaling flow variables with the viscous scales, which are usually indicated with superscript $+$. Hence, the nondimensional distance from wall is $y^+ = y/l_\nu = y\,u_\tau/\nu$. Then, depending on y^+, different regions, or layers, are defined in the near-wall flow. We define the *viscous wall region* as the region for $0 < y^+ < 50$, while the region $y^+ > 50$ is called the *outer layer.* Furthermore, within the viscous wall region, we define the *viscous subregion* as the region for $y^+ < 5$, in which Reynolds shear stresses are negligible with respect to viscous stresses. Finally, the transition region between the viscosity-dominated and the inertia-dominated part of the flow, i.e. for $5 < y^+ < 30$, is called the *buffer layer.*

Starting from this well accepted framework, fluid dynamicists have long sought to understand how boundary-layer turbulence is generated and dissipated. Since boundary-layer flows are the technical driver for so many engineering applications, lots of financial and human resources have been brought to bear on the problem over many decades of study. The progress made, however, has not been commensurated with the effort expanded, reflecting the intrinsic complexity of turbulence phenomena and the difficulty that must be faced when trying to reproduce turbulent precesses in a controlled framework. For this reason, most of turbulence knowledge has resulted from investigation at low Reynolds numbers, where effective flow visualizations and Direct Numerical Simulations (DNS) are possible. In this context, it has been made possible the identification of coherent motions. Historically, fundamental studies can be found in [71] and [66] and nowadays, even if with some controversy, they are quite universally considered as reference works. Despite this, no generally accepted definition of what is meant by coherent motion has arisen. Actually, in physics coherence stands for a well-defined phase relationship. As for turbulence, if we accept Robinson's definition *"a coherent motion is a three dimensional region of the flow over which at least one fundamental flow variable exhibits significant correlation with itself or with another variable over a range of space and/or time that is significantly larger than the smallest local scales of the flow"* [64]. The major motivations for investigating coherent motions in turbulent boundary layers are:

- to aid predictive modeling of the gross statistics of turbulent flows
- to understand the dynamical processes responsible for statistical properties in order to predict them through an appropriate modeling
- to guide alteration and control of turbulence.

The third reason, in particular, concerns the main issues addressed in the present work. As for the reference framework for coherent structures analysis, is is usual to consider a flat-plate, smooth-wall boundary layer with a two-dimensional mean flow, without pressure gradient, wall heating, force fields or compressibility effects. In such environment, the turbulence production process is dominated by three kinds of quasi-periodic eddies: the large outer structures, the intermediate Falco eddies and near-wall eddies. As for large outer structures, they appear as large three dimensional bulges that scale with the layer thickness δ and extend across the entire boundary layer, as depicted in Figure 1.1. These eddies control the dynamics of the boundary layer in the outer region and appear quasi-periodically in space and time. Falco eddies represent another typology of highly coherent structures, which are characterized by having a three-dimensional extension. They usually appear in wakes, jets and boundary layers at an intermediate scale of 100 wall units and play a key role in the interaction between large outer structures and near-wall events. In order to highlight these structures, smoke has been used as in Figure 1.2 to fill the near-wall region of a boundary layer. What appear are roughly circular regions devoid of marked fluid, that have been called pockets.

The third kind of eddies takes place in the wall region, where the most part of the turbulent production in the entire boundary layer occurs during intermittent, violent outward ejections of low-speed fluid and during inrushes of high-speed fluid at a shallow angle toward the wall. This intermittent quasi-cyclic sequence of intense organized motions have been collectively termed the bursting phenomenon. This process, which is schematically outlined in Figure 1.4, begins with elongated counter-rotating streamwise vortices, which induce low- and high-speed streaks between them, as illustrated in Figure 1.5. Then, low-speed regions (Figure 1.3) grow downstream, lift up and develop instantaneous inflectional profiles. At approximately the same time, the interface between low- and high-speed fluid begins to oscillate. Hence, the low-speed region lifts up away from the wall as the oscillation amplitude increases and then the flow rapidly breaks up into a completely chaotic motion. Virtually all of the net production of turbulent kinetic energy in the near-wall region occurs during these bursts. This phase is followed by a large-scale motion of upstream fluid that emanates from the outer region and sweeps the wall region of the previously ejected flow. This sweep event seems to have a stabilizing effect on the bursting site, since it prepares the wall region for a new cycle, thus determining a self-sustaining regime. The relationship between coherent structures in the outer region and near-wall cycle is still not completely understood even if strong evidence of this interaction has been provided in recent works, such as [29] and [54].

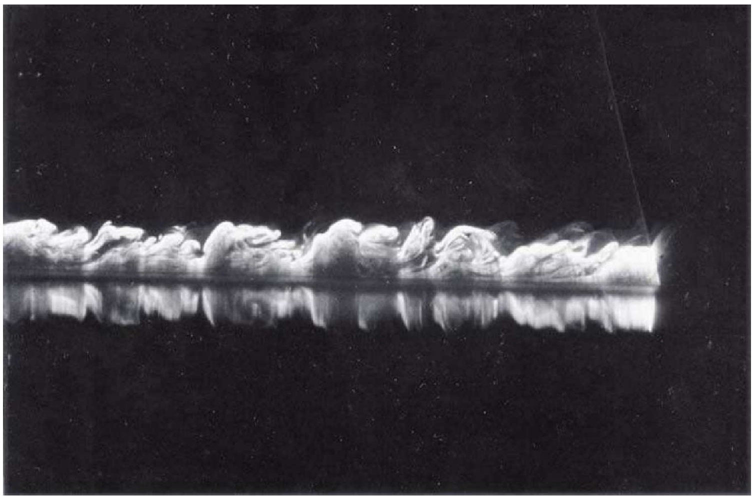

Figure 1.1: Side view of a low-Reynolds-number turbulent boundary layer from [22].

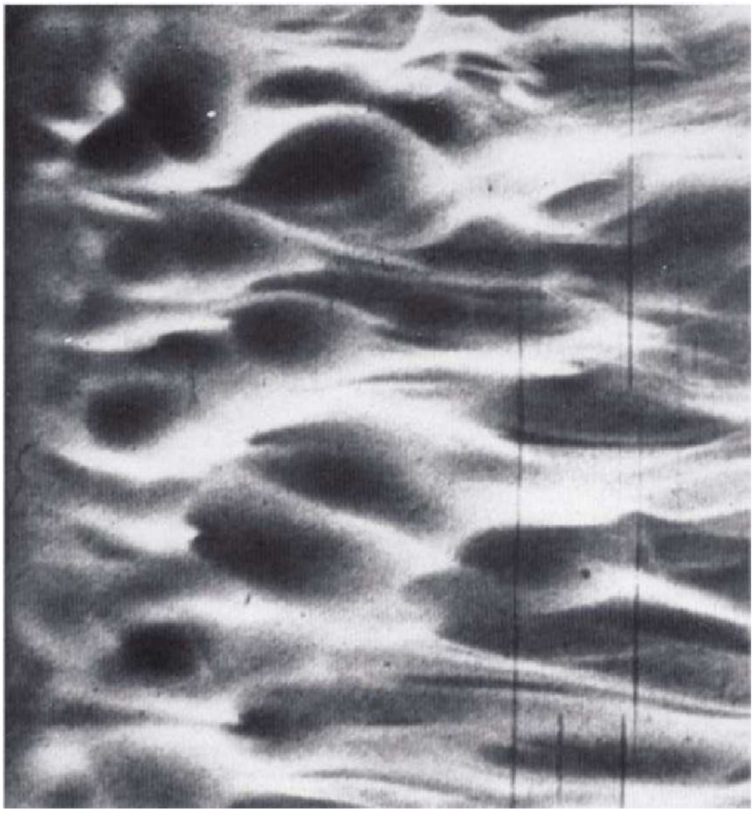

Figure 1.2: Top view of a low-Reynolds number turbulent boundary layer from [18].

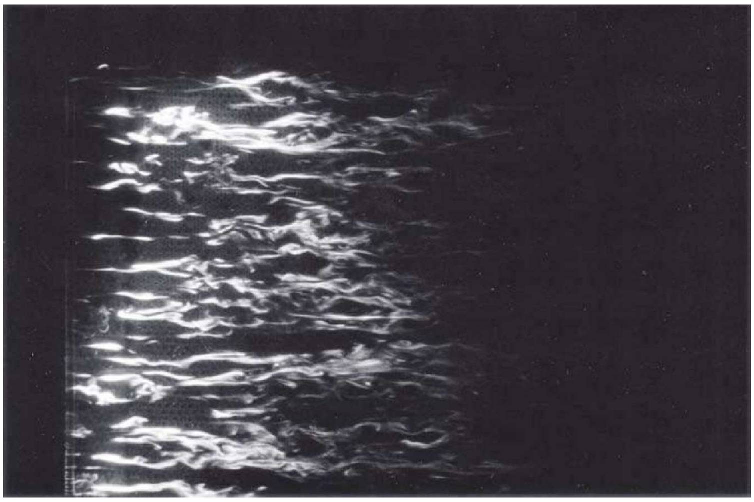

Figure 1.3: Top view of a low-Reynolds-number turbulent boundary layer from [22].

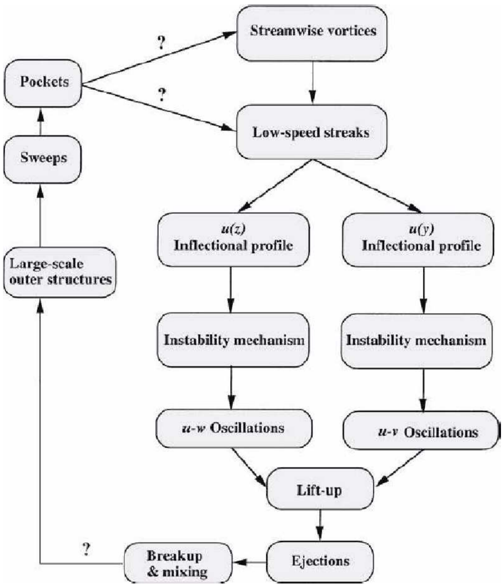

Figure 1.4: Sequential events arising during the bursting process. Arrows with question mark indicate relationships that are still object of debate.

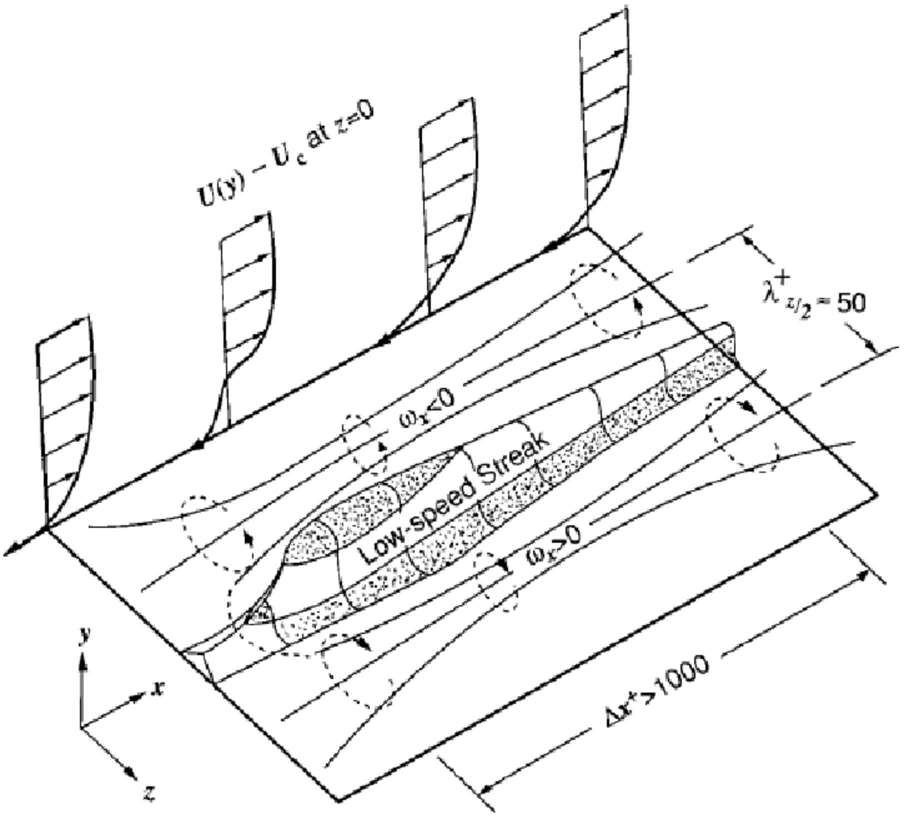

Figure 1.5: Physical model of near-wall turbulent coherent structure generation.

Chapter 2

Flow Control

The possibility of manipulating a flow field in order to obtain a desired objective is of immense technological importance and this surely accounts for the subject being more hotly pursued by scientists and engineers than any other topic in fluid mechanics. It is sufficient to think that the potential benefits arising from the implementation of efficient flow-control systems range from saving billion of dollars in annual fuel costs for land, air and sea vehicles to achieving more competitive industrial processes involving fluid flows. According to a recent study by Airbus [67], turbulence control could reduce the drag of a civil aircraft up to 15%, as shown in Figure 2.1, resulting in more than 15 billion dollars saving per year for shipping industry. In this context, flow manipulation may play a key role in meeting several goals, such as reducing the drag, as previously mentioned, or enhancing the lift, augmenting the mixing of mass, momentum or energy, suppressing the flow-induced noise or a combination thereof. To achieve these results, transition from laminar to turbulent flow may have to be either delayed or advanced, flow separation may have to be either prevented or provoked, and finally turbulence levels may have to be either suppressed or enhanced. All these engineering goals and their connection with flow modifications are schematically outlined in Figure 2.2. It is to remark that none of these targets is particularly difficult if taken alone, but the aim is to achieve the desired objective adopting simple devices, inexpensive to build as well as to operate, so that the expense for flow manipulation would result in a significant net positive saving. Unfortunately, all these goals are not necessarily mutually exclusive, as depicted in Figure 2.3, and potential conflicts usually arise as one tries to achieve a particular control goal only to affect adversely another goal. Thus, an ideal method that is simple, inexpensive to build and operate, and that does not have any trade-offs does not exist and the skilled engineer has often to make compromises.

In order to give an exhaustive overview of flow control methods, we have to remark that many different classifications are possible. One of these is to consider whether the technique is applied at the wall or away from it. In the former case, the flow may be altered by modifying influent surface parameters, like curvature, rigid-wall motion, compliance, temperature and porosity. Even heating and cooling of the surface can

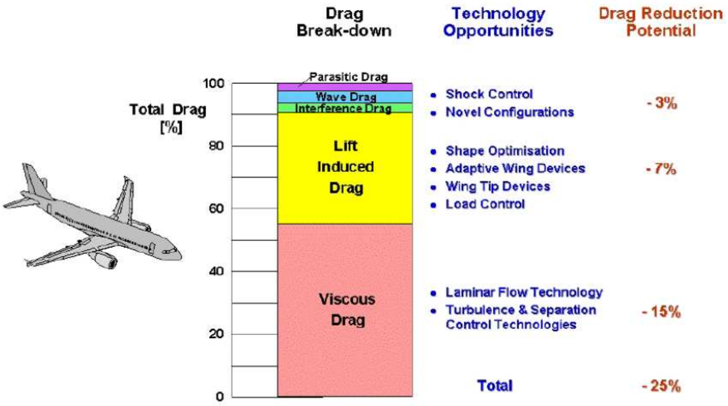

Figure 2.1: Drag break-down of a civil aircraft and potential drag reduction.

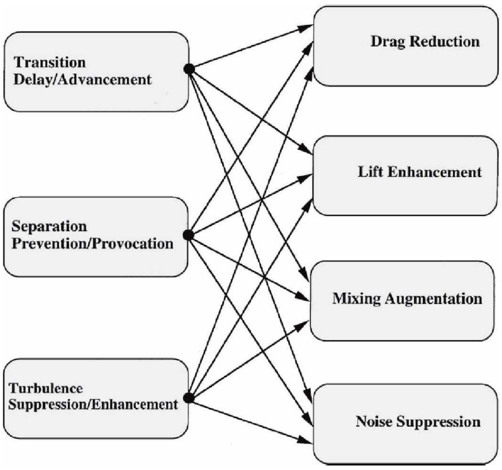

Figure 2.2: Flow modifications and engineering goals.

influence the flow through the resulting density gradients. Mass transfer is possible via suction/injection through a porous wall. Different additives, such as polymers, surfactants, micro bubbles, droplets, particles can also be injected through the surface in water wall-bounded flows. As for the latter case, control devices located away from the surface can also be beneficial. Large-eddy breakup devices (LEBU), acoustic waves, magneto- and electrohydrodynamical body forces are examples of flow control strategies applied away from the wall.

Another scheme for classifying flow control methods considers energy expenditure and the control loop involved. A control device can be passive, thus requiring no auxiliary power and no control loop, or active, hence requiring some energy expenditure, as shown in Figure 2.4. Moreover, active control requires a control loop and is further divided into predetermined or reactive. Predetermined control includes the application of steady or unsteady energy without regard to the particular state of the flow. In this case, the control loop is open and no sensors are required. Reactive control, instead, is

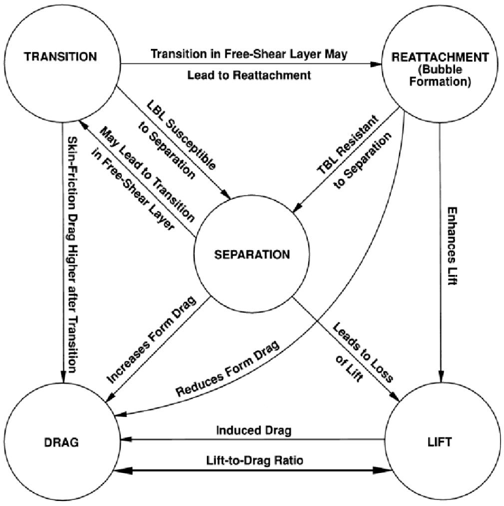

Figure 2.3: Interaction between flow-control goals.

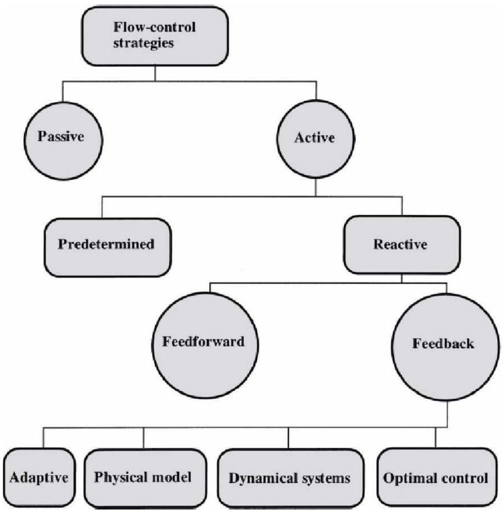

Figure 2.4: Classification of flow control strategies.

a special class of active control where the control input is continuously adjusted based on measurements of some kind. In reactive feedforward control, the measured variable and the controlled variable differ, while reactive feedback control necessitates the controlled variable to be measured, fed back and compared with a reference input. In the following, a brief review of the state-of-the-Art control strategies is given according to the approach adopted and after that, an introductory discussion will describe the most up-to-date sensors and actuators which have been used in experimental tests regarding flow control.

2.1 Passive control

2.1.1 Compliant coatings

Among passive techniques for boundary layer manipulation, compliant coatings surely represent the most simple solution since it does not require slots, ducts or internal equipment of any kind. Aside from reducing drag, other reasons for the strong interest in studying compliant coatings are their many other useful applications, for example as sound-absorbent materials in noisy flow-carrying ducts in aero-engines and as flexible surfaces to coat naval vessels for the purpose of shielding their sonar arrays from the sound generated by the boundary-layer pressure fluctuations.

The idea of adopting compliant coatings for drag reduction came out from studying dolphins' surprising swimming skill. As a matter of fact, bottlenose dolphins have been clocked swimming at speed exceeding $10\,m/s$ for periods of over $7\,s$, but assuming that the power output of cetaceans is equal to that of other mammals ($\approx 35\,W/kg$ of body weight), then such speeds are reached under turbulent flow conditions only if dolphins can expend several times more power than their muscles can generate. More specifically, it can be demonstrated, on the basis of energy considerations, that dolphins can not exceed a speed of $6\,m/s$ for periods greater than 2 hours. The only possible explanation is that dolphins have a lower skin-friction drag level than expected due to their complex epidermis, which acts as a compliant coating optimized over each portion for the appropriate range of local Reynolds number. However, replicating Nature's perfection has represented an arduous task and only after many decades of contradictory results, this technique has been proved to achieve some results in delaying flow transition from laminar to turbulent condition caused by Tollmien-Schlichting instability (TSI). For an exhaustive description of this phenomenon the interested reader is referred to [65].

The mechanism through which compliant coatings work is strictly related to the hydroelastical coupling of fluid and solid which causes an irreversible energy transfer from the former to the latter. However, for longtime it has been deemed impractical to clearly demonstrate its effectiveness and the first significant results appeared for the first time in Lee's wind-tunnel experiments [43]. The coating used for the tests was made by a mixing 91% by weight of $100\,mm^2/s$ silicon oil with 9% of silicone elastomer. Results showed that, as compared to the rigid wall, the single layer, isotropic, visco-elastic compliant coating significantly suppressed the root-mean-square (rms) amplitude of the artificially generated Tollmien-Schlichting waves across the entire boundary layer for a range of Reynolds numbers (Figure 2.5).

2.1.2 Introduction of additives

Turbulent skin-friction drag can be reduced by the addiction of several substances, such as long-chain molecules and microbubbles in liquid flows. The addition of these substances leads to a suppression of the Reynolds stress production in the buffer zone.

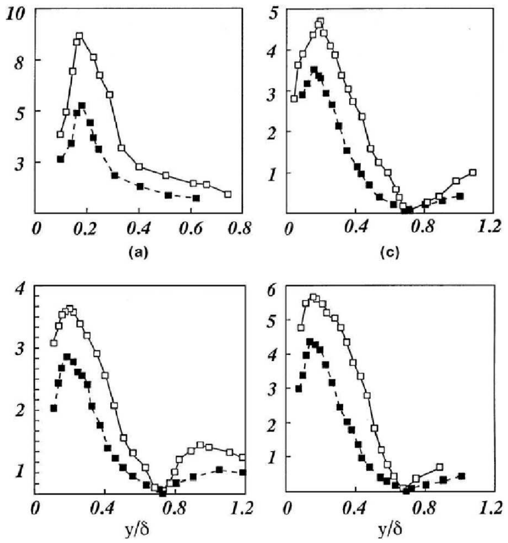

Figure 2.5: Comparison of distribution of rms amplitude of the TSI of rigid surface (white squares) and compliant surface (black squares) across boundary layer. (a) $Re = 1274$, (b) $Re = 1105$, (c) $Re = 1225$, (d) $Re = 1350$.

Thus, the turbulent mixing is inhibited and a consequent reduction in the viscous wall shear stress is achieved. Among the possible techniques for drag reduction, solutions of micromolecules is perhaps the more mature technology. By the way, it has been proved that the addition of less than 100 parts per million of polymethyl methacrylate to a turbulent pipe flow of monochlorobenzene can lead to a skin-friction reduction up to 80% in both external and internal flows, even if its application can be very cost-effective: oil companies, for example, appear to have concluded that the use of polymers for supertankers is just at the break-even point, economically speaking. According to Lumley [50] - [51], the onset of drag reduction is associated with the expansion outside the viscous sublayer of polymer molecules, which at rest are in the form of spherical random coils. This process causes an increase in effective viscosity which damps only the small dissipative eddies, resulting in reduced momentum transport, hence reduced drag.

2.1.3 Large-eddy breakup devices

Large-eddy breakup devices (LEBUs) are designed to alter or break up the large vortices from the outer edge of a turbulent boundary layer. A typical arrangement consists of one or more splitter plates placed in tandem in the outer part of a turbulent boundary layer, as illustrated in Figure 2.6. Unfortunately, there is little theoretical basis for how these geometrical modifications affect the skin-friction and most of the present knowledge comes from experimental evidence. Anyway, tests have shown that it is very easy to substantially reduce the skin-friction, while the most difficult task is to ensure that the device's own skin-friction and pressure drag do not exceed the saving. Among the results achieved, a noteworthy net drag reduction of 20% has been obtained, thus

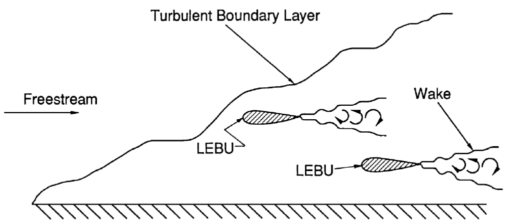

Figure 2.6: Standard arrangement of a LEBUs array.

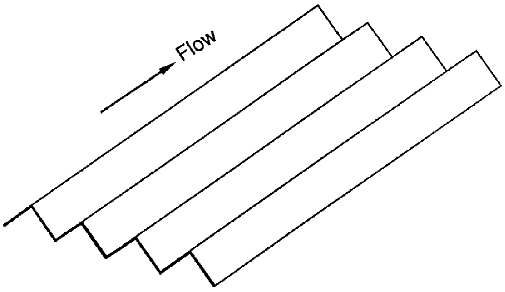

Figure 2.7: Longitudinal ribbed surfaces.

leading LEBUs to be considered one of the most performing solution for drag reduction.

2.1.4 Riblets

Another interesting geometrical modification is represented by riblets, which are wall grooves aligned with the freestream. Small longitudinal striations in the surface interacting favorably with the near-wall structures in a turbulent boundary layer can produce a modest drag reduction in spite of the increase in wet surface area. A net drag reduction of 8% is obtained using V-groove geometry with sharp peak and either sharp or rounded valley (Figure 2.7). Moreover, optimum height and spacing of the symmetric grooves have been found to be about $15\,\nu/u_\tau$. Curiously, the fastest sharks have a surface covering of dermal denticles with flow-aligned keels having the same optimal riblet spacing (Figure 2.8). Riblets work by restraining the movement of the near-wall longitudinal vortices and therefore maintain their coherence. The stabilized

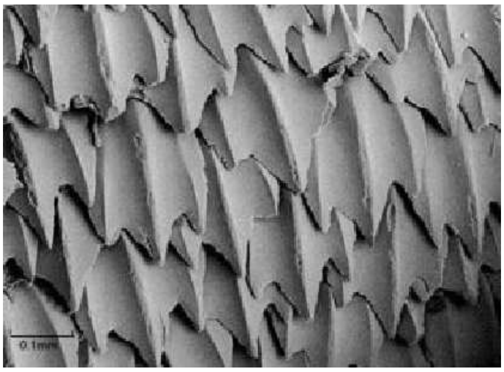

Figure 2.8: Detail of shark skin.

coherent structures present a barrier to the usual cascade from large to small scales and hence impede the rate of energy loss with a resulting drag reduction despite the increased surface area.

2.2 Active control

2.2.1 Predetermined control

Predetermined control mainly involves introducing waves into the flow through actuations or wall movements. Among the former solutions, an interesting one is that proposed in [55], where blowing/suction actuation was employed to form a streamwise-traveling wave of wall-normal velocity v_w, i.e.

$$v_w(x,\, t) = A \sin(\alpha x - \omega t) \tag{2.1}$$

where t is time, x the streamwise coordinate, A the amplitude of the oscillation, $\omega = 2\pi/T$ the frequency of oscillation and $\alpha = 2\pi/\lambda_x$ the streamwise wavenumber where λ_x is the wavelength. Another solution is the one reported in [16] and [17] where the following spanwise-oriented volume forcing was investigated:

$$f_z(z,\, t) = F e^{-y/\Delta} \sin(\beta z - \omega t) \tag{2.2}$$

where z is the spanwise coordinate, Δ the distance up to which the forcing diffuses from the wall and β is the spanwise number. Approximately 30% drag reduction was achieved in a turbulent channel flow at $Re = 3500$.

As for the latter solutions, an interesting way of reducing drag is to adopt oscillating walls moving sinusoidally in spanwise direction with period T, according to the following law

$$w_w(t) = A \sin(\omega t) \tag{2.3}$$

where w_w denotes spanwise velocity component at wall, while the other quantities are the same as before. In [63] this control law has been studied, through parametric investigation over Direct Numerical Simulations of turbulent channel flow, concluding that an optimal frequency ω_{opt} for drag reduction exists and such a reduction can be as high as 34% if the wave amplitude is comparable with the flow centerline velocity. Furthermore, in [61] this technique has been extended for the first time in literature to consider also streamwise-traveling waves of spanwise wall velocity, leading the motion law to account also for spatial displacement, i.e.

$$w_w(x,\, t) = A \sin(\alpha x - \omega t) \tag{2.4}$$

With this motion law, which is graphically represented in Figure 2.9, waves move in streamwise direction with a phase speed $c = \omega/\alpha$. This wall motion law has then been

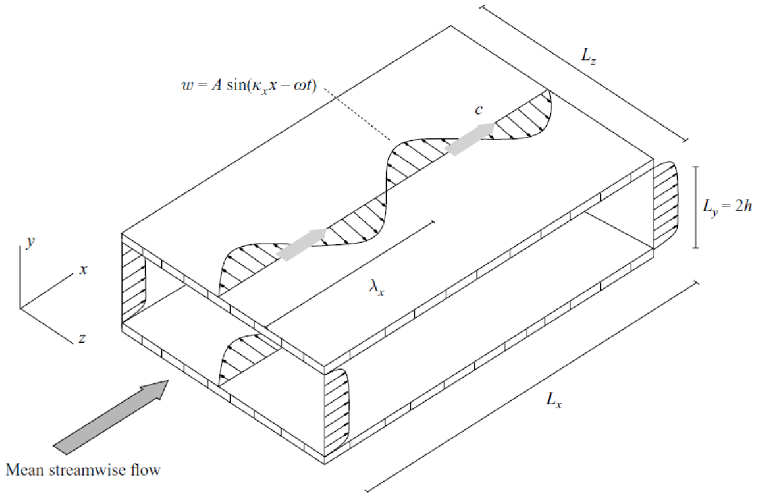

Figure 2.9: Schematic representation of the turbulent channel flow simulated through DNS.

tested through parametric DNS for an array of frequencies ω and wavenumbers α in order to find the optimum set $(\omega_{opt},\, \alpha_{opt})$ achieving the maximum drag and net drag reduction. Results reported in Figure 2.10 show that, off the axes, the perturbed flow reveals an unexpectedly rich behavior. In particular, we can notice a red region of high drag reduction with a peak value of 48% and a cone-shaped blue region of drag increase for $0.35 \leq c \leq 0.6$, showing a peak value of 23% for a phase speed $c = 0.5$. Net power saving can then be computed by considering the power saved from drag reduction and subtracting the power spent to apply the control action. Results in Figure 2.11 show that the region of maximum net saving nearly coincides with the region of maximum drag reduction (DR) and net power saving is positive mainly for slow forward traveling waves, i.e. $0 \leq c \leq 0.2$. Besides, a peak value of 18% net saving is achieved for $(\omega,\, \alpha) \approx (0.15, 1)$.

Although the details of the mechanism through which such waves achieve significant drag reduction are still object of further investigation, a deeper view of the phenomenon has been given in [60], where it has been assumed that streamwise-traveling waves operate by creating a transversal boundary layer in the near-wall region of the channel flow. When the waves move at a speed comparable with the convection velocity, a lock-in effect renders the instantaneous turbulent flow highly three-dimensional, thus provoking drag increase. Instead, when the phase speed is sufficiently different from the near-wall turbulent convection velocity, then the induced spanwise boundary layer can be viewed as a generalized Stoke layer, whose thickness has been proved to linearly correlate to drag reduction till $DR = 35\%$. Beyond this value, waves are oscillating on a time scale larger than the typical lifetime of the near-wall turbulence, thus decreasing the effect of drag reduction.

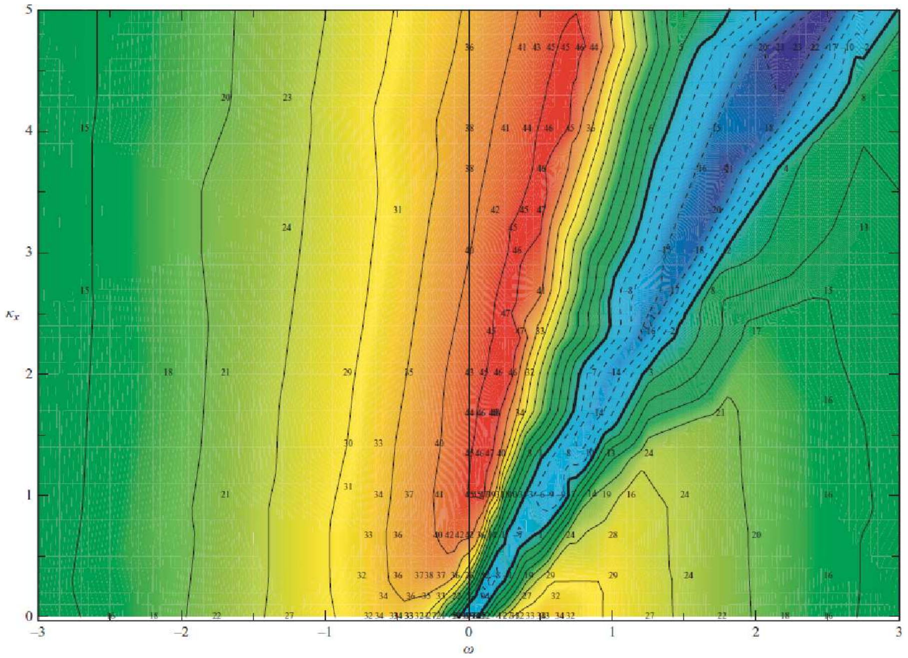

Figure 2.10: Maps of drag reduction DR in the $\omega - \alpha$ plane for $A = 0.5$ and $Re = 4760$. Solid lines denote positive DR, while dashed lines indicate negative DR.

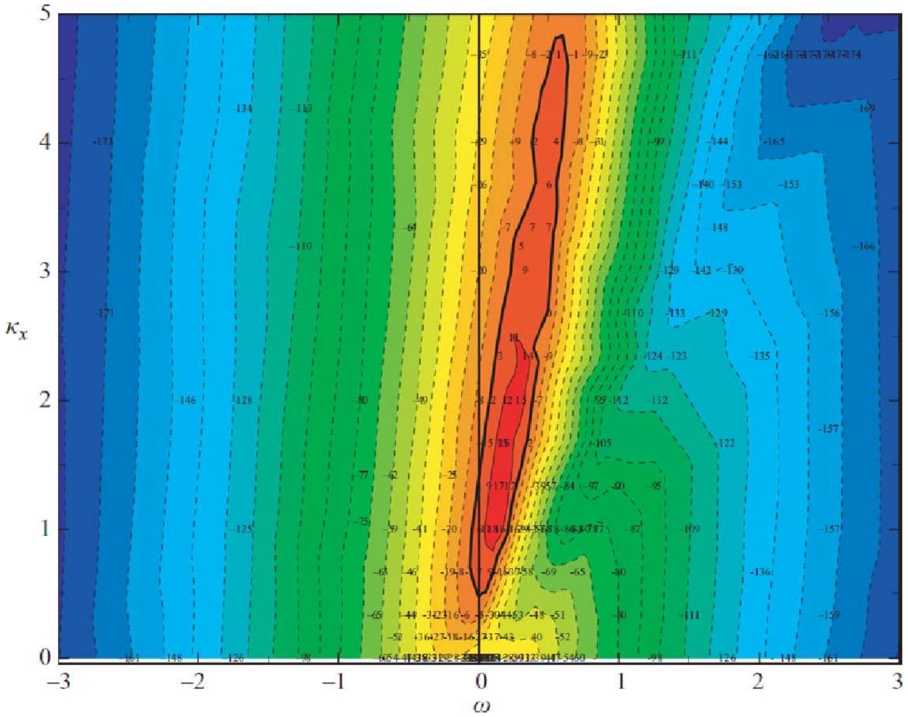

Figure 2.11: Maps of net power saving in the $\omega - \alpha$ plane for $A = 0.5$ and $Re = 4760$. Solid lines denote positive balance, while dashed lines indicate negative net drag reduction.

2.2.2 Feedforward control

The most popular feedforward strategy for controlling turbulent channel flows is the opposition control strategy firstly presented in [12]. With this approach, a detection plane for one of the velocity component is introduced in the flow at a distance of $y^+ \approx 10$. The detected velocity is then applied phased shifted by $-\pi$ as a boundary condition at walls. With this method, direct numerical simulations have showed a drag reduction of around 20% using wall-normal vorticity and 30% using spanwise velocity.

Another meaningful attempt to introduce feedforward control, using this time a control law based on an analytical model, is the one proposed in [5], which concerns the application of a receding-horizon model-predictive control to reduce drag in a turbulent channel flow. With this strategy, the evolution of the system is considered over a finite interval and control inputs are optimized over this finite interval using an iterative gradient-based strategy. Once optimized, control inputs are applied to the evolving flow system, then the procedure is repeated on the following time interval. It has been made possible thereby to fully relaminarize a turbulent channel flow at a low Reynolds number, indicatively $Re = 1500$.

2.2.3 Feedback control

Feedback control is the branch of reactive control that has received the greatest attention due to its solid theoretical background. In this context, the standard scenario considers channel flow with skin friction and pressure sensors at walls to provide system measurements, while zero-net-mass-flux blowing/suction MEMS actuators continuously distributed over the walls are used to manipulate the flow inner structure.

One of the first approaches of this kind, before the introduction of linear systems theory to flow control, has been presented in [41], where a neural network has been implemented in order to adaptively find a feedback law for the local wall shear stress, achieving about 20% drag reduction. A linear feedback based on classical control theory has then appeared in [31], in which it was used to stabilize a turbulent wall flow in a two-dimensional channel using blowing/suction at walls coordinated with measurements of wall shear stresses. Afterwards, modern control theory has been introduced in [38], followed by the extension of the previously developed two dimensional controller to a three-dimensional one, which has been carried out by the same group work in [42], where an *ad hoc* scheme was augmented in the third direction. An exhaustive discussion on the application of linear quadratic feedback control to three-dimensional channel flows has appeared for the first time in [7]. This strong theoretical framework has then received further refinements in [3] and has been applied in [25] for delaying laminar-to-turbulent transition in channel flows for a couple of Reynolds numbers, namely $Re = 2000$ and 3000. Finally, in a recent work [52], LQR control has been tested to achieve net drag reduction for higher Reynolds numbers. Results showed that more than 20% net power saving is possible at $Re = 1500$ and 3500 and up to 15% at $Re = 6500$, as outlined in Figure 2.12.

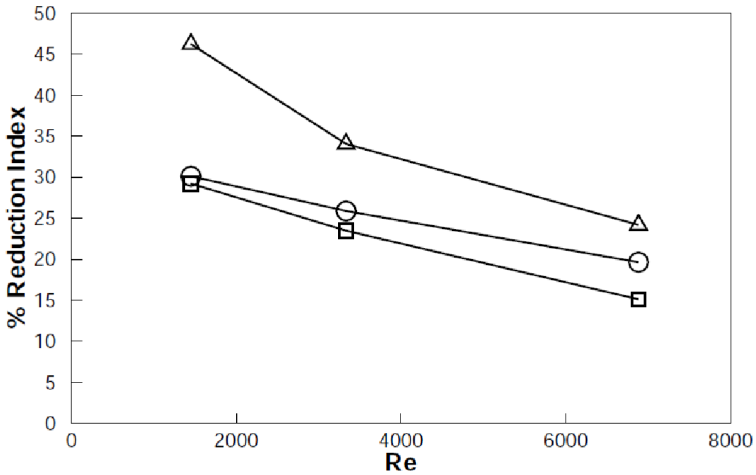

Figure 2.12: Performance of LQR control at different Reynolds numbers. △ = Turbulent kinetic energy, ○ = Drag reduction, □ = Net power saving.

2.3 Sensors and actuators for flow control

2.3.1 Sensors

Unlike most of common control devices, sensors for feedback control of turbulence must meet very hard requirements. First of all, they must have a physical size and response time small enough compared with the spatial and temporal scales of turbulent structures. Experiments conducted in laboratory suggested that the appropriate size of shear stress/wall pressure sensors should be less than $30-40$ viscous units [35]. Afterwards, in order to detect the near-wall structures, it is necessary to build an array of sensors, rather than a single sensor, so to catch even local fluctuations. Clearly, such specifics could be met only by adopting microelectro-mechanical system devices (MEMS). Development of such sensors for use in fluid science has been largely documented in literature, hence for a deeper knowledge of the subject, the interested reader is referred to [21].

The most common MEMS control scheme considers an array of sensors to be mounted flush to the wall. Thus, fluctuating wall shear stresses in streamwise and spanwise directions, τ_{x_w} and τ_{z_w}, respectively, and wall pressure p_w are used to detect the flow state near the wall. Since it is known that the rms value of the wall-shear-stress fluctuation is $\tau_{w,rms} \approx 0.4\tau_w$ and this ratio is quite Reynold-independent, if we suppose that the measurement accuracy required is 5% of the rms value, then the sensitivity should be at least 2% of the full scale of τ_w, which is not difficult to achieve with MEMS sensors. The root-mean-square of wall-pressure fluctuation, instead, is approximately $3\tau_w$ for $Re \approx 1000$. Thus, the sensitivity of 2% of the full scale must be about $0.15\tau_w$, and owing to this larger magnitude, the pressure fluctuation seems better suited for control.

Among the great variety of MEMS sensors, the most mature device for detecting

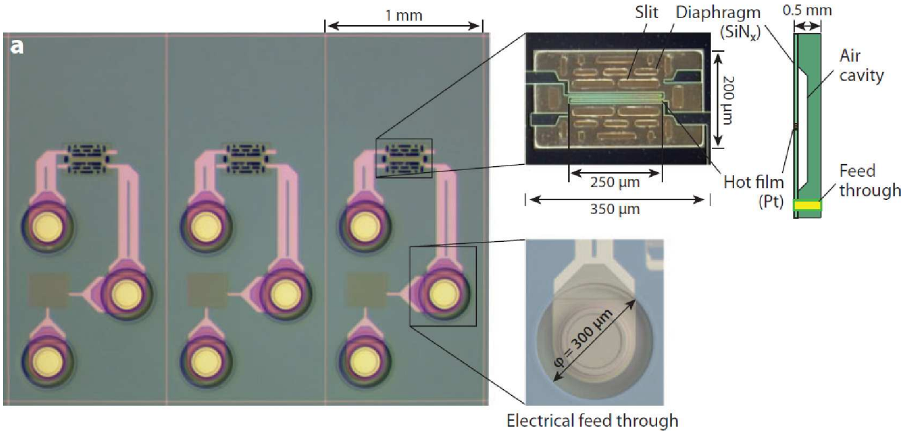

Figure 2.13: Example of micro hot-film wall-shear-stress sensor array with backside electrical contact.

wall shear stresses is the micro-hot-film wall shear stress sensor, which is based on a thermal principle, in that it measures heat transferred from a resistively heated element to flowing fluid, thus indirectly obtaining the wall shear stress. Figure 2.13 shows MEMS sensor arrays with a platinum hot film deposited on a 1-μm-thick SiN_x diaphragm ($400 \times 250\,\mu m^2$), where eighteen sensors are aligned at a pitch of $1\,mm$ in the spanwise direction.

Another sensor, which instead is not based on a thermal principle, uses a micro-floating element for the direct mechanical measurement of shear stress. This element is free to displace laterally against the restoring springs and it is flush mounted to the wall. The displacement of this element is measured with a capacitive or optical method. Its dimensions range from $120 \times 120\,\mu m^2$ to $500 \times 500\,\mu m^2$ and a flat frequency response up to $4\,kHz$, while its noise floor is as low as $0.0004\,Pa$.

2.3.2 Actuators

As for MEMS actuators, the following requirements should be met:

- small dimensions
- fast response
- low energy consumption
- large fluid interaction
- robustness in hostile environment.

Then, actuation force for flow control can be divided in three different categories: electromagnetohydrodynamic or electric body force, on-demand jets and surface force due to a moving fluid-solid interface. Electromagnetohydrodynamic force has proved to be effective for drag reduction in conductive fluids as seawater [9]. Furthermore, in [47]

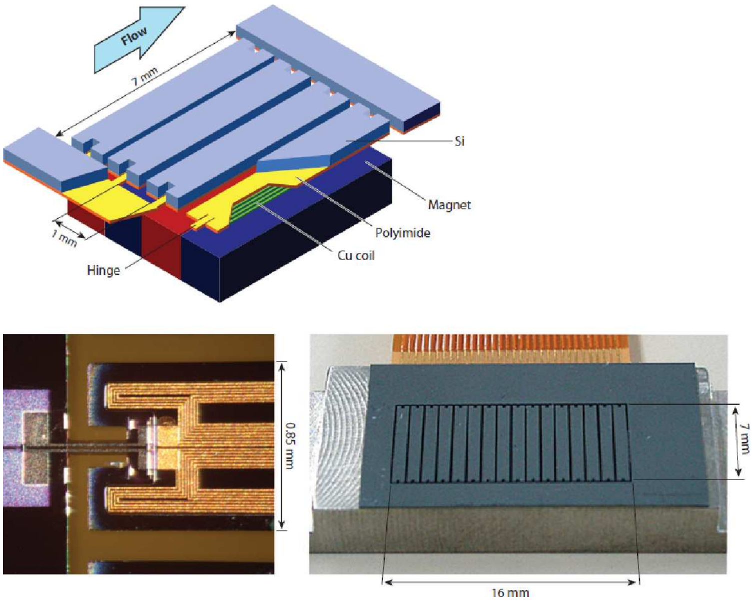

Figure 2.14: Array of seasaw-type magnetic actuators.

electroplated Permalloy has been employed to obtain large out-of-plane displacement in response to an external magnetic field, while in [73] an elongated Si flap was used with a pair of polymide hinges and a permanent magnet array underneath, as shown in Figure 2.14. Unfortunately, the low efficiency of body force in case of poor electrical conductivity of the flow still remains a problematic issue.

For this reason, synthetic jets represent nowadays a preferred choice, since they can benefit of a broader range of applications. Basically, they are realized through an oscillating diaphragm in a cavity with an orifice which generates a zero-net-mass-flux above the orifice.

2.4 Experimental tests

Until now, few attempts have been made to develop feedback control systems in physical experiments. As for predetermined control, the earliest experimental verfications of the oscillating-wall concept are those in [39] in the geometry of a boundary layer and in [14] and [13] in the circular pipe. Several other studies, most of them mentioned in [34], have extended such results. It is to remark that all of them are low-Reynolds setups where the wall oscillation is implemented through mechanical vibrating devices and the measurements are often obtained through a probe mounted near the moving wall. A notable exception is that in [57], where Lorentz body force was employed. The same forcing was implemented in [9] in order to experimentally realize spanwise-traveling wall forcing. Finally, in [59] laboratory tests assessing drag-reducing effect of streamwise traveling waves have been carried out in the geometry of the circular pipe, where the naturally periodic spanwise direction makes the implementation of

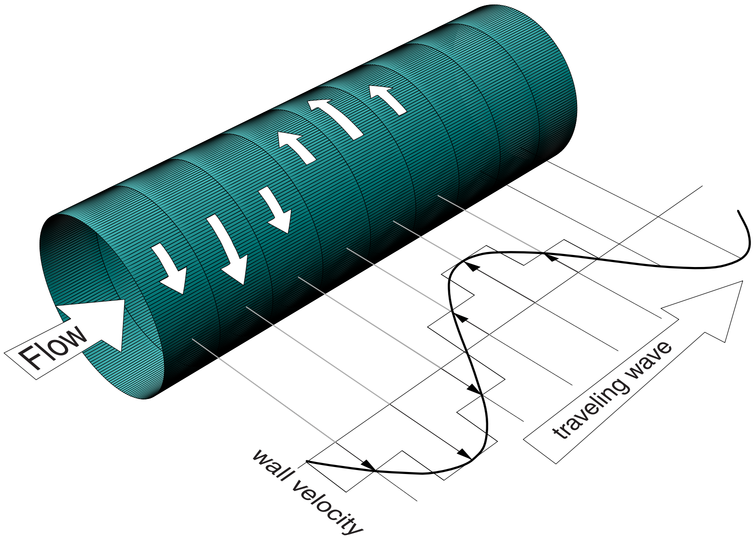

Figure 2.15: Graphical representation of the traveling-wave concept. The desired space-time variation of the transverse wall velocity is achieved through independent alternate motion of adjacent pipe slabs.

traveling waves easier. The spatio-temporal variations required to enforce the waves are obtained through a time- and space-varying rotational speed of the pipe wall. While the harmonic dependence on time is easily implemented, the sinusoidal variation along the streamwise direction is discretized by imposing different rotation rates to different thin longitudinal slabs of the pipe, as shown in Figure 2.15.

As for reactive feedback control, in [30] a control system was set up by using piezo-electric flap actuators and hot-film sensor arrays located upstream and downstream of the actuators. Then, a feedforward/feedback control scheme was applied in order to suppress low- and high-speed streaks induced by vortex tubes in a laminar boundary layer. In [62], a control system was realized using two rows of three wall-mounted hot-film sensors with a single row of three synthetic jet actuators in between. A linear feedback control scheme coupled with a Wiener filter was employed to achieve a 30% reduction of streamwise velocity fluctuations. Recently, in [74] a prototype system has been developed for the feedback control of a turbulent air channel flow (Figure 2.16). This device is composed by an arrayed micro hot-film sensors with a spanwise sensing of $1\,mm$ for the measurement of streamwise shear-stress fluctuations, while arrayed magnetic actuators of $2.4\,mm$ in spanwise width were used to introduce control input through wall deformation. The driving voltage of each actuator is determined with a linear weighted sum of the wall shear-stress fluctuations detected by three sensors located upstream of each actuator and a noise-tolerant genetic algorithm optimizes the control parameters in such a way that the drag reduction is maximized. With this strategy approximately 6% drag reduction was achieved.

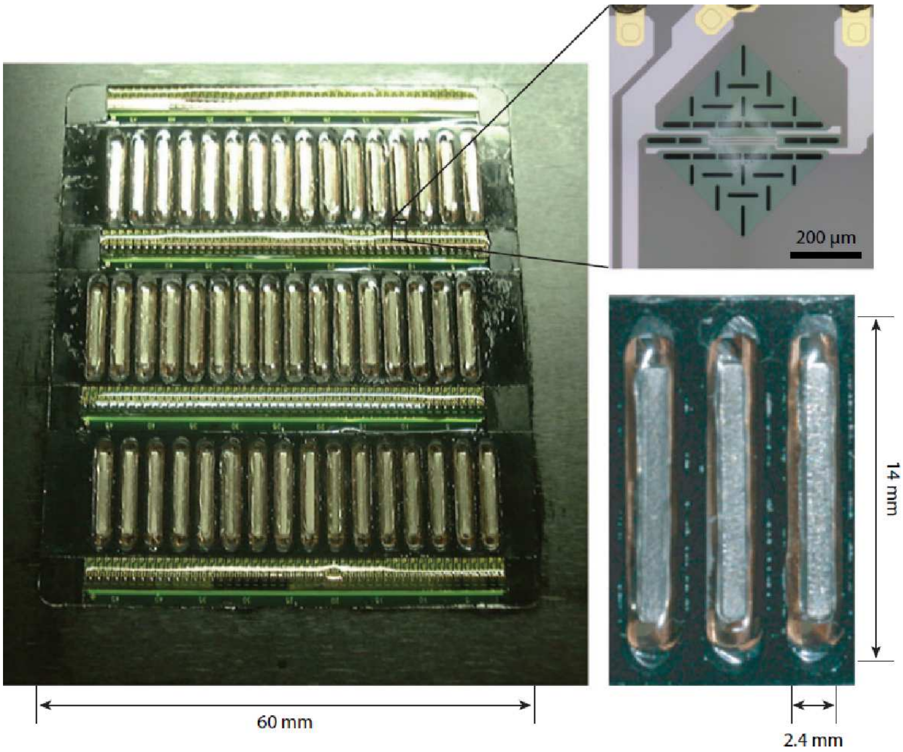

Figure 2.16: Feedback control system with arrayed hot-film sensors and wall-deformation actuators.

Chapter 3

Channel Flow Model

Channel flow at turbulent Reynolds numbers is a framework of particular interest in which developing and testing proper feedback control strategy. As a matter of fact, the symmetry and simplicity offered by the geometry of a plane channel flow lead to effective implementation in DNS code. What follows is an in-depth description of the code used for numerical simulations. After that, starting from fully nonlinear Navier-Stokes equations, a linear model of the channel flow is analytically derived in order to implement an optimal control scheme.

3.1 DNS

The simple geometry of channel flow allows to set a rectangular computational domain, as outlined in Figure 3.1: a Cartesian coordinate system is introduced, where x, y and z denote the streamwise, wall-normal and spanwise directions, respectively. The velocity field is composed by the streamwise, wall-normal and spanwise components u, v and w and the pressure field is denoted by p. We call L_x the dimension of the channel along

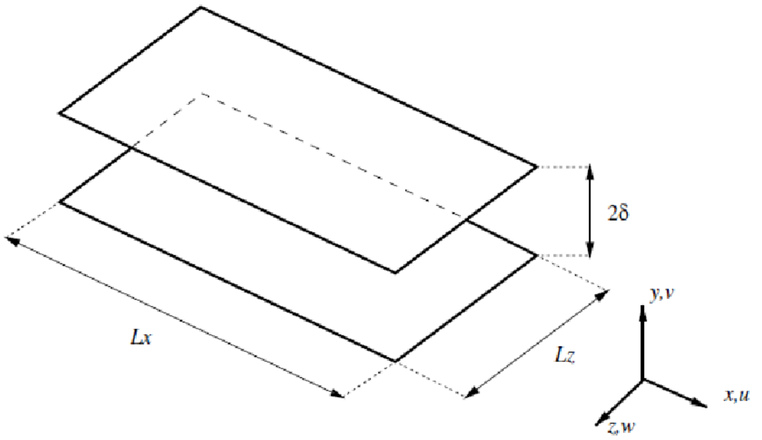

Figure 3.1: Schematic representation of the computation domain used in DNS.

x direction and L_z the dimension along z. A proper length scale one can adopt to represent such flow can be obtained from the channel half-width δ. Hence, we define Reynolds number as

$$Re = \frac{U_B \delta}{\nu} \tag{3.1}$$

where U_B is the reference bulk velocity, which is defined by the integral

$$U_B = \frac{1}{\delta} \int_0^{\delta} \bar{\mathbf{U}} dy \tag{3.2}$$

where $\bar{\mathbf{U}}$ is the average velocity field. For the sake of simplicity, we will always take the channel half-width equal to the unity. With these definitions, the nondimensionalized Navier-Stokes equations for incompressible flows appear as follows:

$$\begin{cases} \dfrac{\partial u}{\partial x} + \dfrac{\partial v}{\partial y} + \dfrac{\partial w}{\partial z} = 0 & \text{(3.3a)} \\ \dfrac{\partial u}{\partial t} + u\dfrac{\partial u}{\partial x} + v\dfrac{\partial u}{\partial y} + w\dfrac{\partial u}{\partial z} = -\dfrac{\partial p}{\partial x} + \dfrac{1}{Re}\Delta u & \text{(3.3b)} \\ \dfrac{\partial v}{\partial t} + u\dfrac{\partial v}{\partial x} + v\dfrac{\partial v}{\partial y} + w\dfrac{\partial v}{\partial z} = -\dfrac{\partial p}{\partial y} + \dfrac{1}{Re}\Delta v & \text{(3.3c)} \\ \dfrac{\partial w}{\partial t} + u\dfrac{\partial w}{\partial x} + v\dfrac{\partial w}{\partial y} + w\dfrac{\partial w}{\partial z} = -\dfrac{\partial p}{\partial z} + \dfrac{1}{Re}\Delta w & \text{(3.3d)} \end{cases}$$

where Equation (3.3a) represents continuity equation, while Equations (3.3b)-(3.3d) represent the conservation of momentum. The problem is closed by assigning an initial condition for the flow field, no-slip boundary conditions at walls and periodic boundary conditions on the unbounded portion of the domain. This scheme is the starting point in the implementation of DNS. The code used in the present work is the one developed by Quadrio and Luchini, described in [48]. The programming language adopted has been written by Paolo Luchini and is called CPL, with which it possible to exploit C, C++ and Fortran commands in the same environment.

The approach to DNS is based on the pioneering work [37], which has become a standard technique in numerical simulations of turbulent flows. It consists of replacing the nondimensionalized Navier-Stokes for incompressible flows in Cartesian coordinates (3.3) with two scalar equations, one for the normal component of the velocity v and one for the normal component of the vorticity η, which is defined as

$$\eta = \frac{\partial u}{\partial z} - \frac{\partial w}{\partial x} \tag{3.4}$$

The equation for wall-normal vorticity can be easily obtained by taking the y-component of the curl of (3.3c). Then, after Fourier-transforming, we get

$$\frac{\partial \hat{\eta}}{\partial t} = \frac{1}{Re}[D_2(\hat{\eta}) - k^2 \hat{\eta}] + j\beta \widehat{HU} - j\alpha \widehat{HW} \tag{3.5}$$

where $D_n(.)$ is the n-th order derivative operator in y direction and $k^2 = \alpha^2 + \beta^2$, where

α and β are wavenumbers in Fourier domain. As for hat sign, it will be considered here, as in the rest of the work, to indicate a variable in Fourier domain. After that, the nonlinear terms which come from Fourier-transforming the convective part of Navier-Stokes equations are grouped together in the following definitions:

$$\begin{aligned} \widehat{HU} &= j\alpha\widehat{uu} + D_1(\widehat{uv}) + j\beta\widehat{uw} \\ \widehat{HV} &= j\alpha\widehat{uv} + D_1(\widehat{vv}) + j\beta\widehat{vw} \\ \widehat{HW} &= j\alpha\widehat{uw} + D_1(\widehat{vw}) + j\beta\widehat{ww} \end{aligned} \tag{3.6}$$

As for the equation for wall-normal velocity, it is determined by summing (3.3b), derived two times w.r.t. x and y, and (3.3d), derived w.r.t. y and z, then subtracting (3.3c) derived twice by x and (3.3c) again derived twice by z. After some algebraic manipulations, we get the following fourth-order equation:

$$\frac{\partial}{\partial t}[D_2(\hat{v}) - k^2\hat{v}] = \frac{1}{Re}[D_4(\hat{v}) - 2k^2 D_2(\hat{v}) + k^4\hat{v}] - k^2\widehat{HV} - D_1(j\alpha\widehat{HU} + j\beta\widehat{HW}) \tag{3.7}$$

Since the equations are written in Fourier domain, unknowns v and η are represented in the form of truncated Fourier series in the homogeneous directions x and z, as follows:

$$v(x,\, y,\, z,\, t) = \sum_{h=-N_x/2}^{N_x/2} \sum_{l=-N_z/2}^{N_z/2} \hat{v}_{hl}(y,\, t) e^{j\alpha_0 hx} e^{j\beta_0 lz} \tag{3.8}$$

where N_x and N_z are the higher wavenumbers at which the discrete Fourier transform has been truncated, h and l are integer variables which span Fourier space in streamwise and spanwise directions, respectively, while α_0 and β_0 are the corresponding fundamental wavenumbers, defined as $\alpha_0 = 2\pi/L_x$ and $\beta_0 = 2\pi/L_z$. We can easily notice that Equations (3.5) and (3.7) are uncoupled if the nonlinear terms are known, e.g. by treating them explicitly in time discretization. Thus, they can be solved separately to advance the solution in time. However, in order to compute the nonlinear terms, we need to compute $\hat{u}$ and $\hat{w}$. By combining the equation for vorticity η and continuity equation in Fourier space we can determine $\hat{u}$ and $\hat{w}$ by solving the following 2×2 algebraic system

$$\begin{cases} \hat{u} = \dfrac{1}{k^2}[j\alpha D_1(\hat{v}) - j\beta\hat{\eta}] \\ \hat{w} = \dfrac{1}{k^2}[j\beta D_1(\hat{v}) + j\alpha\hat{\eta}] \end{cases} \tag{3.9}$$

The numerical evaluation of velocity products would require computationally expensive convolutions in wavenumber space, hence a more efficient way has been proposed, based on inverse Fourier-transforming the quantities of interest into physical domain, where convolutions are replaced by products, thus re-transforming into wavenumber space, using Fast-Fourier-Transform (FFT) algorithms in both directions. In order to preserve spectral accuracy, a de-aliasing factor of 3/2 is introduced to expand the number of collocation points before transforming from wavenumber to physical space.

3.1.1 Time discretization

The following step involves time integration of Equations (3.5) and (3.7) by adopting a semi-implicit method, paying some attention to memory requirements. The most stability-limiting part of the equations, i.e. the viscous part, is advanced with an implicit second-order Crank-Nicolson scheme. This relieves the constraint on the time-step size Δt, that is solely determined by the explicit third-order low-storage Runge-Kutta method used for advancing nonlinear terms, which can thus benefit from a higher precision. After time discretization, Equations (3.5) and (3.7) appear as follows:

$$\begin{aligned}
&\frac{\lambda}{\delta t}\hat{\eta}_{hl}^{n+1} - \frac{1}{Re}\left[D_2(\hat{\eta}_{hl}^{n+1}) - k^2\hat{\eta}_{hl}^{n+1}\right] = \\
&\quad = \frac{\lambda}{\delta t}\hat{\eta}_{hl}^{n} - \frac{1}{Re}\left[D_2(\hat{\eta}_{hl}^{n}) - k^2\hat{\eta}_{hl}^{n}\right] + \\
&\qquad + \theta\left(j\beta_0 l\widehat{HU}_{hl} - j\alpha_0 h\widehat{HW}_{hl}\right)^n + \xi\left(j\beta_0 l\widehat{HU}_{hl} - j\alpha_0 h\widehat{HW}_{hl}\right)^{n-1}
\end{aligned} \tag{3.10}$$

$$\begin{aligned}
&\frac{\lambda}{\delta t}\left(D_2(\hat{v}_{hl}^{n+1}) - k^2\hat{v}_{hl}^{n+1}\right) - \frac{1}{Re}\left[D_4(\hat{v}_{hl}^{n+1}) - 2k^2D_2(\hat{v}_{hl}^{n+1}) + k^4\hat{v}_{hl}^{n+1}\right] = \\
&\quad = \frac{\lambda}{\delta t}\left[D_2(\hat{v}_{hl}^{n}) - k^2\hat{v}_{hl}^{n}\right] - \frac{1}{Re}\left[D_4(\hat{v}_{hl}^{n}) - 2k^2D_2(\hat{v}_{hl}^{n}) + k^4\hat{v}_{hl}^{n}\right] + \\
&\qquad + \theta\left[-k^2\widehat{HV}_{hl} - D_1(j\alpha_0 h\widehat{HU}_{hl} + j\beta_0 l\widehat{HW}_{hl})\right]^n + \\
&\qquad + \theta\left[-k^2\widehat{HV}_{hl} - D_1(j\alpha_0 h\widehat{HU}_{hl} + j\beta_0 l\widehat{HW}_{hl})\right]^{n-1}
\end{aligned} \tag{3.11}$$

Coefficients λ, θ and ξ appearing in the equations, take different values according to the integration scheme one can choose. In order to achieve higher accuracy in the solution, each time-step Δt is divided into three substeps δt_i and solved with different coefficients λ_i, θ_i and ξ_i. Hence, at each substep the discrete equations are solved by assembling the RHSs corresponding to the explicit part. As previously mentioned, velocity products appearing in nonlinear terms are computed through direct/inverse FFT in wall-parallel planes. Then, for each wavenumber pair (α, β), we need to solve a set of two ODEs derived from the implicit formulation of viscous terms. In order to provide a discrete solution of the resulting ODEs, a compact finite difference discretization has been introduced for wall-normal differential operators, so to guarantee spectral accuracy. Such discretization produces two linear systems with real banded matrices, whose solution gives $\hat{\eta}_{hl}^{n+1}$ and $\hat{v}_{hl}^{n+1}$, from which we can easily recover the other velocity components $\hat{u}_{hl}^{n+1}$ and $\hat{w}_{hl}^{n+1}$ from (3.9). Unlike the procedure adopted to build the RHS, this second step proceeds per wall-normal lines, since the simultaneous knowledge of the RHS in all y positions is required.

3.1.2 Compact finite difference scheme

The discretization of first, second and fourth order wall-normal derivatives required for the solution of the problem has been performed using a compact finite differences scheme. This is a major difference with respect to [37], which instead proposed a spectral derivatives approach that provides spectral accuracy but suffers from low parallelization.

The basic idea of compact differences scheme consists of approximating the derivative of a function at each grid point with a linear combination of the function evaluated on a set of nodes in the neighborhood of such grid point. For further details, the interested reader is referred to the exhaustive work of Lele [44]. As for the present implementation, a five grid points stencil has been used to discretize the derivative operator in order to achieve at least fourth-order accuracy. So, for each grid point y_j, the five coefficients $D_n^j(i)$ of the n-th order centered derivative operator are determined as follows:

$$D_n(f(y))|_{y=y_j} = \sum_{i=-2}^{2} D_n^j(i) f(y_{j+i}) \tag{3.12}$$

Usually, the main drawback of compact differences schemes is their implicit formulation which requires the inversion of a linear system for the approximation of every derivative at each grid point if different spacing is applied to the mesh grid. In the present case, however, it is possible to explicitly pre-determine the coefficients. This important simplification has been firstly highlighted in the original Gauss-Jackson-Numerov compact formulation exploited in his seminal work by Thomas [70], concerning the numerical solution of the Orr-Sommerfeld equation. To illustrate Thomas' method let us consider a fourth-order ordinary differential equation for a function $f(y)$ in the form

$$D_4(a_4 f) + D_2(a_2 f) + D_1(a_1 f) + a_0 f = g \tag{3.13}$$

where the coefficients $a_i(y)$ are arbitrary functions of the independent variable y and $g(y)$ is the known RHS. Now suppose that a differential operator in frequency space, say D_4 for example, is approximated as the ratio of two polynomials $\mathcal{D}_4$ and $\mathcal{D}_0$ which have both a counterpart in physical space, namely d_4 and d_0. Hence, if we are able to prove that all the differential operators in the differential equation admit a representation in which the polynomial $\mathcal{D}_0$ at the denominator remains the same, then Equation (3.13) can be recast into the equivalent form

$$d_4(a_4 f) + d_2(a_2 f) + d_1(a_1 f) + d_0(a_0 f) = d_0(g) \tag{3.14}$$

Actually, this alternative formulation is possible if in a fourth-order ODE the third-order derivative operator is not present, as in the present case. So, explicit finite differences schemes have been applied in the DNS code with the same order of accuracy of implicit compact finite differences operator. As for boundaries, non-standard schemes needed to be designed for computing derivatives at walls, so non-centered schemes have been developed following the same approach adopted for interior points, thus preserving by construction the formal accuracy of the method. Moreover, a mesh with variable size has been used to discretize the wall-normal direction, in order to keep track of the increasingly smaller turbulent length scales while approaching channel walls. In the

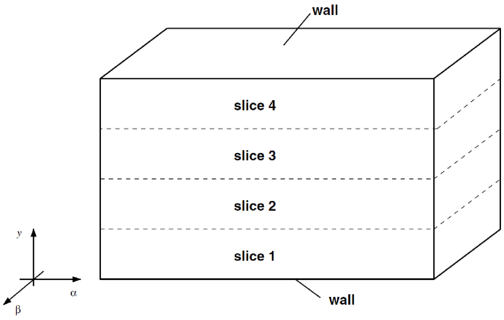

Figure 3.2: Domain slicing scheme for parallel computation.

present code, the stretching function used to generate the mesh is

$$y = \frac{\tanh a\bar{y}}{a} \tag{3.15}$$

where a is an adjustable parameter used to modify the mesh deformation and $\bar{y}$ is a mesh grid with constant spacing coming from lower to upper wall.

3.1.3 Parallel strategy

The approach previously outlined grants excellent parallelization performances, in that a compact difference discretization in wall-normal direction allows to distribute the variables in wall-parallel slices and perform direct and inverse FFTs locally at each machines. Moreover, thanks to the locality of compact difference operators, the communication required to compute wall-normal derivatives of velocity products is fairly small, since data transfer is needed only at the interface between contiguous slices. This is a major difference with respect to [37], where a fully spectral discretization was employed. Although spectral derivatives can benefit from higher accuracy, they have the significant drawback of being defined on the whole domain, thus a transposition of the whole dataset across the computing nodes is needed every time the numerical solution is advanced in time. It is worthless saying that this operation requires a large amount of communication, hence very fast networking hardware is needed to achieve good parallel performance, thus restricting DNS to be carried out only on very expensive computers only.

With compact differences scheme, transpose of the whole flow field can be avoided if data are distributed in slices parallel to the walls and each one of the p machines representing our parallel system is assigned one of these slices. The arrangement is schematically represented in Figure 3.2: each machine holds all the streamwise and spanwise wavenumbers for n_y/p positions, where n_y is the dimension of the meshgrid in y direction. In this way, a small amount of communication is required only at the interface between two continuous slices for the evaluation of the RHSs. Moreover, even this communication can be avoided if two boundary planes on each internal slice are duplicated on the neighboring slice.

The most critical part of the procedure lies in the second part of the time-step advancement, when we have to solve a set of two linear systems, one for each $(h,\, l)$ pair, since data appear to be spread over the p machines. In this case we can avoid to perform a global transpose if we adopt a LU decomposition of the pentadiagonal distributed matrices and then apply a subsequent sweep of backsubstitution, which requires the transmission of only a few coefficients at the interface between neighboring nodes. As the number of linear systems is very high, typically $(n_x + 1)(n_z + 1) \approx 10^4$ or bigger, the solution of the linear systems can be efficiently pipelined as follows. When the LU decomposition of the matrix of the system for a given pair $(h,\, l)$ is performed, there is a first loop from the top row of the matrix down to the bottom row, in order to eliminate the unknowns, then a second loop in the opposite direction. The machine owning the first slice performs the elimination in the local part of the matrix and then passes the boundary coefficients to the neighboring machine, which starts the elimination. Instead of waiting for the elimination in the $(h,\, l)$ system matrices to be completed across the machines, the first machine can start working on the elimination in the matrix of the following system. A synchronization is needed only at the end of the elimination phase, then the whole procedure can be repeated for the backsubstitution phase. This effective pipelined-linear-system strategy allows a point-to-point communication, so that each computer has to exchange information only with adjacent CPUs, allowing to adopt mass-marketed CPUs instead of dedicated servers.

This structure has been realized at the University of Salerno and has been used to perform the most expensive simulations appearing in the present work. The system in its present configuration is composed by 150 quad-core AMD Athlon and each computer is connected to the adjacent ones by two 100 MBits Fast Ethernet cards.

3.1.4 Code validation

In order to validate this DNS code the authors have compared the calculation of some meaningful statistics with results reported in [37]. In Figure 3.3 we can observe a perfect overlapping of the mean velocity profiles u^+. Good overall results have also emerged from computation of autocorrelation functions R_{uu} and R_{ww} for streamwise and spanwise component velocities, evaluated along x-direction at $y^+ = 10$, as shown in Figures 3.4 and 3.5.

3.2 Orr-Sommerfeld and Squire linear model

In order to implement an effective control scheme based on blowing/suction at walls a linear time-invariant (LTI) state space realization of the system is made necessary. In order to achieve this goal, we start by considering Navier-Stokes equations outlined in (3.3), then we split the velocity field into a reference streamwise velocity profile U and perturbations around it in streamwise, wall-normal and spanwise directions, namely u, v and w. We do the same with the pressure field, by highlighting perturbation p.

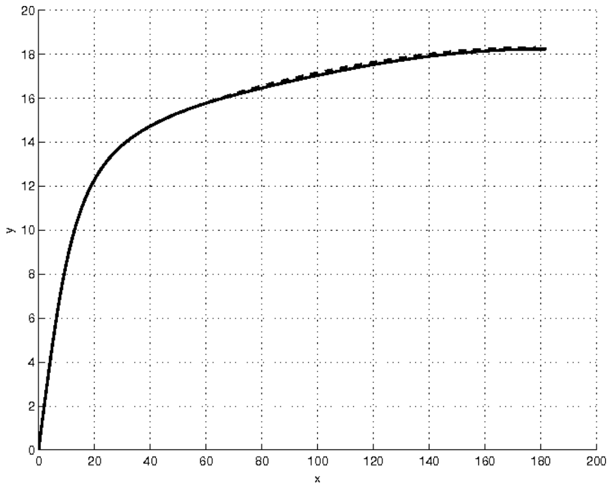

Figure 3.3: Mean velocity profile u^+: comparison between the present DNS code (solid line) and the one outlined in [37] (dashed line).

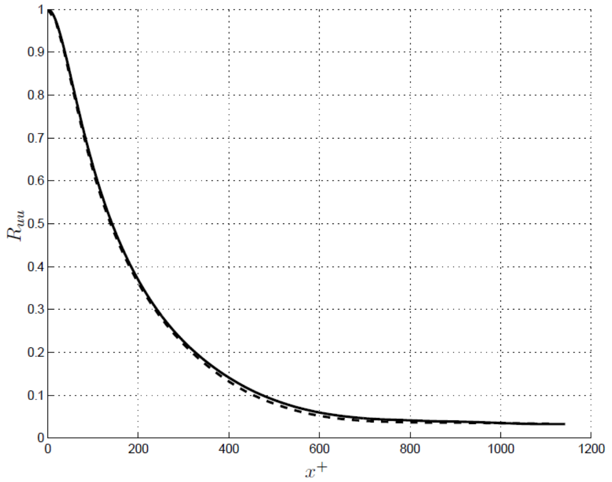

Figure 3.4: Autocorrelation function R_{uu} along x coordinate at $y^+ = 10$: comparison between the present DNS code (solid line) and the one outlined in [37] (dashed line).

Hence

$$\begin{cases} \dfrac{\partial u}{\partial x} + \dfrac{\partial v}{\partial y} + \dfrac{\partial w}{\partial z} = 0 & \text{(3.16a)} \\ \dfrac{\partial u}{\partial t} + U\dfrac{\partial u}{\partial x} + U'v + H_x = -\dfrac{\partial p}{\partial x} + \dfrac{1}{Re}\Delta u & \text{(3.16b)} \\ \dfrac{\partial v}{\partial t} + U\dfrac{\partial v}{\partial x} + H_y = -\dfrac{\partial p}{\partial y} + \dfrac{1}{Re}\Delta v & \text{(3.16c)} \\ \dfrac{\partial w}{\partial t} + U\dfrac{\partial w}{\partial x} + H_z = -\dfrac{\partial p}{\partial z} + \dfrac{1}{Re}\Delta w & \text{(3.16d)} \end{cases}$$

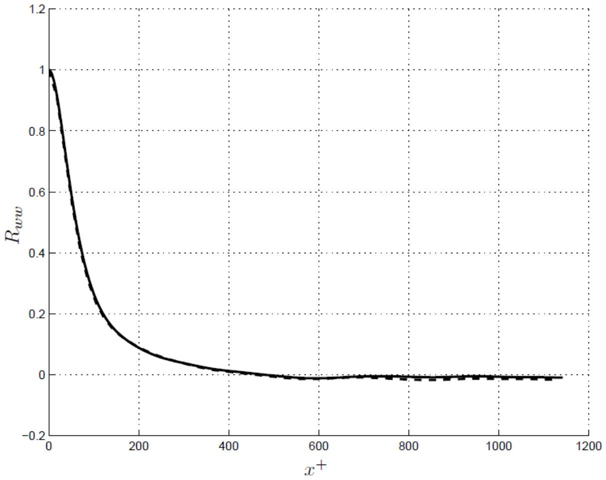

Figure 3.5: Autocorrelation function R_{ww} along x coordinate at $y^+ = 10$: comparison between the present DNS code (solid line) and the one outlined in [37] (dashed line).

where superscript $'$ denotes derivative with respect to y direction and H_x, H_y and H_z are the convective terms, defined as

$$\begin{aligned} H_x &= \mathbf{u}\nabla u \\ H_y &= \mathbf{u}\nabla v \\ H_z &= \mathbf{u}\nabla w \end{aligned} \tag{3.17}$$

where $\mathbf{u}$ represents the fluctuating velocity field (u, v, w). Following a procedure analogous to the one adopted for the implementation of DNS code, it is possible to reduce the number of equations and unknowns to a minimum of two. Firstly, we take the divergence of the vectorial momentum equation, i.e.

$$\begin{aligned} &\frac{\partial}{\partial t}\left(\frac{\partial u}{\partial x}+\frac{\partial v}{\partial y}+\frac{\partial w}{\partial z}\right)+U\frac{\partial}{\partial x}\left(\frac{\partial u}{\partial x}+\frac{\partial v}{\partial y}+\frac{\partial w}{\partial z}\right)+ \\ &\quad+2U'\frac{\partial v}{\partial x}+\left(\frac{\partial H_x}{\partial x}+\frac{\partial H_y}{\partial y}+\frac{\partial H_z}{\partial z}\right)= \\ &\quad=-\Delta p+\frac{1}{Re}\Delta\left(\frac{\partial u}{\partial x}+\frac{\partial v}{\partial y}+\frac{\partial w}{\partial z}\right) \end{aligned} \tag{3.18}$$

hence, by applying continuity, we get

$$\Delta p = -2U'\frac{\partial v}{\partial x} - \left(\frac{\partial H_x}{\partial x}+\frac{\partial H_y}{\partial y}+\frac{\partial H_z}{\partial z}\right) \tag{3.19}$$

Now, if we take the Laplacian of Equation (3.16c), we have that

$$\left(\frac{\partial}{\partial t}+U\frac{\partial}{\partial x}\right)\Delta v + U''\frac{\partial v}{\partial x} + \Delta H_y = -\frac{\partial}{\partial y}\Delta p + \frac{1}{Re}\Delta\Delta v \tag{3.20}$$

After substitution of (3.19) into (3.20) and reordering, we finally obtain

$$\left[\left(\frac{\partial}{\partial t}+U\frac{\partial}{\partial x}\right)\Delta-U''\frac{\partial}{\partial x}-\frac{1}{Re}\Delta\Delta\right]v=d_v \tag{3.21}$$

where with d_v we have considered all the nonlinear terms appearing in the equation, i.e.

$$d_v=\left(\frac{\partial H_x}{\partial x}+\frac{\partial H_y}{\partial y}+\frac{\partial H_z}{\partial z}\right)-\Delta H_y \tag{3.22}$$

To obtain the second equation, we have to subtract Equation (3.16d), derived with respect to x, to Equation (3.16b), derived with respect to z, as follows:

$$\begin{aligned}\frac{\partial}{\partial t}\left(\frac{\partial u}{\partial z}-\frac{\partial w}{\partial x}\right)+U\frac{\partial}{\partial x}\left(\frac{\partial u}{\partial z}-\frac{\partial w}{\partial x}\right)+U'\frac{\partial v}{\partial z}+\left(\frac{\partial H_x}{\partial z}-\frac{\partial H_z}{\partial x}\right)=\\=-\frac{\partial^2 p}{\partial x\partial z}+\frac{\partial^2 p}{\partial x\partial z}+\frac{1}{Re}\Delta\left(\frac{\partial u}{\partial z}-\frac{\partial w}{\partial x}\right)\end{aligned} \tag{3.23}$$

Now, if we introduce the definition of wall-normal vorticity η (3.4), we find

$$\left(\frac{\partial}{\partial t}+U\frac{\partial}{\partial x}-\frac{1}{Re}\Delta\right)\eta+U'\frac{\partial v}{\partial z}=d_\eta \tag{3.24}$$

where d_η contains the nonlinear terms, i.e.

$$d_\eta=\left(\frac{\partial H_x}{\partial z}-\frac{\partial H_z}{\partial x}\right) \tag{3.25}$$

The set of Navier-Stokes equations in v-η formulations now appears as follows:

$$\left\{\begin{array}{ll}\left[\left(\frac{\partial}{\partial t}+U\frac{\partial}{\partial x}\right)\Delta-U''\frac{\partial}{\partial x}-\frac{1}{Re}\Delta\Delta\right]v=d_v & \text{(3.26a)}\\ \left(\frac{\partial}{\partial t}+U\frac{\partial}{\partial x}-\frac{1}{Re}\Delta\right)\eta+U'\frac{\partial v}{\partial z}=d_\eta & \text{(3.26b)}\end{array}\right.$$

Now, it is useful to exploit the spatial invariance of Equations (3.26) with respect to translation in directions x and z, by Fourier-transforming in these directions. The field variables v and η, in Fourier space become

$$v(x,\,y,\,z,\,t)=\sum_{n_x=-\infty}^{\infty}\sum_{n_z=-\infty}^{\infty}\hat{v}(n_x,\,y,\,n_z,\,t)e^{j\frac{2\pi n_x x}{L_x}}\,e^{j\frac{2\pi n_z z}{L_z}} \tag{3.27}$$

$$\eta(x,\,y,\,z,\,t)=\sum_{n_x=-\infty}^{\infty}\sum_{n_z=-\infty}^{\infty}\hat{\eta}(n_x,\,y,\,n_z,\,t)e^{j\frac{2\pi n_x x}{L_x}}\,e^{j\frac{2\pi n_z z}{L_z}} \tag{3.28}$$

where Fourier coefficients are defined as follows:

$$\hat{v}(n_x,\, y,\, n_z,\, t) = \frac{1}{L_x L_z} \int_0^{L_x} \int_0^{L_z} v(x,\, y,\, z,\, t)\, e^{-j\frac{2\pi n_x x}{L_x}}\, e^{-j\frac{2\pi n_z z}{L_z}}\, dz\, dx \tag{3.29}$$

$$\hat{\eta}(n_x,\, y,\, n_z,\, t) = \frac{1}{L_x\, L_z} \int_0^{L_x} \int_0^{L_z} v(x,\, y,\, z,\, t)\, e^{-j\frac{2\pi n_x x}{L_x}}\, e^{-j\frac{2\pi n_z z}{L_z}}\, dz\, dx \tag{3.30}$$

If we define the streamwise and spanwise wavenumbers $\alpha = \frac{2\pi n_x}{L_x}$ and $\beta = \frac{2\pi n_z}{L_z}$, after Fourier-transforming, we get

$$\begin{cases} \hat{\Delta}\dot{\hat{v}} = \left(-j\alpha U\hat{\Delta} + j\alpha U'' + \dfrac{1}{Re}\hat{\Delta}\hat{\Delta}\right)\hat{v} + \hat{d}_v & \text{(3.31a)} \\ \dot{\hat{\eta}} = (-j\beta U')\,\hat{v} + \left(-j\alpha U + \dfrac{1}{Re}\hat{\Delta}\right)\hat{\eta} + \hat{d}_\eta & \text{(3.31b)} \end{cases}$$

where $\hat{\Delta} = D_2(.) - k^2$, with $D_2(.) = \partial^2/\partial y^2$ and $k^2 = \alpha^2 + \beta^2$. In order to discretize the derivatives operators in wall-normal direction D_i different solutions have been developed, which are outlined in Section 3.3. Then, if we consider just the linear part, Equations (3.31) represent the well-known Orr-Sommerfeld and Squire equations, that in operator form read

$$\begin{gathered} \begin{bmatrix} \hat{\Delta} & 0 \\ 0 & I \end{bmatrix} \begin{bmatrix} \dot{\hat{v}} \\ \dot{\hat{\eta}} \end{bmatrix} = \begin{bmatrix} \hat{L}_{OS} & 0 \\ \hat{L}_C & \hat{L}_{SQ} \end{bmatrix} \begin{bmatrix} \hat{v} \\ \hat{\eta} \end{bmatrix} \\ M\dot{\hat{x}} = L\hat{x} \\ \dot{\hat{x}} = M^{-1}L\hat{x} = N\hat{x} \end{gathered} \tag{3.32}$$

Assuming modes with exponential time dependence, this system becomes an eigenvalue problem with two distinct solution families, the first one of which contains the Orr-Sommerfeld modes, which involve eigensolutions of the equation for wall-normal velocity (3.31a). The least-stable Orr-Sommerfeld mode represents the so-called Tollmien-Schlichting waves. These two-dimensional waves can experiment exponential growth at subcritical Reynolds numbers, i.e. for $Re < 5772$, subsequently falling into secondary instability to small-amplitude three-dimensional perturbations, thus causing the flow to rapidly evolve into a fully turbulent state.

The second family of solutions contains the Squire modes and has zero wall-normal velocity. Unlike Orr-Sommerfeld modes, Squire modes are always damped. To prove that, we consider Squire equation without the forcing term in v, i.e.

$$\left(\frac{\partial}{\partial t} + j\alpha U - \frac{1}{Re}\hat{\Delta}\right)\hat{\eta} = 0 \tag{3.33}$$

and we impose an exponential solution of the type

$$\hat{\eta}(y,\, t) = \tilde{\eta}(y)\, e^{-j\alpha c t} \tag{3.34}$$

where c represents complex phase speed. After substitution of Equation (3.34) into (3.33), we obtain

$$(U - c)\tilde{\eta} - \frac{1}{j\alpha Re}\hat{\Delta}\tilde{\eta} = 0 \tag{3.35}$$

After multiplication by complex conjugate $\bar{\tilde{\eta}}$ and integration over the domain $y \in [-1, 1]$, we find

$$c\int_{-1}^{1} \bar{\tilde{\eta}}\tilde{\eta}\, dy = \int_{-1}^{1} U\bar{\tilde{\eta}}\tilde{\eta}\, dy - \frac{j}{\alpha Re}\int_{-1}^{1} \bar{\tilde{\eta}}\hat{\Delta}\tilde{\eta}\, dy \tag{3.36}$$

By taking just the imaginary part of the previous equation, we demonstrate the thesis:

$$c_i\int_{-1}^{1} |\tilde{\eta}|^2\, dy = -\frac{1}{\alpha Re}\int_{-1}^{1} (|D\tilde{\eta}|^2 + |k\tilde{\eta}|^2)\, dy < 0 \tag{3.37}$$

3.3 Discretization of derivatives operators

In order to discretize the derivatives in the wall-normal direction two different approaches have been developed and compared: finite differences and spectral derivatives. What follows is a detailed description of these two schemes.

3.3.1 Finite differences

Finite differences (FD) approach computes the approximation of the k-th order derivative of the function $f(y)$ we want to derive at each grid point y_j using a Taylor series expansion of the function f at an arbitrary stencil $n \geq k+1$ of points $y_1, \ldots, y_i, \ldots, y_n$ in the neighborhood of y_j. Now, let us consider for simplicity an equally spaced grid, then we will provide the generalization to arbitrary grid spacing. The key idea is to use a linear combination of Taylor series expansion of the function at stencil points $x_1 f(y_1) + x_2 f(y_2) + \cdots + x_n f(y_n)$ in order to achieve the approximation of derivative $f^k(y_j)$ with the maximum order of accuracy. This goal will help us to impose the conditions to determine the coefficients $x_1, x_2, \ldots, x_n$. In order to illustrate the key idea we will provide two different examples.

As for the first example, we consider the approximation of first derivative $f'(y)$ at point y_j with a stencil $n = 3$ centered around the point y_j on a grid of spacing h. We have

$$f'(y_j) = x_1 f(y_j - h) + x_2 f(y_j) + x_3 f(y_j + h) \tag{3.38}$$

Taylor series expansion of each term till order $n - 1$ leads to

$$\begin{aligned} f(y_j - h) &= f_j - hf'_j + \frac{1}{2}h^2 f''_j + \mathcal{O}(h^3) \\ f(y_j) &= f_j \\ f(y_j + h) &= f_j + hf'_j + \frac{1}{2}h^2 f''_j + \mathcal{O}(h^3) \end{aligned} \tag{3.39}$$

Substitution of relations (3.39) into (3.38) implies

$$f'(y_j) = (x_1 + x_2 + x_3)f_j + (x_3 - x_1)h\, f'_j + (x_3 + x_1)\frac{h^2}{2}f''_j + \mathcal{O}(h^3) \tag{3.40}$$

Hence the best approximation of first derivative is given by imposing the following conditions:

$$\begin{cases} x_1 + x_2 + x_3 = 0 \\ -\,hx_1 + hx_3 = 1 \\ \dfrac{h^2}{2}x_1 + \dfrac{h^2}{2}x_3 = 0 \end{cases} \tag{3.41}$$

These conditions can be represented through an equivalent linear system

$$\begin{bmatrix} 1 & 1 & 1 \\ -h & 0 & h \\ h^2 & 0 & h^2 \end{bmatrix} \begin{bmatrix} x_1 \\ x_2 \\ x_3 \end{bmatrix} = \begin{bmatrix} 0 \\ 1 \\ 0 \end{bmatrix} \tag{3.42}$$

Solution of the system (3.42) leads to

$$x_1 = -\frac{1}{2h}, \qquad x_2 = 0, \qquad x_3 = \frac{1}{2h} \tag{3.43}$$

With this finite differences scheme, the error due to truncation of Taylor series is readily available and its order of magnitude is equal to $\mathcal{O}(h^3)$. Finally, the centered approximation of the first derivative of function $f(y)$ discretized over an equally spaced grid is given by

$$f'(y_j) = \frac{f(y_j + h) - f(y_j - h)}{2h} \tag{3.44}$$

As for the second example, we want to implement an uncentered finite difference scheme to compute the approximation of second order derivative. Thus, by following the same steps of the previous example, we have

$$f''(y_j) = x_1 f(y_j) + x_2 f(y_j + h) + x_3 f(y_j + 2h) \tag{3.45}$$

Then, expanding the terms into Taylor series and imposing the condition of approximating the derivative with the minimum truncation error lead to the following linear system:

$$\begin{cases} x_1 + x_2 + x_3 = 0 \\ hx_2 + 2hx_3 = 1 \\ \dfrac{h^2}{2}x_2 + 2h^2x_3 = 2 \end{cases} \tag{3.46}$$

hence

$$\begin{bmatrix} 1 & 1 & 1 \\ 0 & h & 2h \\ 0 & h^2 & 4h^2 \end{bmatrix} \begin{bmatrix} x_1 \\ x_2 \\ x_3 \end{bmatrix} = \begin{bmatrix} 0 \\ 0 \\ 4 \end{bmatrix} \tag{3.47}$$

The solution of the system is

$$x_2 = \frac{1}{h^2}, \qquad x_2 = -\frac{2}{h^2}, \qquad x_3 = \frac{1}{h^2} \tag{3.48}$$

So, the uncentered approximation of the second-order derivative of function $f(y)$ discretized over an equally spaced grid is given by

$$f''(y_j) = \frac{f(y_j) - 2f(y_j + h) + f(y_j + 2h)}{h^2} \tag{3.49}$$

From these examples, we can infer that the linear system that has to be solved for determining the interpolant coefficients $x_1, \ldots, x_n$ that approximate a k-th order derivative with a stencil of n is given by a proper partition of the following Vandermonde matrix:

$$\begin{bmatrix} \ldots & (-2h)^0 & (-h)^0 & 1 & (h)^0 & (2h)^0 & \ldots \\ \ldots & (-2h)^1 & (-h)^1 & 0 & (h)^1 & (2h)^1 & \ldots \\ \ldots & (-2h)^2 & (-h)^2 & 0 & (h)^2 & (2h)^2 & \ldots \\ \ldots & (-2h)^3 & (-h)^3 & 0 & (h)^3 & (2h)^3 & \ldots \\ & \vdots & \vdots & \vdots & \vdots & \vdots & \end{bmatrix} \tag{3.50}$$

The solution of the system is then recovered by considering a number of rows and columns equal to the stencil n. The choice of which columns we have to take depends on the finite difference scheme: if we consider a centered scheme, then for n odd, we must take the columns going from $-(n-1)/2$ to $(n-1)/2$, while if the scheme is uncentered, then the columns to choose are a shifted version of the previous ones, depending on the degree of decentralization. Thus, a single linear system is sufficient to completely determine the derivatives of all grid points. As a matter of fact, if A is the proper partition of Vandermonde matrix (3.50), the vector of unknown coefficients $x = \left[\begin{smallmatrix} x_1 & x_2 & \cdots & x_n \end{smallmatrix}\right]^T$ can be recovered as $Ax = k!\, e_{k+1}$, where e_{k+1} is a vector of zeros with 1 in row $k+1$. Unfortunately, Vandermonde matrices are well-known for being highly ill-conditioned, so this technique is particularly amenable only for low n. However, it is to remark that this drawback actually is not a very limiting one, since usually a stencil of 5-7 points is sufficient to discretize the system with high accuracy.

The case of unequally spaced grid leads to the definition of a Vandermonde matrix for each grid point y_j, with the major difference that spacing h is replaced by the actual spacing $y_{j+1} - y_j$, in this way:

$$\begin{bmatrix} \ldots & (y_{j-2} - y_j)^0 & (y_{j-1} - y_j)^0 & 1 & (y_{j+1} - y_j)^0 & (y_{j+2} - y_j)^0 & \ldots \\ \ldots & (y_{j-2} - y_j)^1 & (y_{j-1} - y_j)^1 & 0 & (y_{j+1} - y_j)^1 & (y_{j+2} - y_j)^1 & \ldots \\ \ldots & (y_{j-2} - y_j)^2 & (y_{j-1} - y_j)^2 & 0 & (y_{j+1} - y_j)^2 & (y_{j+2} - y_j)^2 & \ldots \\ \ldots & (y_{j-2} - y_j)^3 & (y_{j-1} - y_j)^3 & 0 & (y_{j+1} - y_j)^3 & (y_{j+2} - y_j)^3 & \ldots \\ \ldots & (y_{j-2} - y_j)^4 & (y_{j-1} - y_j)^4 & 0 & (y_{j+1} - y_j)^4 & (y_{j+2} - y_j)^4 & \ldots \\ & \vdots & \vdots & \vdots & \vdots & \vdots & \end{bmatrix} \tag{3.51}$$

The procedure to extract matrix A is the same described before, the major difference is that now it is required to solve N linear systems of size $n \times n$, instead of one. Differentiation matrices arising from finite difference schemes are always band matrices, whose size of the band corresponds to the stencil n we have chosen. For this reason, finite differences are particularly amenable to sparse solver algorithms for the solution of ODEs. As for the order of accuracy, it is strictly related to the stencil because the higher the stencil, then the lower the truncation error can be set. So, if we define $\bar{h}$ as an average mesh grid, then it can be proved that there always exists a constant $C > 0$ so that the order of accuracy is $\mathcal{O}(C\bar{h}^{n+1})$.

3.3.2 Spectral derivatives

Spectral derivatives (SD) schemes have been implemented using the Matlab Differentiation Matrix Suite developed by Weiderman and Reddy and widely described in [72]. This approach adopts a spectral collocation method in order to build a weighted interpolation of the function to be derived $f(y)$ over a set of nodes $\{y_j\}_{j=1}^{N}$, i.e.

$$f(y) \approx p_{N-1}(y) = \sum_{j=1}^{N} \alpha(y)\phi_j(y)f(y_j) \tag{3.52}$$

where $\alpha(y)$ is a weight function and the set of interpolating functions $\{\phi_j(y_j)\}_{j=1}^{N}$ satisfies $\phi_j(y_k) = \delta_{jk}$ (the Kronecker delta). This means that $p_{N-1}(y)$ is an interpolant of $f(y)$ in the sense that the following equivalence holds at every node:

$$f(y_j) = p_{N-1}(y_j), \qquad j = 1, \ldots, N \tag{3.53}$$

Spectral derivatives are set up from Equation (3.52) by considering, as shown in [10]

$$\alpha(y) = 1 \tag{3.54}$$

$$\phi_j(y) = \frac{(-1)^j}{c_j} \frac{1-y^2}{(N-1)^2} \frac{T'_{N-1}(y)}{y-y_j} \tag{3.55}$$

$$p_{N-1}(y) = \sum_{j=1}^{N} \phi_j(y)f(y_j) \tag{3.56}$$

where $c_1 = c_N = 2$, $c_2 = \cdots = c_{N-1} = 1$ and $T_{N-1}(y)$ is the Chebyshev polynomial of degree $N-1$, defined as

$$T_j(y) = \cos(j \arccos y) \tag{3.57}$$

Interpolation points are the well-known Gauss-Lobatto-Chebyshev nodes, which are defined as follows:

$$y_j = \cos\frac{(k-1)\pi}{N-1} \qquad k = 1, \ldots, N \tag{3.58}$$

Differentiation matrices are then obtained through derivation of the polynomial interpolator. For the first derivative D_1, we get

$$D_1^{k\,j} = \begin{cases} \dfrac{c_k(-1)^{j+k}}{c_j(y_k - y_j)} & j \neq k \\ -\dfrac{1}{2}\dfrac{y_k}{(1-y_k^2)} & j = k \neq 1,\, N \\ \dfrac{2(N-1)^2+1}{6} & j = k = 1 \\ -\dfrac{2(N-1)^2+1}{6} & j = k = N \end{cases} \tag{3.59}$$

where $D_1^{k\,j}$ represents the element of matrix D_1 with indexes $(k,\, j)$. Higher order derivatives are then computed as power of D_1, i.e. if l is the order of the derivative, then $D_l = (D_1)^l$. Unlike finite difference schemes, spectral derivatives have the relevant property that the discretization error converges exponentially upon grid refinement. In particular, if N is the number of grid points, then it can be proved that there always exists a constant $C > 0$, so that the order of accuracy is $\mathcal{O}(e^{-C\,N})$. The price to pay is that this method generates full matrices, so faster sparse solvers are no longer available.

3.3.3 Benchmark problem for the proposed derivation schemes

In order to test the performances of the above mentioned derivation schemes and show how boundary conditions are imposed, we will compare the analytical solution of a fourth-order inhomogeneous ordinary differential equation to its numerical solutions. We consider $f(y)$ as the unknown function defined over the domain $y \in [-1,\, 1]$ and the following differential equation

$$f^{IV}(y) + 10f^{III}(y) + 35f''(y) + 50f'(y) + 24f(y) = 1728y^2 \tag{3.60}$$

with Dirichlet and Neumann clamped boundary conditions, i.e.

$$f(-1) = f(1) = f'(-1) = f'(1) = 0 \tag{3.61}$$

The analytical solution $f(y)$ can be obtained by superposition of the solution of the associated homogeneous ODE $f_h(y)$ and the particular solution $f_p(y)$. As for the homogeneous equation, we propose a solution of the type

$$f_h(y) = Ce^{\lambda y} \tag{3.62}$$

After subustitution in Equation (3.60), we find the associated characteristic equation

$$\lambda^4 + 10\lambda^3 + 35\lambda^2 + 50\lambda + 24 = 0 \tag{3.63}$$

which has four distinct real solutions:

$$\lambda_1 = -1, \quad \lambda_2 = -2, \quad \lambda_3 = -3, \quad \lambda_4 = -4 \tag{3.64}$$

hence

$$f_h(y) = C_1 e^{-1y} + C_2 e^{-2y} + C_3 e^{-3y} + C_4 e^{-4y} \tag{3.65}$$

where $C_1, \ldots, C_4$ are constants to be determined by applying boundary conditions after having determined the particular solution $f_p(y)$, which can be found by inspection:

$$f_p(y) = \bar{A}y^2 + \bar{B}y + \bar{C} \tag{3.66}$$

Substitution in (3.60) leads to

$$24\bar{A}y^2 + (100\bar{A} + 24\bar{B})y + (70\bar{A} + 24\bar{B} + 24\bar{C}) = 1728y^2 \tag{3.67}$$

Equating, term by terms, LHS and RHS, we obtain the following linear system:

$$\begin{cases} 24\bar{A} = 1728 \\ 100\bar{A} + 24\bar{B} = 0 \\ 70\bar{A} + 24\bar{B} + 24\bar{C} = 0 \end{cases} \tag{3.68}$$

from which we obtain $\bar{A} = 72$, $\bar{B} = -300$ and $\bar{C} = 415$. Hence, the full solution of the ODE reads

$$f(y) = C_1 e^{-1y} + C_2 e^{-2y} + C_3 e^{-3y} + C_4 e^{-4y} + 72y^2 - 300y + 415 \tag{3.69}$$

By imposing boundary conditions, we can recover the values of $C_1, \ldots, C_4$ from the solution of the following linear system:

$$\begin{bmatrix} e^1 & e^2 & e^3 & e^4 \\ e^{-1} & e^{-2} & e^{-3} & e^{-4} \\ e^1 & 2e^2 & 3e^3 & 4e^4 \\ e^{-1} & 2e^{-2} & 3e^{-3} & 4e^{-4} \end{bmatrix} \begin{bmatrix} C_1 \\ C_2 \\ C_3 \\ C_4 \end{bmatrix} \begin{bmatrix} -\bar{A} + \bar{B} - \bar{C} \\ -\bar{A} - \bar{B} - \bar{C} \\ -2\bar{A} + \bar{B} \\ 2\bar{A} + \bar{B} \end{bmatrix} \tag{3.70}$$

Then, we implement a finite differences scheme by choosing a stencil $n = 5$ and defining a meshgrid of $N+2$ nodes y_{-1}, y_0, y_1, $\ldots$, y_{N-1}, y_N, y_{N+1} with constant width h over the extended domain $y \in [-1-h,\, 1+h]$. Note that the fictitious nodes $y_{-1} = -1-h$ and $y_{N+1} = 1+h$ have been introduced to better account for boundary conditions. As a matter of fact, we can impose Dirichlet condition by setting $y_0 = y_N = 0$. As for Neumann conditions, we can discretize the first order derivative through an uncentered differentiation scheme:

$$\begin{aligned} D_1^{-1(+)}y_{-1} + D_1^{0(+)}y_0 + D_1^{1(+)}y_1 + D_1^{2(+)}y_2 + D_1^{3(+)}y_3 = 0 \\ D_1^{-3(-)}y_{N-3} + D_1^{-2(-)}y_{N-2} + D_1^{-1(-)}y_{N-1} + D_1^{0(-)}y_N + D_1^{1(-)}y_{N+1} = 0 \end{aligned} \tag{3.71}$$

After discretization of the four derivatives appearing in the LHS, we obtain the discrete solution $f_1, \ldots, f_{N-1}$ of ODE (3.60) by solving the following linear system:

$$\begin{gathered} \left(\frac{1}{h^4}\begin{bmatrix} 0 \\ 0 \\ D_4 \\ 0 \\ 0 \end{bmatrix} + \frac{4}{h^3}\begin{bmatrix} 0 \\ 0 \\ D_3 \\ 0 \\ 0 \end{bmatrix} + \frac{35}{h^2}\begin{bmatrix} 0 \\ 0 \\ D_2 \\ 0 \\ 0 \end{bmatrix} + \frac{50}{h}\begin{bmatrix} 0 \\ 0 \\ D_1 \\ 0 \\ 0 \end{bmatrix} + 24\begin{bmatrix} 0 \\ 0 \\ I \\ 0 \\ 0 \end{bmatrix} + \right. \\ + \frac{1}{h}\begin{bmatrix} D_1^{-1(+)} & D_1^{0(+)} & D_1^{1(+)} & D_1^{2(+)} & D_1^{3(+)} & \ldots & 0 \\ 0 & & & 0 & & & 0 \\ 0 & \ldots & D_1^{-3(-)} & D_1^{-2(-)} & D_1^{-1(-)} & D_1^{0(-)} & D_1^{1(-)} \end{bmatrix} + \\ \left. + \begin{bmatrix} 0 & 0 & 0 & \ldots & 0 & 0 & 0 \\ 0 & 1 & 0 & \ldots & 0 & 0 & 0 \\ 0 & & & 0 & & & 0 \\ 0 & 0 & 0 & \ldots & 0 & 1 & 0 \\ 0 & 0 & 0 & \ldots & 0 & 0 & 0 \end{bmatrix} \right) \begin{bmatrix} f_{-1} \\ f_0 \\ f_1 \\ \vdots \\ f_{N-1} \\ f_N \\ f_{N+1} \end{bmatrix} = \begin{bmatrix} 0 \\ 0 \\ 1728(-1+h)^2 \\ \vdots \\ 1728(1-h)^2 \\ 0 \\ 0 \end{bmatrix} \end{gathered} \tag{3.72}$$

As for spectral derivatives approach to solve ODE (3.60), it needs to be modified in order to account for clamped boundary conditions. For this reason, we must replace the weight function $\alpha(y) = 1$ in (3.52) with $\tilde{\alpha}(y) = \left[\frac{(1-y^2)^2}{(1-y_j^2)}\right]^2$. Thus, the polynomial of degree $N+1$ satisfying $N-2$ interpolation conditions and boundary conditions is

$$p_{N+1}(y) = \sum_{j=1}^{N-2} f_j \tilde{\phi}_j(y) \quad \text{with} \quad \tilde{\phi}_j(y) = \tilde{\alpha}(y) \tag{3.73}$$

After derivation of functions $\tilde{\phi}_j(y)$, we finally get the differentiation matrices.
Results have shown that the best performances are achieved by using a spectral derivatives scheme. As a matter of fact, we can see from Figure 3.6 that spectral derivatives lead to a smaller error with respect to finite differences in we consider the same number of grid point. On the other hand, finite differences show good convergence to analytical solution if further grid refinement is applied. As for the relative error committed during numerical discretization of ODE, spectral derivatives show fast exponential convergence in a double logarithmic graph, with good agreement with theretical prediction. Furthermore, it can be noticed from Figure 3.7 that in this case just 20 grid points are sufficient to reach machine precision. As for finite differences, instead, they appear to

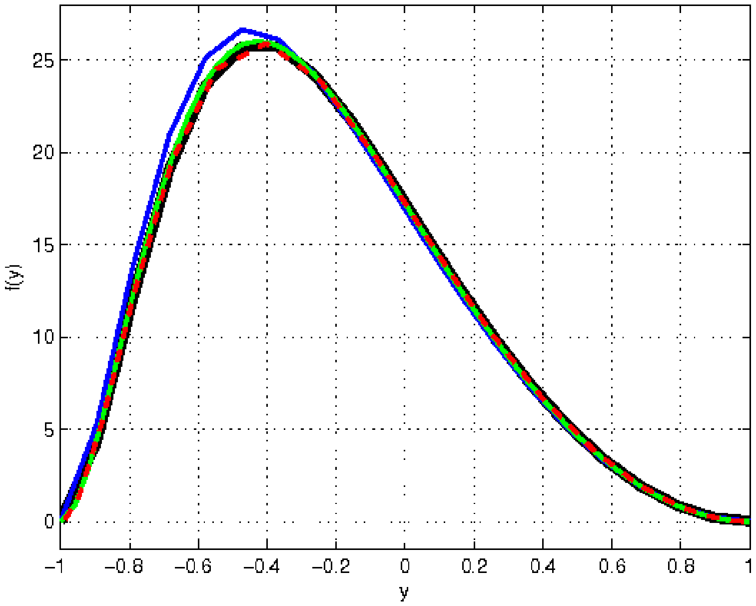

Figure 3.6: Solutions of the benchmark ODE: analytical solution (black solid line), numerical solution with FD and $N = 20$ (blue solid line), with FD and $N = 40$ (green solid line) and numerical solution with SD and $N = 20$ (red dashed line).

converge more slowly, following a linear trend according to theoretical prediction, as outlined in Figure 3.8.

3.4 Orr-Sommerfeld and Squire eigenvalues

In order to test the accuracy of the proposed discretization techniques for differential operators, we applied these two strategies for the computation of the eigenvalues of Orr-Sommerfeld and Squire equations (3.32) for a given wavenumber pair. For spectral derivatives a standard Gauss-Lobatto-Chebyshev grid was used, while for finite difference scheme we adopted an equally spaced mesh. Results have then been compared to reference data taken from literature [7], where the eigenvalues were computed for $Re = 10000$, $\alpha = 1$ and $\beta = 0$ using a Chebyshev collocation technique over a meshgrid of $N = 140$. Results show perfect correspondance with spectral derivatives with the same number of grid points, while finite differences show some misfit, which tends to zero if we increase the number of grid points, as can be stated from Tables 3.1 - 3.2 and root-loca in Figures 3.9.

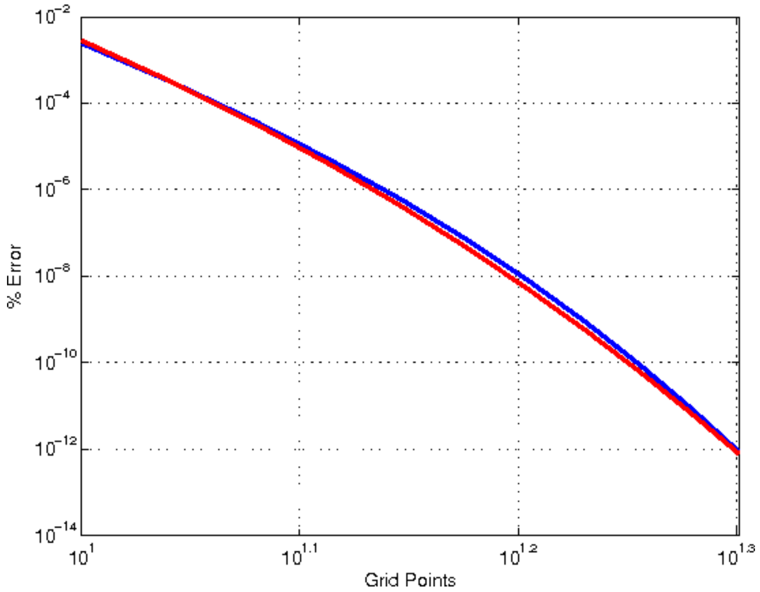

Figure 3.7: Relative error of spectral derivatives scheme upon grid refinement: numerical result (blue line) and theoretical prediction (red line).

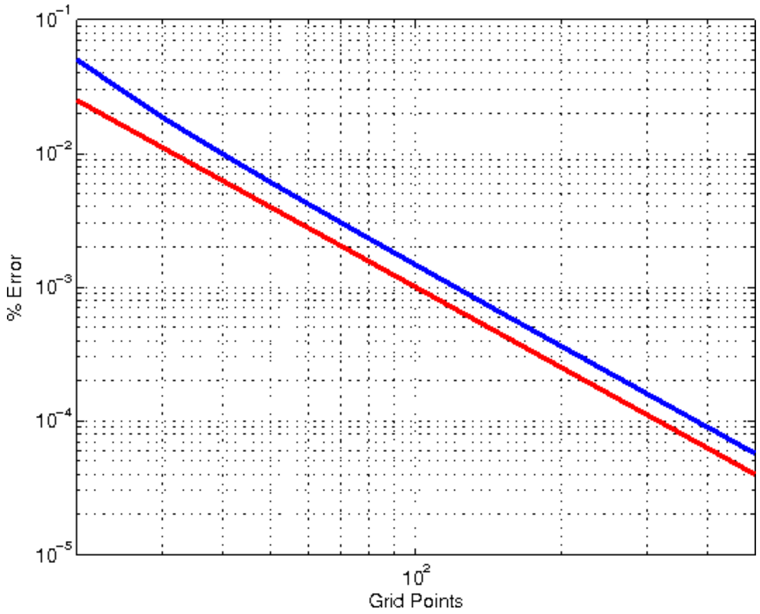

Figure 3.8: Relative error of finite differences scheme upon grid refinement: numerical result (blue line) and theoretical prediction (red line).

Eigenvalues from [7]	**Eigenvalues with spectral derivatives** ($N = 140$)
$-0.03516728 - 0.96463092\,j$	$-0.03516728 - 0.96463092\,j$
$-0.03518658 - 0.96464251\,j$	$-0.03518658 - 0.96464251\,j$
$-0.05089873 - 0.27720434\,j$	$-0.05089872 - 0.27720434\,j$
$-0.06320150 - 0.93631654\,j$	$-0.06320149 - 0.93631653\,j$
$-0.06325157 - 0.93635178\,j$	$-0.06325156 - 0.93635178\,j$
$-0.09122274 - 0.90798305\,j$	$-0.09122273 - 0.90798305\,j$
$-0.09131286 - 0.90805633\,j$	$-0.09131286 - 0.90805633\,j$
$-0.11923285 - 0.87962729\,j$	$-0.11923285 - 0.87962729\,j$
$-0.11937073 - 0.87975570\,j$	$-0.11937073 - 0.87975569\,j$
$-0.12450198 - 0.34910682\,j$	$-0.12450197 - 0.34910682\,j$
$-0.13822653 - 0.41635102\,j$	$-0.13822652 - 0.41635101\,j$
$-0.14723393 - 0.85124584\,j$	$-0.14723392 - 0.85124584\,j$
$-0.14742560 - 0.85144938\,j$	$-0.14742560 - 0.85144938\,j$
$-0.17522868 - 0.82283504\,j$	$-0.17522867 - 0.82283503\,j$
$-0.32519719 - 0.63610486\,j$	$-0.32519705 - 0.63610485\,j$
$-0.34373267 - 0.67764346\,j$	$-0.34373449 - 0.67764252\,j$
$-0.66286552 - 0.67027520\,j$	$-0.66286552 - 0.67027520\,j$

Table 3.1: Least stable eigenvalues of Orr-Sommerfeld and Squire matrix for $Re = 10000$, $\alpha = 1$ and $\beta = 0$: comparison between literature and spectral derivatives scheme.

Eigenvalues with finite differences	
$N = 140$	$N = 420$
$-0.03517149 - 0.96491989\,j$	$-0.03516776 - 0.96466336\,j$
$-0.03519049 - 0.96493167\,j$	$-0.03518704 - 0.96467496\,j$
$-0.05567417 - 0.27694719\,j$	$-0.05146951 - 0.27714155\,j$
$-0.06321614 - 0.93730086\,j$	$-0.06320315 - 0.93642700\,j$
$-0.06326420 - 0.93733665\,j$	$-0.06325302 - 0.93646228\,j$
$-0.09125560 - 0.91006094\,j$	$-0.09122641 - 0.90821619\,j$
$-0.09133959 - 0.91013498\,j$	$-0.09131589 - 0.90828951\,j$
$-0.11929327 - 0.88319777\,j$	$-0.11923958 - 0.88002784\,j$
$-0.11941743 - 0.88332638\,j$	$-0.11937598 - 0.88015620\,j$
$-0.13068803 - 0.34449294\,j$	$-0.12521618 - 0.34853458\,j$
$-0.14739614 - 0.41177196\,j$	$-0.13928940 - 0.41576417\,j$
$-0.14733285 - 0.85670917\,j$	$-0.14724491 - 0.85185866\,j$
$-0.14749865 - 0.85691061\,j$	$-0.14743374 - 0.85206189\,j$
$-0.17537852 - 0.83059326\,j$	$-0.17524524 - 0.82370521\,j$
$-0.33462740 - 0.67062235\,j$	$-0.32771455 - 0.63364552\,j$
$-0.34800467 - 0.67799967\,j$	$-0.34550988 - 0.67621392\,j$
$-0.66120126 - 0.67332972\,j$	$-0.66279600 - 0.67042974\,j$

Table 3.2: Least stable eigenvalues of Orr-Sommerfeld and Squire matrix for $Re = 10000$, $\alpha = 1$ and $\beta = 0$: comparison between finite differences schemes with different mesh grids.

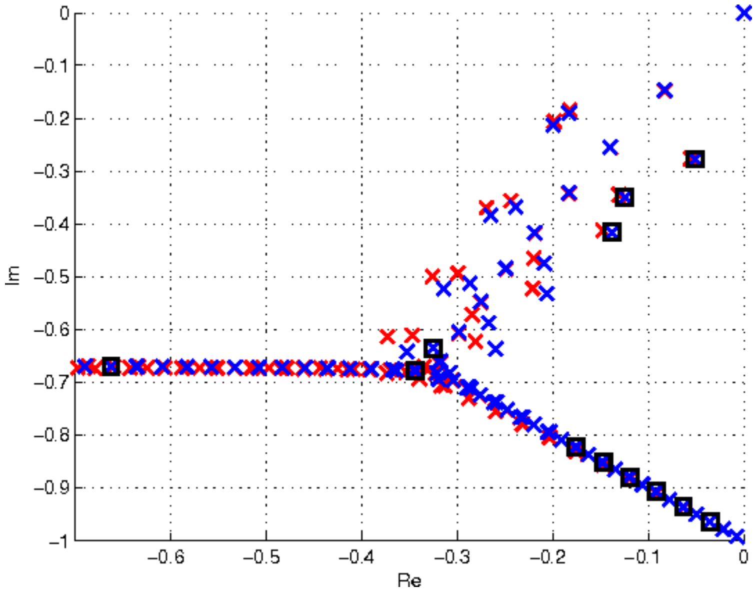

(a) $N = 140$

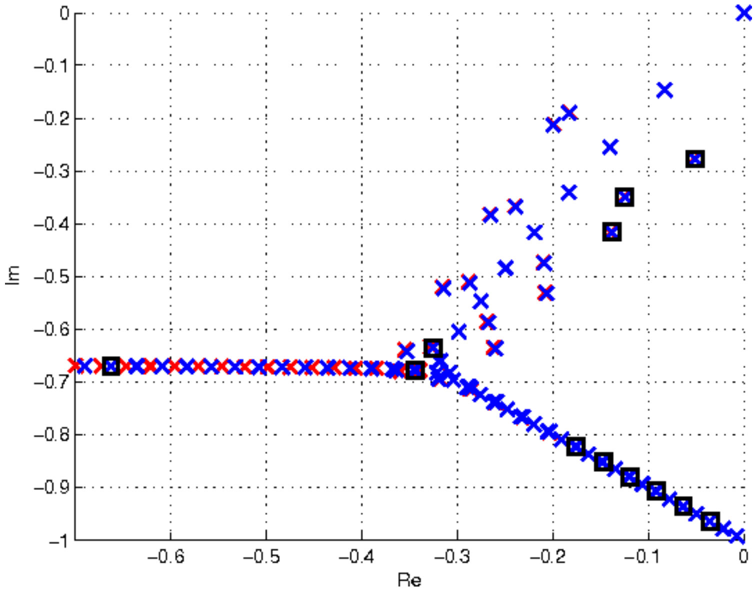

(b) $N = 420$

Figure 3.9: Eigenvalues of Orr-Sommerfeld and Squire matrix for $Re = 10000$, $\alpha = 1$, $\beta = 0$ calculated with finite differences (red crosses) and spectral derivatives (blue crosses), compared to the ones reported in literature (black squares).

Chapter 4

Optimal State Feedback Control

After having developed a linear model for plane channel flow, we are now able to define a proper optimal control law. In the following, we will discuss the solution we have implemented, then a parametric study will be carried out to assess the performances of different control solutions applied to a turbulent flow for a couple of Reynolds numbers that have been widely investigated in literature through DNS, namely $Re = 1500$ and 3500.

4.1 Derivation of an optimal controller

In order to implement an optimal control strategy we need first to recast the Orr-Sommerfeld and Squire model developed in Chapter 3 into state-space formulation. For this purpose, we will consider here and in the following a state-space linear time-invariant (LTI) system defined as

$$\begin{cases} \dot{x} = Ax + Bu + B_n n & (4.1a) \\ y = Cx + D_{yd} d & (4.1b) \end{cases}$$

where $x \in \mathcal{C}^n$ represents the state vector, $u \in \mathcal{C}^m$ is the control vector, $y \in \mathcal{C}^p$ is the measurement vector, n the disturbance acting on input, d the noise affecting measures. Besides, $A \in \mathcal{C}^{n\times n}$ is the state matrix, $B \in \mathcal{C}^{n\times m}$ the input matrix, $C \in \mathcal{C}^{p\times n}$ the measurement matrix and B_n and D_{yd} are the input matrices of disturbances. In order to obtain a state-space formulation, we adopted the strategy proposed in [25]. Hence, since blowing/suction is applied at walls, we define a control variable $\hat{\phi}$ which represents the wall-normal velocities at boundaries: $\hat{\phi} = \begin{bmatrix} \hat{v}_{+1} \\ \hat{v}_{-1} \end{bmatrix}$. This particular kind of forcing is difficult to handle in standard linear control theory unless we introduce a lifting procedure with which the inhomogeneous boundary conditions at walls are represented by volume forcing near the wall in a modified system with homogeneous boundary conditions. Thus, using superposition principle, the solution of the original system $\hat{x}$

is recovered by combining the homogeneous solution $\hat{x}_h$ with a particular solution $\hat{x}_p$:

$$\hat{x} = \hat{x}_h + \hat{x}_p = \begin{cases} \hat{v} = \hat{v}_h + \hat{v}_p \\ \hat{\eta} = \hat{\eta}_h + \hat{\eta}_p \end{cases} \tag{4.2}$$

where particular solution is introduced to relate boundary conditions to volume forcing, as follows:

$$\hat{x}_p = \begin{bmatrix} \hat{v}_p \\ \hat{\eta}_p \end{bmatrix} = \begin{bmatrix} Z_{v_p,\,v_{+1}} & Z_{v_p,\,v_{-1}} \\ Z_{\eta_p,\,v_{+1}} & Z_{\eta_p,\,v_{-1}} \end{bmatrix} \begin{bmatrix} \hat{v}_{+1} \\ \hat{v}_{-1} \end{bmatrix} = Z\hat{\phi} \tag{4.3}$$

Matrix Z can be determined in different ways. The first solution suggests to calculate both block-columns by solving an appropriate two points boundary value problem, e.g. considering upper wall actuation:

$$\begin{cases} L_{OS} Z_{v_p,\,v_{+1}}(y) = 0 \\ L_C Z_{v_p,\,v_{+1}}(y) + L_{SQ} Z_{\eta_p,\,v_{+1}}(y) = 0 \end{cases} \tag{4.4}$$

with boundary conditions

$$\begin{aligned} Z_{v_p,\,v_{+1}}(y = +1) &= 1 \\ Z_{v_p,\,v_{+1}}(y = -1) &= 0 \\ Z'_{v_p,\,v_{+1}}(y = \pm 1) &= 0 \\ Z_{\eta_p,\,v_{+1}}(y = \pm 1) &= 0 \end{aligned} \tag{4.5}$$

An analogous problem must be solved for lower wall actuation.
The second and more straightforward solution is to choose Z in order to satisfy just boundary conditions. This is the approach that has been followed in this work and the functions that have been introduced to assemble matrix Z are

$$\begin{aligned} Z_{v_p,\,v_{+1}} &= \frac{1}{2}\left\{\cos\left[\frac{\pi}{2}(y-1)\right] + 1\right\} \\ Z_{v_p,\,v_{-1}} &= \frac{1}{2}\left\{\cos\left[\frac{\pi}{2}(y+1)\right] + 1\right\} \\ Z_{\eta_p,\,v_{+1}} &= \sin\left[\frac{\pi}{2}(y-1)\right] \\ Z_{\eta_p,\,v_{-1}} &= \sin\left[\frac{\pi}{2}(y+1)\right] \end{aligned} \tag{4.6}$$

After this step, we finally obtain a state-space model for each wavenumber pair (α, β):

$$\dot{\hat{x}}_s = A\hat{x}_s + B\hat{u}_s \tag{4.7}$$

where

$$A = \begin{bmatrix} N & NZ \\ 0 & 0 \end{bmatrix}, \qquad B = \begin{bmatrix} -Z \\ I \end{bmatrix}, \qquad \hat{x}_s = \begin{bmatrix} \hat{x}_h \\ \hat{\phi} \end{bmatrix}, \qquad \hat{u}_s = \frac{\partial \hat{\phi}}{\partial t} \tag{4.8}$$

With this model at hand, we apply a control law based on state feedback, i.e.

$$\hat{u}_s = -\hat{K}_s \hat{x}_s \tag{4.9}$$

where $\hat{K}_s$ is the unknown gain matrix that can be determined as the solution of an optimal control problem. Therefore, we define an objective function combining a state norm and a weight on control effort, i.e.

$$J = \frac{1}{2} \int_0^{\infty} (\hat{x}^T Q \hat{x} + \rho \hat{u}_s^T R \hat{u}_s)\, dt \tag{4.10}$$

where ρ is a penalty introduce to weigh the relative importance of control effort on control performances. However, in this formulation state vector $\hat{x}$ differs from the one we have defined to account for boundary conditions, so it must be modified by considering that $\hat{x} = [I \quad Z]\hat{x}_s$. We get

$$J = \frac{1}{2} \int_0^{\infty} (\hat{x}_s^T \hat{Q}_s \hat{x}_s + \rho \hat{u}_s^T R \hat{u}_s)\, dt \tag{4.11}$$

where

$$\hat{Q}_s = \begin{bmatrix} \hat{Q} & \hat{Q}Z \\ Z^T\hat{Q} & Z^T\hat{Q}Z \end{bmatrix} \tag{4.12}$$

According to optimal feedback control theory, the control feedback minimizing functional J in (4.11) is defined as

$$\hat{K}_s = \rho R^{-1} B^T P \tag{4.13}$$

where P is the solution of the following Riccati equation:

$$A^T P + PA + \hat{Q}_s - \rho P B R^{-1} B^T P = 0 \tag{4.14}$$

The controller arising from these procedure is called linear quadratic regulator (LQR). Nevertheless, the feedback rule we have just defined is for the feedback of the homogeneous part only, thus it must be modified accordingly before being applied to channel flow. For this purpose, let us consider the decomposition

$$\hat{u}_s = \begin{bmatrix} \hat{K}_{s,\,+1,\,\hat{v}_h} & \hat{K}_{s,\,+1,\,\hat{\eta}_h} & \hat{K}_{s,\,+1,\,\hat{v}_{+1}} & \hat{K}_{s,\,+1,\,\hat{v}_{-1}} \\ \hat{K}_{s,\,-1,\,\hat{v}_h} & \hat{K}_{s,\,-1,\,\hat{\eta}_h} & \hat{K}_{s,\,-1,\,\hat{v}_{+1}} & \hat{K}_{s,\,-1,\,\hat{v}_{-1}} \end{bmatrix} \begin{bmatrix} \hat{v}_h \\ \hat{\eta}_h \\ \hat{v}_{+1} \\ \hat{v}_{-1} \end{bmatrix} \tag{4.15}$$

hence, after some trivial manipulations, we obtain

$$\begin{bmatrix} \dot{\hat{v}}_{+1} \\ \dot{\hat{v}}_{-1} \end{bmatrix} = \begin{bmatrix} \hat{K}_{+1,\,\hat{v}} & \hat{K}_{+1,\,\hat{\eta}} \\ \hat{K}_{-1,\,\hat{v}} & \hat{K}_{-1,\,\hat{\eta}} \end{bmatrix} \hat{x} \tag{4.16}$$

where

$$\hat{K}_{\pm 1,\,\hat{v}_{+1}} = \hat{K}_{s,\,\pm 1,\,\hat{v}_{+1}} - \hat{K}_{s,\,\pm 1,\,\hat{v}_h} Z_{\hat{v}_p\,\hat{v}_{+1}} - \hat{K}_{s,\,\pm 1,\,\hat{\eta}_h} Z_{\hat{\eta}_p\,\hat{v}_{+1}} \tag{4.17}$$

$$\hat{K}_{\pm 1,\,\hat{v}_{-1}} = \hat{K}_{s,\,\pm 1,\,\hat{v}_{-1}} - \hat{K}_{s,\,\pm 1,\,\hat{v}_h} Z_{\hat{v}_p\,\hat{v}_{-1}} - \hat{K}_{s,\,\pm 1,\,\hat{\eta}_h} Z_{\hat{\eta}_p\,\hat{v}_{-1}} \tag{4.18}$$

and

$$\hat{K}_{\pm 1,\,\hat{v}} = \begin{bmatrix} \hat{K}_{\pm 1,\,\hat{v}_{-1}} & \hat{K}_{\pm 1,\,\hat{v}_h} & \hat{K}_{\pm 1,\,\hat{v}_{+1}} \end{bmatrix} \tag{4.19}$$

$$\hat{K}_{\pm 1,\,\hat{v}} = \begin{bmatrix} 0 & \hat{K}_{\pm 1,\,\hat{\eta}_h} & 0 \end{bmatrix} \tag{4.20}$$

Now, since with this definition control gains depend on the spatial discretization in y direction, it is necessary to scale the control gains to a grid-independent weighting function at each wavenumber pair $(\alpha,\, \beta)$. After this straightforward transformation, weights $\hat{K}$ can be incorporated into DNS code by scaling the control gains by the grid stretching function used in the simulation code, in our case the hyperbolic tangent function defined in (3.15). Feedback rules are then computed for an array of wavenumber pairs and then inverse Fourier-transformed to physical space, where control law appears in the form of a convolution integral, as follows:

$$\begin{aligned} \dot{v}(x,\, y = \pm 1,\, z,\, t) = \int_0^{L_z} \int_{-1}^{+1} \int_0^{L_x} & \left[K_{\pm 1,\, v}(x - \bar{x},\, \bar{y},\, z - \bar{z})\, v(\bar{x},\, \bar{y},\, \bar{z},\, t) + \right. \\ & \left. + K_{\pm 1,\, \eta}(x - \bar{x},\, \bar{y},\, z - \bar{z})\, \eta(\bar{x},\, \bar{y},\, \bar{z},\, t) \right] d\bar{x}\, d\bar{y}\, d\bar{z} \end{aligned} \tag{4.21}$$

where $K_{\pm 1,\, v}$ and $K_{\pm 1,\, \eta}$ appear feedback convolution kernels in physical space.

4.2 Choice of reference velocity profile

Among the possible reference velocity profiles $U(y)$ that can be used to design full state controller, it is particularly useful to choose the analytical solution of Poiseuille laminar flow, which is a rare case in which Navier-Stokes equations admit closed-form solution. In facts, Poiseuille channel flow is based on the assumption of parallel stationary flow, that leads to the following simplified two-dimensional Navier-Stokes equations:

$$\left\{ \begin{aligned} & \frac{\partial U}{\partial x} + \frac{\partial V}{\partial y} = 0 && \text{(4.22a)} \\ & U \frac{\partial U}{\partial x} + V \frac{\partial U}{\partial y} = -\frac{\partial P}{\partial x} + \frac{1}{Re} \Delta U && \text{(4.22b)} \\ & U \frac{\partial V}{\partial x} + V \frac{\partial V}{\partial y} = -\frac{\partial P}{\partial y} + \frac{1}{Re} \Delta V && \text{(4.22c)} \end{aligned} \right.$$

Now, we search for a solution of the type $\mathbf{U} = (U(x, y),\, 0,\, 0)$. This assumption reduces the continuity equation to the condition $\frac{\partial u}{\partial y} = 0$. So, all the convective terms on the

LHS of the equations are equal to zero, determining

$$\begin{cases} \dfrac{1}{Re}\dfrac{d^2U}{dy^2} - \dfrac{\partial P}{\partial x} = 0 & \text{(4.23a)} \\ \dfrac{\partial P}{\partial y} = 0 & \text{(4.23b)} \end{cases}$$

This leads to a further simplification:

$$\frac{1}{Re}\frac{d^2U}{dy^2} - \frac{dP}{dx} = 0 \tag{4.24}$$

Thus, by imposing no-slip boundary condition at walls and nondimensionalizing the solution with respect to bulk velocity, we get

$$U(y) = \frac{3}{2}(1 - y^2) \tag{4.25}$$

Another meaningful choice for the reference velocity profile could be the mean streamwise velocity profile $\bar{U}(y)$ of the turbulent channel flow, which can be recovered after averaging the streamwise velocity obtained through a DNS performed at the given Reynolds number, i.e.

$$\bar{U}(y) = \lim_{T\to\infty} \frac{1}{L_x L_z}\frac{1}{T}\int_0^{L_x}\int_0^{L_z}\int_0^{T} U(x,\, y,\, z,\, t)\, dt\, dz\, dx \tag{4.26}$$

4.3 Objective function design

The choice of a proper weight on state vector in optimal control formulation is for our scope a very delicate task, since it is not possible to directly target drag through the objective function, in that standard LQR control allows only quadratic norms of the state. For this reason, it is necessary to find a proper state measure whose minimization will reduce turbulent drag. In [5] many control laws have been investigated in a model predictive control framework, in order to state the effectiveness of different cost functions. An interesting conclusion that came out is that turbulent kinetic energy is a good candidate for achieving drag reduction through zero-net-mass-flux blowing/suction actuation at walls in a full-information control framework. Furthermore, in [25] energy norm has been successfully introduced to delay transition to turbulence at a critical regime. Another quadratic performance measure investigated in this work is the rate of dissipation which has been firstly introduced in [52] applied to a measure-based Wiener-Hopf control framework, basing on the physical intuition that in statistically stationary conditions the average skin fraction drag in a turbulent channel flow equals the average rate of dissipation of turbulent kinetic energy. Then, a third measure has been tested to achieve drag reduction, i.e. enstrophy norm, that is a quantity directly related to the kinetic energy in the flow and which corresponds to dissipation effects in the fluid. Finally, measurements available at walls have been used in order to obtain a quadratic norm of the state. These last control laws have been applied in a flow control setting for the first time in the present work.

Before going into details, we will show how to calculate the integral over the domain $y \in [-1, 1]$ appearing in state norms, i.e. by defining proper methods of numerical quadrature depending on the discretization techniques adopted. Thus, when finite differences schemes have been introduced to discretize wall-normal derivative operators, we chose a Lagrange quadrature scheme, whose general definition is

$$\int_{-1}^{1} f(y)\,dy = \sum_{j=0}^{N} \alpha_j f(y_j) \tag{4.27}$$

where $f(y)$ is the function we want to integrate and α_j are the integration weights. The choice of such integration weights leads to different quadrature schemes. In the present work we have decided to adopt the trapezoidal rule, which defines the weights $\{\alpha_j\}_0^N$ as follows:

$$\alpha_j = \begin{cases} \dfrac{1}{2} & \text{for} \quad j = 0,\, N \\ 1 & \text{otherwise} \end{cases} \tag{4.28}$$

As for spectral derivatives, instead, we have implemented the strategy suggested in [28] and applied for the first time in [24]. We start by approximating the integrand function $f(y)$ with a Chebyshev expansion

$$f(y) = \sum_{j=0}^{N} a_j T_j(y) \tag{4.29}$$

where $T_j(y)$ is the Chebyshev polynomial previously defined in Section 3.3.2, while coefficients a_i are defined as

$$a_i = \frac{c_i}{N} \sum_{j=0}^{N} b_j f(y_j) T_j(y_j) \tag{4.30}$$

where

$$b_j = \begin{cases} \dfrac{1}{2} & \text{for} \quad j = 0,\, N \\ 1 & \text{otherwise} \end{cases} \quad \text{and} \quad c_i = \begin{cases} 1 & \text{for} \quad i = 0,\, N \\ 2 & \text{otherwise} \end{cases} \tag{4.31}$$

Then, by combining Equations (4.29) and (4.30), we get

$$f(y) = \sum_{i=0}^{N} c_i T_i(y) \sum_{j=0}^{N} \frac{b_j}{N} f(y_j) T_i(y_j) \tag{4.32}$$

Substitution of Equation (4.32) into (4.27) leads to

$$\int_{-1}^{1} f(y)\,dy = \frac{1}{N} \sum_{j=0}^{N} b_j f(y_j) \sum_{i=0}^{N} c_i T_i(y_j) \int_{-1}^{1} T_i(y)\,dy \tag{4.33}$$

Finally, noticing that

$$\int_{-1}^{1} T_i(y)\,dy = \begin{cases} 0 & i \text{ odd} \\ \dfrac{2}{1-i^2} & i \text{ even} \end{cases} \tag{4.34}$$

yields

$$\alpha_j = \frac{b_j}{N}\left[2 + \sum_{i=1}^{N} c_i \frac{1+(-1)^i}{1-i^2}\cos\left(\frac{ij\pi}{N}\right)\right] \tag{4.35}$$

In the following, we will provide an analytical derivation of the proposed state norms.

4.3.1 Energy norm

Turbulent kinetic energy norm is defined in physical domain as follows:

$$E = \frac{1}{2V}\int_V (u^2 + v^2 + w^2)\,dV \tag{4.36}$$

where V is the volume of the computation domain. After Fourier-transforming by reminding relations (3.9), we apply Parseval theorem to obtain:

$$\begin{aligned} E(\alpha,\,\beta) &= \frac{1}{8}\int_{-1}^{1}(|\hat u|^2 + |\hat v|^2 + |\hat w|^2)\,dy = \\ &= \frac{1}{8k^4}\int_{-1}^{1}(\alpha^2\hat v^T D_1^T D_1 \hat v + \beta^2 \hat\eta^T\hat\eta \cancel{-\alpha\beta\hat v^T D_1^T\hat\eta} \cancel{-\alpha\beta\hat\eta^T D_1\hat v} + \\ &\quad + k^4\hat v^T\hat v + \alpha^2\hat\eta^T\hat\eta + \beta^2\hat v^T D_1^T D_1\hat v \cancel{+\alpha\beta\hat v^T D_1^T\hat\eta} \cancel{+\alpha\beta\hat\eta^T D_1\hat v})\,dy = \\ &= \frac{1}{8k^2}\int_{-1}^{1}[\hat v^T(k^2 I + D_1^T D_1)\hat v + \hat\eta^T\hat\eta],dy \end{aligned} \tag{4.37}$$

So, we can define energy as a quadratic function of the state vector x:

$$E(\alpha,\,\beta) = x^T Q_E(\alpha,\,\beta)x = \|x\|_E \tag{4.38}$$

4.3.2 Dissipation norm

If we consider stationary conditions, dissipation rate of a turbulent flow is defined as

$$D = \frac{1}{Re}\int_V \frac{\partial u_i}{\partial u_j}\frac{\partial u_i}{\partial u_j}\,dV \tag{4.39}$$

After averaging and Fourier-transforming, we obtain

$$\begin{aligned} D(\alpha,\,\beta) = \frac{1}{Re}\frac{1}{2k^2}\int_{-1}^{1}&[\hat v^T(D_2^T D_2 + 2k^2 D_1^T D_1 + k^4)\hat v + \\ &+ \hat\eta^T(k^2 + D_1^T D_1)\hat\eta]\,dy \end{aligned} \tag{4.40}$$

So, we can define dissipation as a quadratic function of the state vector x, as done previously:

$$D(\alpha,\, \beta) = x^T Q_D(\alpha,\, \beta) x = \|x\|_D \tag{4.41}$$

4.3.3 Enstrophy norm

Enstrophy is defined as the integral of the square of the total vorticity:

$$\Xi = \frac{1}{2V} \int_V (\eta_x^2 + \eta_y^2 + \eta_z^2)\, dV \tag{4.42}$$

where

$$\begin{aligned}
\eta_x &= \frac{\partial w}{\partial y} - \frac{\partial v}{\partial z} \Rightarrow \hat{\eta}_x = \frac{1}{k^2}(j\alpha D_1 \hat{\eta} + j\beta D_2 \hat{v} - j\beta k^2 \hat{v}) \\
\eta_y &= \frac{\partial u}{\partial z} - \frac{\partial w}{\partial x} \Rightarrow \hat{\eta}_y = \hat{\eta} \\
\eta_z &= \frac{\partial v}{\partial x} - \frac{\partial u}{\partial y} \Rightarrow \hat{\eta}_z = \frac{1}{k^2}(j\alpha k^2 \hat{v} - j\alpha D_2 \hat{v} + j\beta D_1 \hat{\eta})
\end{aligned} \tag{4.43}$$

Then, through substitution in Equation (4.42), after Fourier-transforming, we obtain

$$\begin{aligned}
\Xi(\alpha,\, \beta) &= \frac{1}{8} \int_{-1}^{1} (|\hat{\eta}_x|^2 + |\hat{\eta}_y|^2 + |\hat{\eta}_z|^2)\, dy = \\
&= \frac{1}{8k^4} \int_{-1}^{1} (\alpha^2 \hat{\eta}^T D^T D \hat{\eta} + \beta^2 \hat{v} D_2^T D_2 \hat{v} + \beta^2 k^4 \hat{v}^T \hat{v} + k^4 \hat{\eta}^T \hat{\eta} + \alpha^2 k^4 \hat{v}^T \hat{v} \\
&\quad + \alpha^2 \hat{v}^T D_2^T D_2 \hat{v} + \beta^2 \hat{\eta}^T D^T D \hat{\eta} \cancel{+ 2\alpha\beta \hat{\eta}^T D^T D_2 \hat{v}} \cancel{- 2\alpha\beta k^2 \hat{\eta}^T D^T \hat{v}} + \\
&\quad - 2\beta^2 k^2 \hat{v}^T D_2 \hat{v} - 2\alpha^2 k^2 \hat{v}^T D_2 \hat{v} + \cancel{-2\alpha\beta \hat{\eta}^T D^T D_2 \hat{v}} \cancel{+ 2\alpha\beta k^2 \hat{\eta}^T D^T \hat{v}})\, dy = \\
&= \frac{1}{8k^2} \int_{-1}^{1} [\hat{\eta}^T (D^T D + k^2 I) \hat{\eta} + \hat{v}^T (D_2^T D_2 - 2k^2 D_2 + k^4 I) \hat{v}]\, dy
\end{aligned} \tag{4.44}$$

Again, state norm is represented as

$$\Xi(\alpha,\, \beta) = x^T Q_\Xi(\alpha,\, \beta) x = \|x\|_\Xi \tag{4.45}$$

4.3.4 Wall-measurement norm

As previously mentioned, matrix C is used to relate output measurements to the state vector. Since only wall information is available, the measures we can dispose of are spanwise and streamwise wall shear stresses, namely τ_{x_w} and τ_{z_w}, and wall pressure

p_w, for which the following relations hold:

$$\tau_{x_w} = \frac{1}{Re} \left. \frac{\partial u}{\partial y} \right|_{y \pm 1} \tag{4.46}$$

$$\tau_{z_w} = \frac{1}{Re} \left. \frac{\partial w}{\partial y} \right|_{y \pm 1} \tag{4.47}$$

$$p_w = p|_{y \pm 1} \tag{4.48}$$

Since the control scheme we have derived is applied to a state-space system in Fourier domain, it is necessary to recast these relations in wavenumber space. Hence, wall shear stresses in Fourier space are determined as

$$\hat{\tau}_{x_w} = \frac{1}{Re} D_1 \left. \frac{\partial \hat{u}}{\partial y} \right|_{y=\pm 1} = \frac{j}{k^2 Re} \begin{bmatrix} \alpha D_{2_w} & -\beta D_{1_w} \end{bmatrix} \left. \begin{bmatrix} \hat{v} \\ \hat{\eta} \end{bmatrix} \right|_{y=\pm 1} \tag{4.49}$$

$$\hat{\tau}_{z_w} = \frac{1}{Re} D_1 \left. \frac{\partial \hat{w}}{\partial y} \right|_{y=\pm 1} = \frac{j}{k^2 Re} \begin{bmatrix} \beta D_{2_w} & \alpha D_{1_w} \end{bmatrix} \left. \begin{bmatrix} \hat{v} \\ \hat{\eta} \end{bmatrix} \right|_{y=\pm 1} \tag{4.50}$$

Wall pressure is recovered by taking the sum of Equation (3.3b), derived with respect to x and Equation (3.3d), derived with respect to z, and by evaluating it at walls in steady-state conditions. We get

$$\left. \frac{\partial^2 p}{\partial x^2} \right|_{y \pm 1} + \left. \frac{\partial^2 p}{\partial z^2} \right|_{y=\pm 1} = - \frac{1}{Re} \left. \frac{\partial \Delta v}{\partial y} \right|_{y=\pm 1} \tag{4.51}$$

Then, after Fourier-transforming

$$\hat{p}_w = \frac{1}{k^2 Re} D_3 \hat{v}|_{y=\pm 1} \tag{4.52}$$

we find the associated output-to-state relation

$$\hat{p}_w = \frac{1}{k^2 Re} \begin{bmatrix} D_{3_w} & 0 \end{bmatrix} \left. \begin{bmatrix} \hat{v} \\ \hat{\eta} \end{bmatrix} \right|_{y=\pm 1} \tag{4.53}$$

Nevertheless, the lifting technique we have introduced to apply LQR control has led to a modified definition of state vector. For this reason, now we have to recast these relations in a coherent form. We start by partitioning state vector into homogeneous and inhomogeneous parts:

$$\begin{bmatrix} \hat{v} \\ \hat{\eta} \end{bmatrix} = \begin{bmatrix} \hat{\phi}_{-1} \\ \hat{v}_h + \hat{v}_p \\ \hat{\phi}_{+1} \\ 0 \\ \hat{\eta}_h + \hat{\eta}_p \\ 0 \end{bmatrix} = \begin{bmatrix} \hat{\phi}_{-1} \\ \hat{v}_h + Z_{v_p,\, v_{+1}} \hat{\phi}_{+1} + Z_{v_p,\, v_{-1}} \hat{\phi}_{-1} \\ \hat{\phi}_{+1} \\ 0 \\ \hat{\eta}_h + Z_{\eta_p,\, v_{+1}} \hat{\phi}_{+1} + Z_{\eta_p,\, v_{-1}} \hat{\phi}_{-1} \\ 0 \end{bmatrix} \tag{4.54}$$

Hence, if now we consider for example the streamwise wall shear stress at lower wall and we adopt finite differences schemes in order to discretize uncentered derivatives, with some manipulations we get

$$\begin{aligned}\hat{\tau}_{x_w\,-1} &= \frac{j}{k^2 Re}\begin{bmatrix}\alpha D^{0}_{2_w} & \alpha D^{1:4}_{2_w} & 0 & \dots & 0 & 0\\ -\beta D^{0}_{1_w} & \beta D^{1:4}_{1_w} & 0 & \dots & 0 & 0\end{bmatrix}\begin{bmatrix}\hat{v}\\ \hat{\eta}\end{bmatrix} =\\ &= \frac{j}{k^2 Re}\{\begin{bmatrix}\alpha D^{1:4}_{2_w} & 0 & \dots & 0 & -\beta D^{1:4}_{1_w} & 0 & \dots & 0\end{bmatrix}\begin{bmatrix}\hat{v}_h\\ \hat{\eta}_h\end{bmatrix} +\\ &+ \begin{bmatrix}\alpha D^{1:4}_{2_w} & 0 & \dots & 0 & \beta D^{1:4}_{1_w} & 0 & \dots & 0\end{bmatrix} Z + \begin{bmatrix}0 & \alpha D^{0}_{2_w}\end{bmatrix}\hat{\phi}\}\end{aligned} \tag{4.55}$$

Similarly, for the upper wall we find

$$\begin{aligned}\hat{\tau}_{x_w\,+1} &= \frac{j}{k^2 Re}\begin{bmatrix}0 & 0 & \dots & 0 & \alpha D^{n-4:n-1}_{2_w} & \alpha D^{n}_{2_w}\\ 0 & 0 & \dots & 0 & -\beta D^{n-4:n-1}_{1_w} & -\beta D^{n}_{1_w}\end{bmatrix}\begin{bmatrix}\hat{v}\\ \hat{\eta}\end{bmatrix} =\\ &= \frac{j}{k^2 Re}\{\begin{bmatrix}0 & \dots & 0 & \alpha D^{n-4:n-1}_{2_w} & 0 & \dots & 0 & -\beta D^{n-4:n-1}_{1_w}\end{bmatrix}\begin{bmatrix}\hat{v}_h\\ \hat{\eta}_h\end{bmatrix} +\\ &+ \begin{bmatrix}0 & \dots & 0 & \alpha D^{n-4:n-1}_{2_w} & 0 & \dots & 0 & -\beta D^{n-4:n-1}_{1_w}\end{bmatrix} Z + \begin{bmatrix}\alpha D^{n}_{2_w} & 0\end{bmatrix}\hat{\phi}\}\end{aligned} \tag{4.56}$$

For spanwise wall shear stresses and pressure measurements, their output-to-state relations can be found in a similar manner. Matrix C is then obtained by assembling all these relations, as follows:

$$y = \begin{bmatrix}\tau_{x_w\,\pm 1}\\ \tau_{x_w\,\pm 1}\\ p_{w\,\pm 1}\end{bmatrix} = \begin{bmatrix}C_{\tau_{x_w\,\pm 1}}\\ C_{\tau_{x_w\,\pm 1}}\\ C_{p_w\,\pm 1}\end{bmatrix}\begin{bmatrix}\hat{v}_h\\ \hat{\eta}_h\\ \hat{\phi}\end{bmatrix} = C\hat{x}_s \tag{4.57}$$

A quadratic norm of the state is then obtained by considering

$$y^T y = x^T C^T C x = x^T Q_C x = \|x\|_C \tag{4.58}$$

4.4 Solution of Riccati equation

Riccati equation arising from optimal control formulation is a nonlinear continuous algebraic equation (CARE) for which many algorithms have been proposed in the last decades in order to provide a numerical solution. All of them can be grouped into two categories, the first one considering those algorithms which find a solution through matrix factorization, the second involving numerical procedures which define an iterative method converging to the unique solution. Usually, in standard control problems factorization methods are well suited since they have a deterministic computational time. On the other hand, if we are dealing with extremely ill-conditioned matrices, then factorization techniques can lead to inaccurate solutions, while iterative methods, given an initial stabilizing solution, are able to converge to actual solution with the desired degree of precision.

Since in the present work a set of Riccati equations needed to be solved during kernel generation phase and for smaller penalties ρ matrices became very ill-conditioned, an iterative solver has been implemented, based on Newton-Kleinman method. In order to initialize such solver, we have used the solution of a factorizing technique based on Schur-Hamilton method. In the following, the two methods adopted in tandem will be briefly discussed.

4.4.1 Schur-Hamilton method

Starting by considering CARE

$$A^T P + PA + Q - PBR^{-1}B^T P = 0 \tag{4.59}$$

the key idea is to build the associated Hamiltonian matrix

$$H = \begin{bmatrix} A & -S \\ -Q & -A^T \end{bmatrix} \tag{4.60}$$

where $S = BR^{-1}B^T$. Then, it can be proved that a matrix P is a solution of the CARE if and only if the columns of $\left[\begin{smallmatrix} I \\ P \end{smallmatrix}\right]$ span an n-dimensional invariant subspace of the Hamiltonian matrix H in (4.60). To prove that, we introduce the following matrix J:

$$J = \begin{bmatrix} 0 & I \\ -I & 0 \end{bmatrix} \tag{4.61}$$

then, we assume that a $n \times n$ matrix L exists such that

$$H \begin{bmatrix} I \\ P \end{bmatrix} = \begin{bmatrix} I \\ P \end{bmatrix} L \tag{4.62}$$

Multiplying both sides of (4.62) by the inverse of J, we find

$$J^{-1} H \begin{bmatrix} I \\ P \end{bmatrix} = J^{-1} \begin{bmatrix} I \\ P \end{bmatrix} L \tag{4.63}$$

Hence, we can get further simplification and write

$$\begin{bmatrix} Q & A^T \\ A & -S \end{bmatrix} \begin{bmatrix} I \\ P \end{bmatrix} = \begin{bmatrix} -P \\ I \end{bmatrix} L \tag{4.64}$$

Finally, by multiplying both sides of (4.64) by $\left[\begin{smallmatrix} I & P \end{smallmatrix}\right]$, we get

$$PA + A^T P + Q - PSP = 0 \tag{4.65}$$

showing that P satisfies the CARE. To prove the converse, we note that if P is a solution of the CARE, then

$$H \begin{bmatrix} I \\ P \end{bmatrix} = \begin{bmatrix} A - SP \\ -Q - A^T P \end{bmatrix} = \begin{bmatrix} A - SP \\ P(A - SP) \end{bmatrix} = \begin{bmatrix} I \\ P \end{bmatrix} (A - SP) \tag{4.66}$$

that is, the columns of $\left[\begin{smallmatrix} I \\ P \end{smallmatrix}\right]$ span an invariant subspace of H. As a corollary, it can be straightforwardly proved that if the columns of $\left[\begin{smallmatrix} P_1 \\ P_2 \end{smallmatrix}\right]$ span an n-dimensional invariant subspace of the Hamiltonian matrix H and P_1 is invertible, then $P_2 P_1^{-1}$ is a solution of the CARE. With this in mind, to solve the CARE starting from Hamiltonian matrix H, we need first to transform H into real Schur form (RSF) by using a QR factorization algorithm, as described in [40]. Now, if $U^T H U$ is an ordered real Schur matrix obtained through transformation matrix U, then we have

$$U^T H U = \begin{bmatrix} T_{11} & T_{12} \\ 0 & T_{22} \end{bmatrix} \tag{4.67}$$

where the eigenvalues of H with negative real parts have been stacked in T_{11} and those with positive real parts are stacked in T_{22}. Then, if we conformably partition U in the same way

$$U = \begin{bmatrix} U_{11} & U_{12} \\ U_{21} & U_{22} \end{bmatrix} \tag{4.68}$$

after substitution of (4.68) into Equation (4.67), we get

$$H \begin{bmatrix} U_{11} \\ U_{21} \end{bmatrix} = \begin{bmatrix} U_{11} \\ U_{21} \end{bmatrix} T_{11} \tag{4.69}$$

Hence, the previously mentioned corollary asserts that matrix $P = U_{21} U_{11}^{-1}$ is the unique stabilizing solution of the CARE we were searching for.

4.4.2 Newton-Kleinman method

This algorithm considers an initial stabilizing solution P_0 for Riccati equation (4.59). Then, since

$$P = P_0 + \Delta P \qquad \text{with} \qquad \Delta P = P - X_0 \tag{4.70}$$

we can substitute this expression into (4.59) and find

$$Q + PA + A^T P - P_0 S P_0 - \Delta P S \Delta P - P_0 S \Delta P - \Delta P S P_0 = 0 \tag{4.71}$$

After simplification, we can write

$$(A - SP_0)^T P + P(A - SP_0) = -Q - P_0 S P_0 + \Delta P S \Delta P \tag{4.72}$$

where we can neglect the second-order term $\Delta PS\Delta P$ in the RHS, since we are assuming ΔP is small. Thus, we obtain the following Lyapunov equation for the next approximation P_1:

$$(A - SP_0)^T P_1 + P_1(A - SP_0) = -Q - P_0 S P_0 \tag{4.73}$$

The strategy adopted till now may be considered a sort of Newton's method, even if updating rule is not cast in the canonical form. So, let us define the following quantity:

$$R_C(P) = PA + A^T P - PSP + Q \tag{4.74}$$

Then, we compute the first derivative of $R_C(P)$, for which it is necessary to adopt the definition of derivative generalized to Banach space, i.e. Fréchet derivative, as follows:

$$R'_P(Z) = (A - SP)^T Z + Z(A - SP) \tag{4.75}$$

thus, defining $\Delta_i = P_{i+1} - P_i$, Newton's method for $R_C(P) = 0$ is

$$R'_{P_i}(\Delta_i) + R_C(P_i) = 0 \tag{4.76}$$

which is a Lyapunov equation. Hence, solution at step $i+1$ is determined as $P_{i+1} = P_i + \Delta_i$. So said, we can summarize all the steps in the following algorithm:

1. Choose an initial stabilizing solution P_0
2. Compute $R_C(P_i) = A^T P_i + P_i A + Q - P_i S P_i$
3. Solve the Lyapunov equation for Δ_i:

$$(A - SP_i)^T \Delta_i + \Delta_i(A - SP_i) + R_C(P_i) = 0 \tag{4.77}$$

4. Compute $P_{i+1} = P_i + \Delta_i$

This algorithm ends when a predefined number of maximum iterations is reached or when a fixed tolerance is achieved, i.e.

$$\frac{\|P_{i+1} - P_i\|_F}{\|P_i\|_F} \leq \epsilon \tag{4.78}$$

where $\|.\|_F$ denotes Frobenius matrix norm, defined as

$$\|P_i\|_F = \sqrt{Tr\{P_i^T P_i\}} \tag{4.79}$$

Unfortunately, another issue is still pending, since if an ill-conditioned matrix leads to inaccurate solution by adopting Schur-Hamilton method, then we will encounter numerical difficulties in solving Lyapunov equation (4.77) inside Newton-Kleinman method using standard factorization techniques. Then, inaccurate solution of Lyapunov equation will lead to slower rate of convergence, thus deteriorating performances. Therefore, the same approach used for Riccati equation has been followed to solve Lyapunov equation, i.e. a factorization algorithm based on Schur method has been implemented in order to find an initial stabilizing solution for an iterative Lyapunov solver, based on Smith method. What follows is a brief description of the techniques adopted in the present work.

4.5 Solution of Lyapunov equation

4.5.1 Schur method

This method is actually the most widely used and computationally effective approach. It was proposed for the first time in [2] and it starts by considering the standard algebraic Lyapunov equation:

$$XA + A^T X = C \tag{4.80}$$

Now, we take the RSF of A^T, namely $R = U^T A^T U$ of matrix A^T, which can be obtained through QR factorization, as previously mentioned. After this transformation, Lyapunov equation (4.80) is reduced to

$$YR^T + RY = \widehat{C} \tag{4.81}$$

where $Y = U^T XU$ and $\widehat{C} = U^T CU$. Now let

$$Y = [y_1,\, \dots,\, y_n], \qquad \widehat{C} = [\hat{c}_1,\, \dots,\, \hat{c}_n], \qquad R = [r_{ij}] \tag{4.82}$$

and assume that columns y_{i+1} through y_n have been computed and consider the following two cases:

- *Case 1:* $r_{k,k-1} = 0$. Then, y_k is determined by solving the quasi-triangular system:

$$(R + r_{kk} I) y_k = \hat{c}_k - \sum_{j=k+1}^{n} r_{kj} y_j \tag{4.83}$$

- *Case 2:* $r_{k,\,k-1} \neq 0$ for some k. This indicates that there is a *Schur bump* on the diagonal. This enables to compute y_{i-1} and y_i simultaneously, by solving the following linear system:

$$\begin{aligned} R[y_{i-1},\, y_i] + [y_{i-1},\, y_i] \begin{bmatrix} r_{i-1,\,i-1} & r_{i,\,i-1} \\ r_{i-1,\,i} & r_{ii} \end{bmatrix} &= \\ = [\hat{c}_{i-1},\, \hat{c}_i] - \sum_{j=i+1}^{n} [r_{i-1,\,j},\, r_{ij} y_j] &= [d_{k-1},\, d_k] \end{aligned} \tag{4.84}$$

This procedure is repeated until all the columns of Y have been computed.

4.5.2 Smith method

This technique has been firstly introduced in [69] and has received a lot of attention in the following decades in order to provide this method with faster convergence. The key idea consists of rewriting Lyapunov equation (4.80) in the following form:

$$(pI - A^T)X(pI - A) - (pI + A^T)X(pI + A) = -2pC \tag{4.85}$$

where p is a positive parameter. Premultiplying both sides by $(pI - A^T)^{-1}$ and postmultiplying by $(pI - A)^{-1}$, we get the following Stein equation:

$$X - S^T XS = T \tag{4.86}$$

where $S = (pI + A)(pI - A)^{-1}$ and $T = -2p(pI - A^T)^{-1}C(pI - A)^{-1}$. Thus, starting from an initial condition T_0, the solution at each step $i+1$ is iteratively determined as

$$X_{i+1} = T + S^T X_i S \tag{4.87}$$

For the sake of completeness we have to mention that a faster converging solution has been introduced by Penzl in [58]. It exploits the alternate direction implicit (ADI) method, which defines the solution X_i at each step, through two separate substeps, as follows:

$$(A^T + p_i I)X_{i-1/2} = C - X_{i-1}(A - p_i I) \tag{4.88}$$

$$(A^T + p_i I)X_i = C - X_{i-1/2}(A - p_i I) \tag{4.89}$$

It can be proved that Smith's algorithm is a particular case of ADI method, where parameters p_i assume a single constant value. The choice of these parameters is of great importance, since the rate of convergence has been proved to be strongly affected. In particular, if we decide to choose n parameters p_i, the optimal choice is given by the solution of the following *minimax* problem:

$$\{p_1, \ldots, p_n\} = \arg\min \max_{\lambda_i \in \sigma(A)} \left| \prod_{i=1}^{n} \frac{p_i - \lambda}{p_i + \lambda} \right| \tag{4.90}$$

where $\sigma(A)$ is the spectrum of matrix A. Unfortunately, no closed form solution exists for this problem, so suboptimal techniques must be developed, based on Ritz approximation of matrix spectrum, as shown in [15].

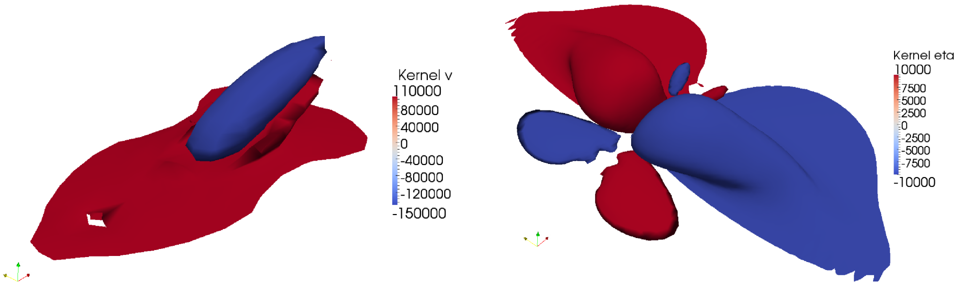

(a) *Kernel for wall-normal velocity* v (b) *Kernel for wall-normal vorticity* η

Figure 4.1: Localized controller gains relating the state x to the control forcing u at walls: visualized are positive (red) and negative (blue) isosurfaces at 6% of the peak value. Kernels were computed at $Re = 1500$ by using *energy norm* and $\rho = 10^{-4}$ in the cost function.

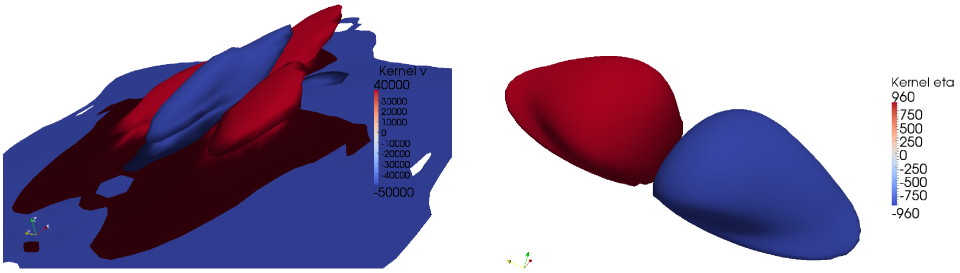

(a) *Kernel for wall-normal velocity* v (b) *Kernel for wall-normal vorticity* η

Figure 4.2: Localized controller gains relating the state x to the control forcing u at walls: visualized are positive (red) and negative (blue) isosurfaces at 6% of the peak value. Kernels were computed at $Re = 1500$ by using *dissipation norm* and $\rho = 10^{-4}$ in the cost function.

4.6 Parametric study on the effectiveness of LQR control

In order to assess the performances of the control laws we have developed, a set of kernels has been generated considering different control penalties and different state norms into the cost function (4.11). Then, DNS have been performed applying control feedback through boundary conditions for a couple of Reynolds numbers that have been widely studied in literature, namely $Re = 1500$ and $Re = 3500$. In all simulations, the dimensions of the computational domain have been $L_x = 4\pi$ and $L_z = 2\pi$. In particular, for $Re = 1500$, control gains have been computed for an array of wavenumbers (α, β) considering $0 \leq \alpha \leq 64$ and $-64 \leq \beta \leq 64$. Computation of a single kernel at this Reynolds number has required about 4 hours of CPU time on a single dual-CPU Intel using Matlab Parallel Computing Toolbox for the solution of CARE for each wavenumber pair. Convolution kernels computed using this approach are depicted in Figures 4.1 - 4.4. What can be immediately observed is that although different state norms have been considered, all kernels for wall-normal velocity angle away from the wall in the upstream direction, while those for vorticity appear as an-

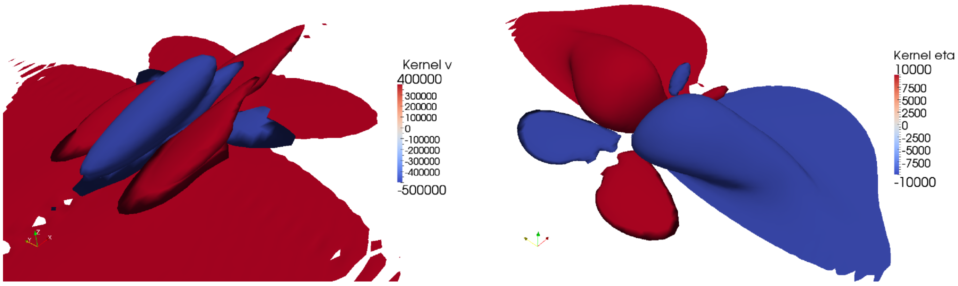

(a) *Kernel for wall-normal velocity* v (b) *Kernel for wall-normal vorticity* η

Figure 4.3: Localized controller gains relating the state x to the control forcing u at walls: visualized are positive (red) and negative (blue) isosurfaces at 6% of the peak value. Kernels were computed at $Re = 1500$ by using *enstrophy norm* and $\rho = 10^{-2}$ in the cost function.

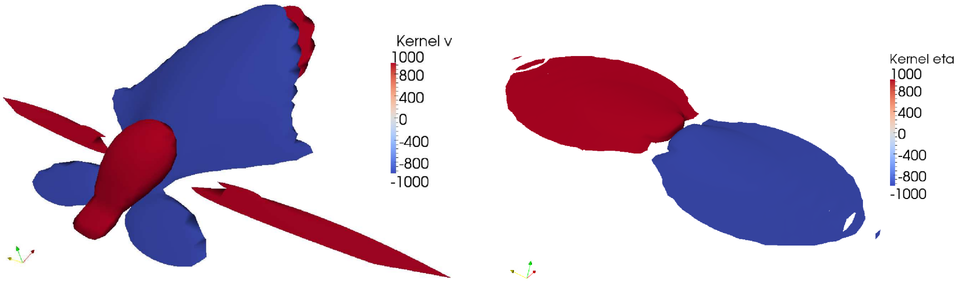

(a) *Kernel for wall-normal velocity* v (b) *Kernel for wall-normal vorticity* η

Figure 4.4: Localized controller gains relating the state x to the control forcing u at walls: visualized are positive (red) and negative (blue) isosurfaces at 6% of the peak value. Kernels were computed at $Re = 1500$ by using *measure-based norm* and $\rho = 10^{-2}$ in the cost function.

tisymmetric bulges more or less flat depending on the state norm used. These shapes are particularly meaningful since they interact with turbulent structures by contrasting the convective delay, which requires to anticipate flow perturbations inside the domain by applying wall actuation downstream.

As for DNS performed at $Re = 1500$, they have required about 14 days of computational time and they were run on cluster *Zeno*, a set of 10 dual-CPU Intel Xeon provided by the Department of Aerospace Engineering of Politecnico di Milano. Each simulation was run creating two threads on a single computer in order to exploit the parallelization performances of our DNS code. Approximately more than 2 months of CPU time was taken. Results have shown that energy norm is an excellent choice for targeting drag. However, the choice of the reference profile $U(y)$ (Figure 4.7) in kernel generation phase has a significant effect of overall performances. As a matter of fact, when using a turbulent reference profile a maximum drag reduction of 18% can be achieved, and overall performances appear quite independent of control penalty, as we can notice from Figures 4.5. On the other hand, by using Poiseuille laminar profile, the statistics of the controlled flow show improved performances and a richer behavior (Figure 4.6). In particular, for $\rho = 10^{-4}$ actual relaminarization has been observed with flow statistics

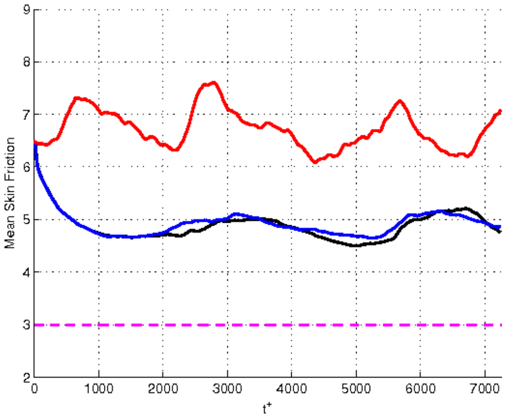

(a) *Mean Skin Friction*

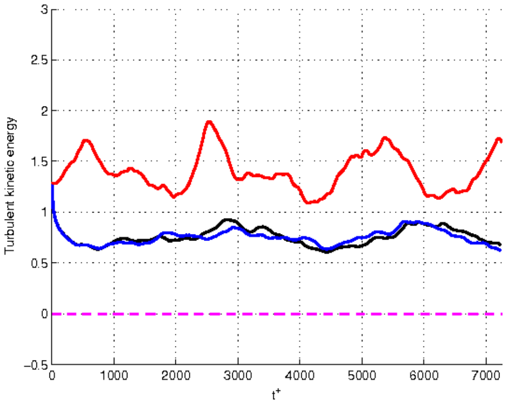

(b) *Turbulent kinetic energy*

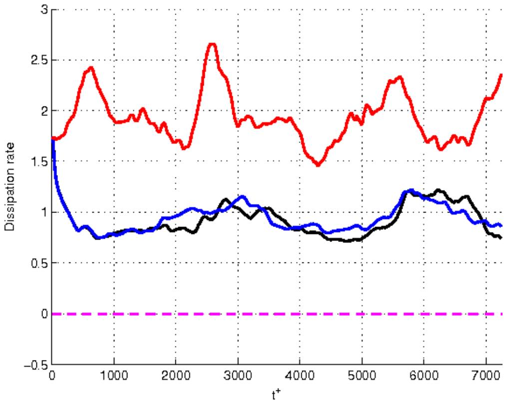

(c) *Dissipation rate*

Figure 4.5: Main statistics of the uncontrolled (red line) and controlled flow at $Re = 1500$ using *energy norm*, turbulent reference profile and different control penalties ρ, namely 10^{-2} (black line) and 10^{-4} (blue line) with respect to laminar flow (magenta line).

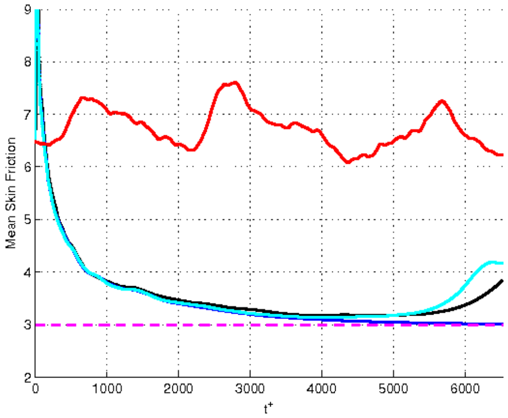

(a) *Mean Skin Friction*

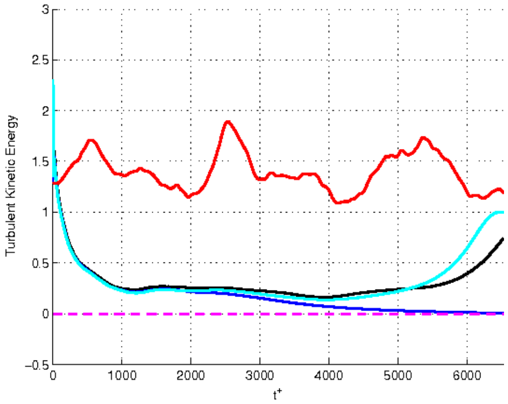

(b) *Turbulent kinetic energy*

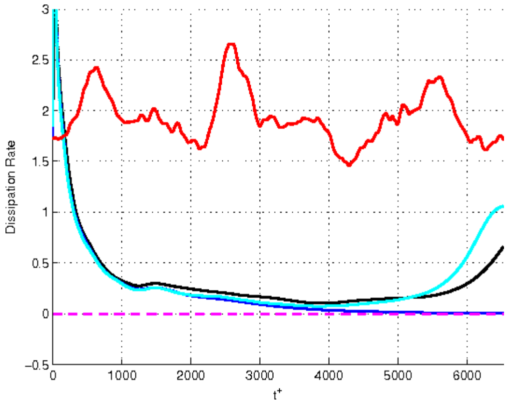

(c) *Dissipation rate*

Figure 4.6: Main statistics of the uncontrolled (red line) and controlled flow at $Re = 1500$ using *energy norm*, Poiseuille reference profile and different control penalties ρ, namely 10^{-2} (black line), 10^{-3} (blue line), 10^{-4} (cyan line) and 10^{-5} (green line) with respect to laminar flow (magenta line).

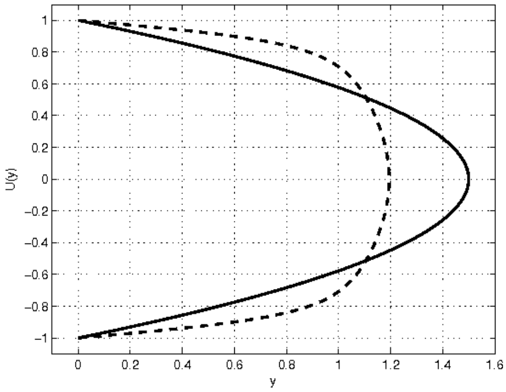

Figure 4.7: Comparison between laminar and turbulent reference profile $U(y)$ at $Re = 1500$.

slowly evolving towards ceiling laminar condition, thus determining a maximum drag reduction of nearly 53%. Surprisingly, this is the first result in flow control literature of relaminarization at $Re = 1500$ by adopting a LQR control approach with constant gains. Before this, actual relaminarization has been obtained using a LQR control in [26] combined with a sort of gain-scheduling of the reference velocity profile which was varied from turbulent to laminar as simulation advanced. The possible reasons why this result has never been attained before are many. First of all, as mentioned before, with small values of control penalty ρ standard Schur-Hamilton Riccati solvers have been proved to produce inaccurate solution. In the present work, Newton-Kleinman iterative solver has always been used in cascade in order to achieve further accuracy in the solution. Furthermore, by using Poiseuille reference profile, skin friction values exhibit a prominent overshooting at the very beginning of the simulation. This could lead to possible numerical problems in the evaluation of wall derivatives and has also a limiting effect on time-step in the semi-implicit DNS code, thus slowing down the simulation. Actually, relaminarization is the highest possible result in turbulent drag reduction, if our aim is to obtain a net power saving by using blowing/suction actuators at wall, as analytically demonstrated by Bewley, whose proof is reported in Appendix A. Moreover, this is consistent with the assertion that turbulence in channel flow is an essentially linear process [36] and a linear controller is sufficient to suppress turbulence at least at low Reynolds numbers. Then, this effective set of control parameters has been tested through DNS by considering a different flow field as initial condition. Results (Figure 4.8) have shown that relaminarization process is independent of the initial conditions of the flow. The only drawback of this control scheme is that it requires high performances from blowing/suction actuators. As a matter of fact, when control is applied at the very beginning of the simulation, wall actuation reaches up to 70% of bulk velocity. For these reason, the effect of actuator saturation at 10% of bulk velocity on overall performances has been investigated. Results have shown that control peak values are effectively reduced in the transitory whereas no noteworthy performance degradation has been observed, as can be stated from Figure 4.9.

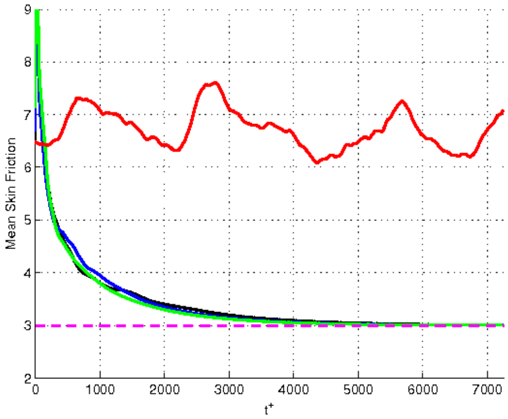

Figure 4.8: Mean skin friction of the uncontrolled (red line) and controlled flow at $Re = 1500$ using *energy norm*, Poiseuille reference profile and $\rho = 10^{-4}$. Three different initial conditions have been considered in DNS (blue, black and green lines).

Table 4.1: Drag reduction DR and net power saving P_{SP} of feedback control using energy norm and turbulent reference profile.

ρ	DR	P_{Net}
$1\,10^{-2}$	28.8%	15%
$1\,10^{-4}$	28.1%	13.6%

Visualizing the flow field during relaminarization process also offers a valuable occasion of observing how blowing/suction applied at walls acts in order to manipulate and destroy turbulent structures. What can be inferred from Figures 4.10 - 4.12 is that suction is introduced in the proximity of high-speed streaks, while a blowing action is introduced under low-speed streaks. The same happens for sweep and injection phenomena that characterize wall turbulence, as outlined in Chapter 1. In particular, suction is applied in presence of injection events, while blowing occurs when sweep events take place. In this way, the cycle of near-wall turbulence generation is interrupted, causing the flow to fully relaminarize.

Now, if we are interested in net power P_{Net} saved thanks to wall feedback control, we need to compute the power P_{SP} spent for actuation. For this purpose, we used the formula proposed in [5]:

$$P_{SP} = \frac{1}{T}\int_T \int_A \left(|\phi|\frac{\phi^2}{2} + |\phi|(p - \bar{p}) \right) dA\, dt \tag{4.91}$$

where A is the area covered by actuators and $\bar{p}$ is the average wall pressure. Results are shown in Tables 4.1 and 4.2.

As for the other control laws they proved to have limited impact on drag reduction. As a matter of fact, kernels based on measure norm provided a maximum drag reduction of about 15% and net saving of around 12%. In particular weak dependence has been observed of control penalty ρ on overall performances. A possible explanation

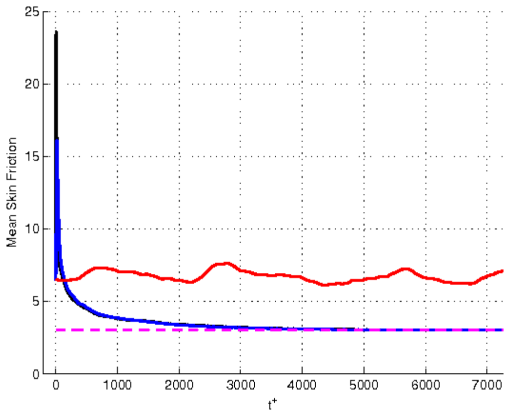

(a) *Mean skin friction*

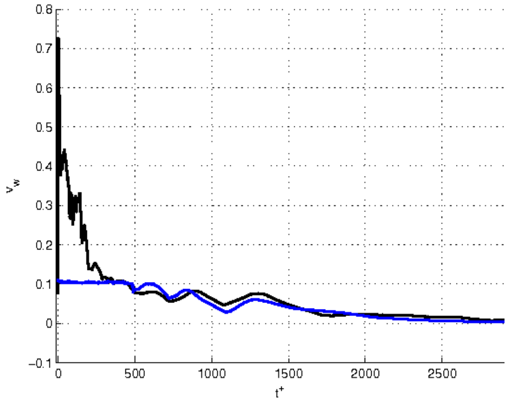

(b) *Control peak value*

Figure 4.9: Effect of actuator saturation on drag reduction at $Re = 1500$ using *energy norm*, Poiseuille reference profile and $\rho = 10^{-4}$: uncontrolled flow (red line), controlled flow without (black line) and with saturation (blue line).

to this behavior may be found by looking at the shape of the associated convolution kernels in Figure 4.4. In facts, these kernels, with respect to the others, appear to be confined to near-wall region, that leads to poor flow manipulation capability. Considering enstrophy norm, instead, a maximum drag reduction of nearly 25% has been achieved for $\rho = 10^{-4}$, but simulations have suffered by strong numerical instability, due to the high values of control actuation. For this reason it is not surprising that, among the possible combinations of control penalties and reference velocity profiles, none of them has led to positive net drag reduction. Then, as far as dissipation norm is concerned, it proved to yield a maximum drag reduction of about 30% for $\rho = 10^{-3}$ by using Poiseuille reference velocity, as we can see in Figure 4.13. Unfortunately, as for enstrophy norm, the power spent for actuation is very high, and net power saving is very limited, if not negative, as indicated in Table 4.3.

Finally, convolution kernels have been designed for reducing the drag of a turbulent channel flow at a higher Reynold number, namely $Re = 3500$. This scenario has required to account for a wider array of wavenumbers (α, β), i.e. $0 \leq \alpha \leq 128$ and

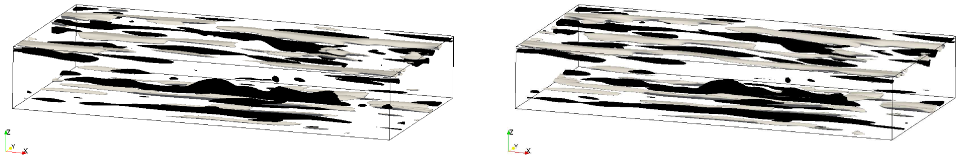

(a) *Frame at* $t^+ = 7.5$ (b) *Frame at* $t^+ = 15$

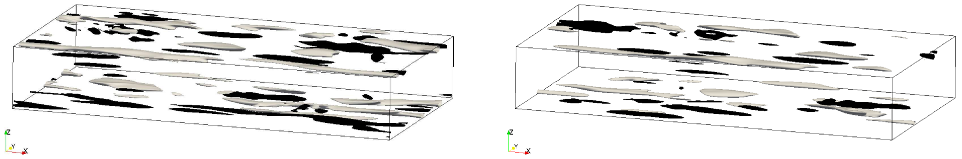

(c) *Frame at* $t^+ = 75$ (d) *Frame at* $t^+ = 150$

Figure 4.10: Three-dimensional view at different time steps of a turbulent channel flow at $Re = 1500$ controlled by using energy norm and $\rho = 10^{-4}$: visualized are high- (light) and low- (dark) speed streaks at 30% of bulk velocity.

Table 4.2: Drag reduction DR and net power saving P_{Net} of feedback control using energy norm and Poiseuille reference profile.

ρ	DR	P_{Net}
$1\,10^{-3}$	47.5%	39.1%
$5\,10^{-4}$	52.6%	46.1%
$1\,10^{-4}$	52.3%	47.5%
$5\,10^{-5}$	51.2%	44.8%
$1\,10^{-5}$	49.4%	38.7%

$-128 \leq \beta \leq 128$, during kernel design, due to energetic considerations. The computation of the whole set of feedback gains has required approximately 40 hours of CPU time on a dual-core Intel using Matlab Parallelization Toolbox for the solution of the CARE associated to each wavenumber pair. Direct Numerical Simulations have been run on the cluster of University of Salerno, where they took 4 days each using 10 AMD Opteron quad-core machines for a total of more than 20 months of CPU time. Results have shown that using Poiseuille reference profile in this case leads to relevant drag increase, while things get better if turbulent profile is adopted. This happens because the flow is very far from laminar condition (Figure 4.14), hence Poiseuille profile is no longer representative of flow field. Furthermore, as suggested in [26], we introduced

Table 4.3: Drag reduction DR and net power saving P_{SP} of feedback control using dissipation norm and Poiseuille reference profile.

ρ	DR	P_{Net}
$1\,10^{-2}$	24.9%	−30.1%
$1\,10^{-3}$	31.9%	6.6%
$1\,10^{-4}$	30.5%	3.2%
$1\,10^{-5}$	30.1%	3.1%

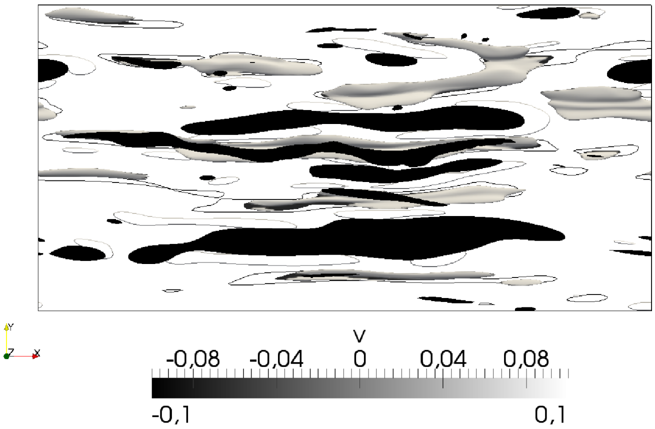

(a) *Frame at* $t^+ = 7.5$

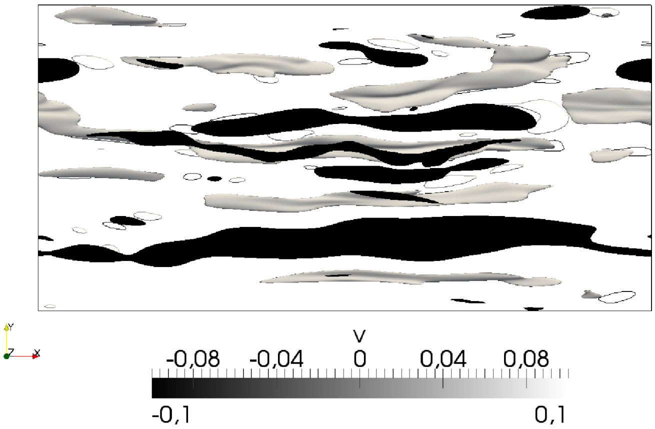

(b) *Frame at* $t^+ = 15$

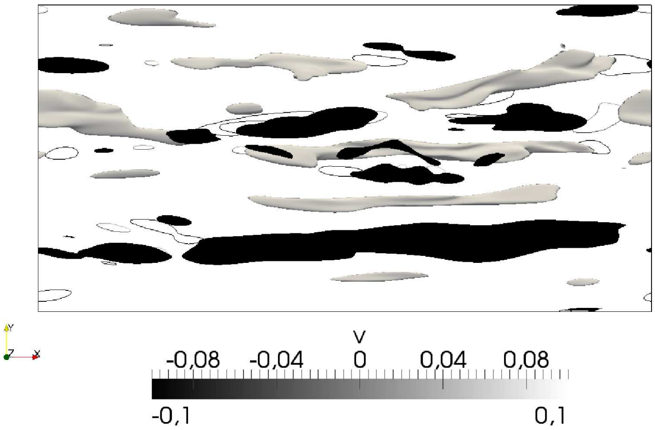

(c) *Frame at* $t^+ = 40$

Figure 4.11: Top view at different time steps of the lower half of a turbulent channel flow at $Re = 1500$ controlled by using energy norm and $\rho = 10^{-4}$: visualized are high- (light) and low- (dark) speed streaks at 30% of bulk velocity. Control actuation at wall is represented by contours graduated according to the legend.

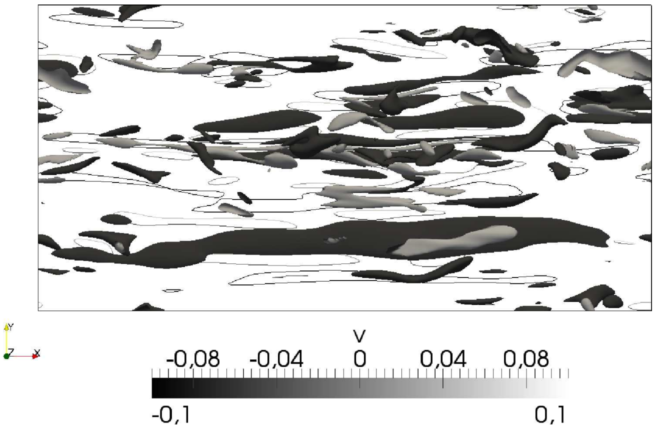

(a) *Frame at* $t^+ = 7.5$

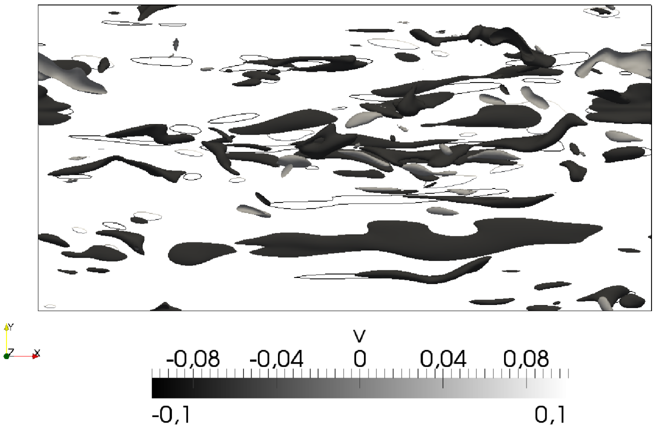

(b) *Frame at* $t^+ = 15$

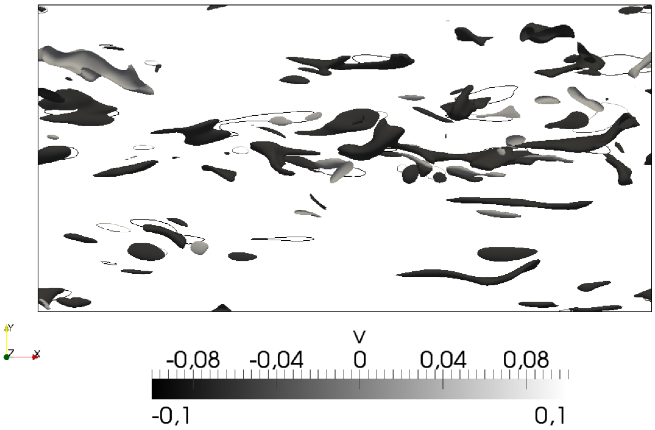

(c) *Frame at* $t^+ = 40$

Figure 4.12: Top view at different time steps of the lower half of a turbulent channel flow at $Re = 1500$ controlled by using energy norm and $\rho = 10^{-4}$: visualized are injection (light) and sweep (dark) events.Control actuation at wall is represented by contours graduated according to the legend.

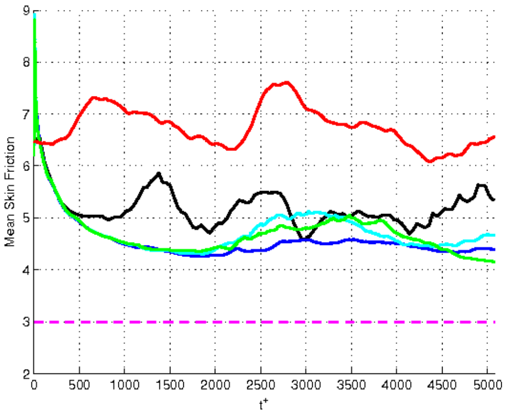

(a) *Mean Skin Friction*

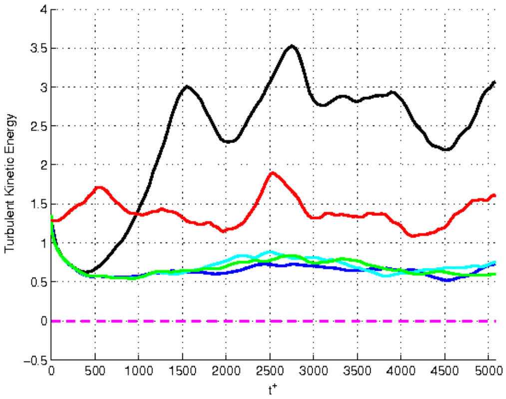

(b) *Turbulent kinetic energy*

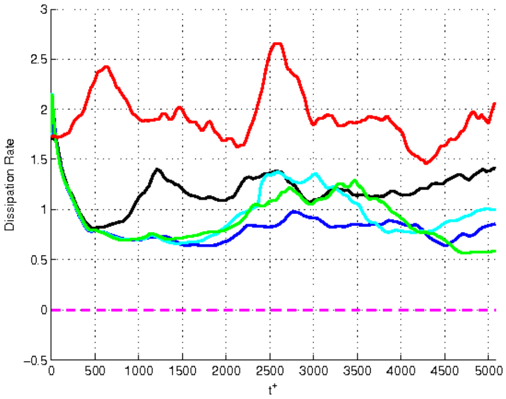

(c) *Dissipation rate*

Figure 4.13: Main statistics of the uncontrolled (red line) and controlled flow at $Re = 1500$ using *dissipation norm* and different control penalties ρ, namely 10^{-2} (black line), 10^{-3} (blue line), 10^{-4} (cyan line) and 10^{-5} (green line) with respect to laminar flow (magenta line).

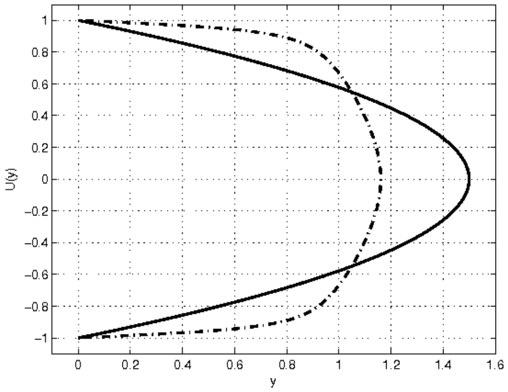

Figure 4.14: Comparison between laminar and turbulent reference profiles $U(y)$ at $Re = 3500$.

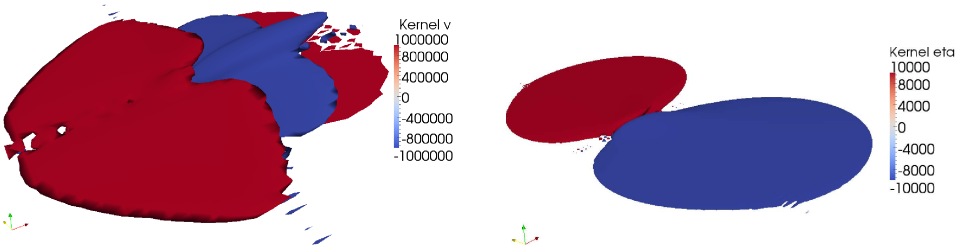

(a) *Kernel for wall-normal velocity* v **(b)** *Kernel for wall-normal vorticity* η

Figure 4.15: Localized controller gains relating the state x to the control forcing u at walls: visualized are positive (red) and negative (blue) isosurfaces at 6% of the peak value. Kernels were computed at $Re = 3500$ by using *energy norm* with smoothing function $f(y)$ and $\rho = 10^{-2}$ in the cost function.

a weight function $f(y)$ in the integrand of energy norm, which has proved to achieve the best performances at $Re = 1500$. Such function is defined as $f(y) = 1 + \bar{U}'(y)$ and the proposed effect is to indirectly target the coupling term L_C of Orr-Sommerfeld and Squire operator (3.32). Looking at kernel shape (Figure 4.15), the introduction of function $f(y)$ has led to convolution kernels that are more localized to near-wall part of the flow field.

Results in Figure 4.16 have shown that a maximum drag reduction of nearly 28% can be achieved with a net saving of about 18%. Moreover, it has been observed that overall performances are not affected by the choice of control penalty ρ, thus suggesting that an intrinsic limit exists in the application of a linear feedback control scheme when nonlinearities become relevant at high Reynold numbers.

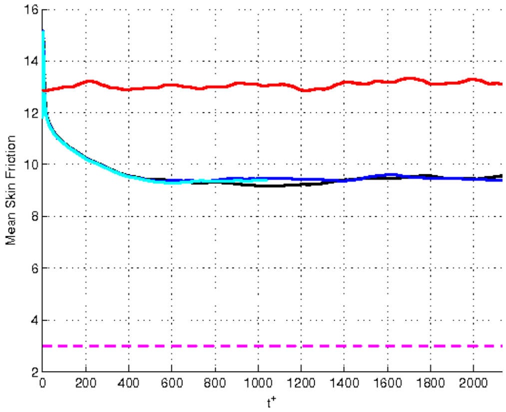

(a) *Mean Skin Friction*

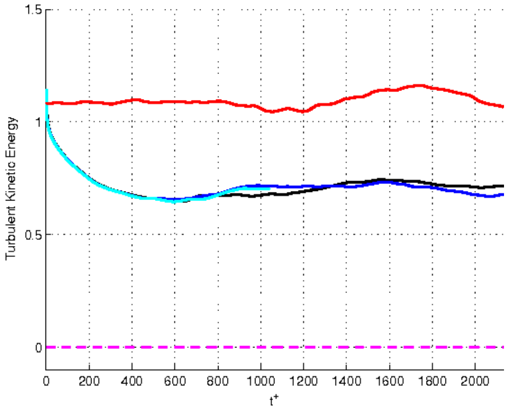

(b) *Turbulent kinetic energy*

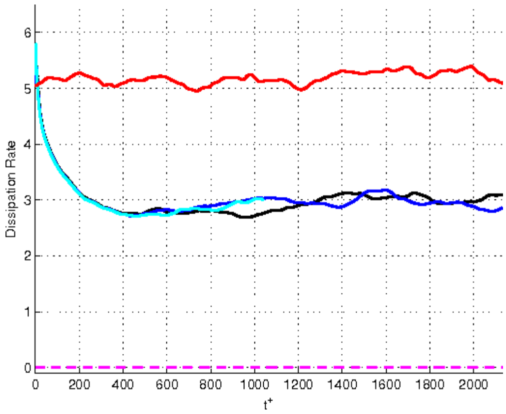

(c) *Dissipation rate*

Figure 4.16: Main statistics of the uncontrolled (red line) and controlled flow at $Re = 3500$ using *energy norm*, turbulent reference profile and different control penalties ρ, namely 10^{-2} (black line), 10^{-3} (blue line) and 10^{-4} (cyan line) with respect to laminar flow (magenta line).

Chapter 5

Optimal Output Feedback Control

Optimal state feedback control has been proved to yield very good performances in reducing drag in a turbulent channel flow at the Reynold numbers we have considered. Unfortunately, in real applications the knowledge of the entire state of the system is hardly available, since it would require to mount sensors inside the channel flow, solution that is clearly unpractical and could give origin to unsought load effects. For this reason, the present chapter address the issue of finding an optimal control law based solely on feedback of wall-measurement information. What follows is an analytical derivation of such control approach. After that, some useful tools will be introduced and applied in order to assess the effectiveness of output feedback with respect to state feedback for the present flow control framework.

5.1 Analytical derivation

Direct feedback of measurement vector y means considering a control input $u = -Ky$ acting on the linear time-invariant system considered in Chapter 4. With these expression, after manipulations of LQR cost function J, we get the following expression:

$$\begin{aligned} J = \frac{1}{2} Tr \left\{ PX_0 + \Lambda[(A - BKC)^T P + P(A - BKC) + \right. \\ \left. + Q + C^T K^T RKC] \right\} \end{aligned} \tag{5.1}$$

where X_0 is the initial state vector at time $t = 0$. Now, by setting to zero all the derivatives, we find

$$\begin{cases} \dfrac{\partial J}{\partial \Lambda} = (A - BKC)^T P + P(A - BKC) + Q + C^T K^T RKC = 0 & \text{(5.2a)} \\ \dfrac{\partial J}{\partial P} = X_0 + (A - BKC)\Lambda + \Lambda(A - BKC)^T = 0 & \text{(5.2b)} \\ \dfrac{\partial J}{\partial K} = RKC\Lambda C^T - B^T \Lambda C^T = 0 & \text{(5.2c)} \end{cases}$$

hence, from Equation (5.2c), we obtain

$$K = R^{-1} B^T \Lambda C^T (C \Lambda C^T)^{-1} \tag{5.3}$$

As we can see, the system is highly nonlinear and totally coupled, so that it is not possible to obtain the solution from a single Riccati equation as in full state approach. In order to overcome this deadlock, an iterative procedure has been implemented based on steepest descent technique. The algorithm we have developed leverages the seminal work of Levine appearing in [45] and [46]. It starts by defining an initial value F for the cost function and the tolerance on the minimum step size α_{min}. Then, considering an initial stabilizing solution K, the algorithm involves the following steps:

1. Calculate P with Equation (5.2a)
2. Calculate Λ with Equation (5.2b)
3. Set $K_0 = K$
4. Calculate K with Equation (5.3)
5. Calculate $\Delta K = K - K_0$
6. Set $\alpha = 1$
7. Calculate $K = K_0 + \alpha \Delta K$
8. Calculate P with Equation (5.2a)
9. Calculate $J = \frac{1}{2} Tr\left\{P X_0\right\}$
10. Set $\alpha = \alpha/2$
11. If the system is stable and $J < F$, then set $F = J$, else go to 7
12. If $\alpha < \alpha_{min}$ then ends, else go to 2

It is to remark, however, that even if the existence of a global minimum is assured, possible numerical problems may occur due to the presence of multiple stationary solutions. For these reasons, optimization has been repeated starting from different initial solutions, until the cost function F has reached a sufficient degree of performance, that could not coincide with the global minimum.

5.2 Measures of performance

In order to assess the performances of output feedback control with respect to LQR control, we have calculated the feedback gains for a wavenumber pair $(\alpha\,\beta)$, then we have applied the performance measures outlined in [7] in order to compare the results with full state control developed in Chapter 4. A useful tool which has been proved to be particularly meaningful is the concept of H_2 and H_∞ norm of disturbance-to-state function. As a matter of fact, H_2 norm of the transfer function of a system represents an estimate of the expected rms value of the transfer function output with a unitary input, whereas H_∞ norm is a measure of worst case amplification of the disturbance affecting the system. More specifically, given a transfer function $T_{nx}(s)$ in Laplace domain, defined as

$$X(s) = Q^{1/2}(sI - A)^{-1} B_n\, N(s) \tag{5.4}$$

where A is the state matrix of the system, B_n the input disturbance matrix, Q the state weight in optimal control cost function, $N(s)$ and $X(s)$ the input disturbance and state vector in Laplace domain, respectively. Then the H_2 norm of $T_{nx}(s)$ is defined as

$$\|T_{nx}\|_2 = \frac{1}{2\pi}\int_{-\infty}^{\infty} Tr\{T_{nx}(j\omega)^T T_{nx}(j\omega)\}\, d\omega \tag{5.5}$$

However, this formulation is not particularly amenable to numerical computation, so we preferred to calculate the H_2 norm as follows:

$$\|T_{nx}\|_2 = \sqrt{Tr\{B_n^T L B_n\}} \quad \text{where} \quad A^T L + LA + Q = 0 \tag{5.6}$$

As for H_∞ norm, it is defined as

$$\|T_{nx}\|_\infty = \sup_\omega \sigma_{max}[T_{nx}(j\omega)] = \gamma \tag{5.7}$$

where σ_{max} is the maximum singular value. Unfortunately, a closed form does not exist to compute such norm, but it can be sought by an iterative search. For this reason, we adopted the software *cvx*, an advanced convex solver developed by Grant and Boyd of Stanford University and described in [23], to solve an equivalent minimization problem:

$$\begin{cases} \min \gamma \\ \text{subject to} \quad \Re\left\{ eig \begin{bmatrix} A & \frac{1}{\gamma} B_n B_n^T \\ -Q & -A^T \end{bmatrix} \right\} < 0 \end{cases} \tag{5.8}$$

5.3 Output feedback performance assessment

In order to understand how output feedback behaves with respect to full-state control, H_2 and H_∞ norm of disturbance-to-state transfer function have been calculated at $Re = 1500$ for a couple of wavenumbers $\alpha = 1$ and $\beta = 0$, using different control

Table 5.1: Performance of optimal state feedback controller at $Re = 1500$ for $\alpha = 1$ and $\beta = 0$ using different state norms and different control penalties.

State norm	ρ	$\|T_{dx}\|_2$	$\|T_{dx}\|_\infty$
(No control)	-	453.2	10354
Energy	10^{-2}	101.8	2876
	10^{-3}	98.2	2469
	10^{-4}	89.7	2201
	10^{-5}	89.4	2197
Dissipation	10^{-2}	121.0	3005
	10^{-3}	101.3	2711
	10^{-4}	98.5	2555
	10^{-5}	97.1	2520

Table 5.2: Performance of optimal output feedback control at $Re = 3500$ for $\alpha = 1$ and $\beta = 0$ using different state norms and different control penalties.

State norm	ρ	$\|T_{dx}\|_2$	$\|T_{dx}\|_\infty$
(No control)	-	453.2	10354
Energy	10^{-2}	441.2	9810
	10^{-3}	431.3	9788
	10^{-4}	401.6	9665
	10^{-5}	397.3	9651
Dissipation	10^{-2}	442.6	9891
	10^{-3}	434.4	9833
	10^{-4}	409.8	9677
	10^{-5}	399.1	9625

penalties ρ and the best performing state norms that have emerged in Chapter 4, i.e. turbulent kinetic energy and dissipation rate. As for output feedback control, measures of shear stresses and pressure at both walls have been considered, exploiting relations outlined in Section 4.3.4. Results are resumed in Tables 5.1 and 5.2.

What appears clear is that LQR control effectively abates H_2 norm of disturbance-to-state transfer function, reducing at the same time H_∞ norm. In particular, we can observe that energy norm always performs slightly better than dissipation. As for output feedback, instead, results are rather poor. As a matter of fact, H_2 norm showed a maximum reduction of 15% against nearly 80% obtained with full state control. Interestingly, dissipation and energy norm have proved to perform more or less the same when only wall measurement information is available.

A possible explanation to this outcome can be found analyzing the dimensions of system matrices we are dealing with. In facts, optimal control design at $Re = 1500$ and 3500 involves state matrices A whose dimensions are about $\mathcal{O}(10^2) \times \mathcal{O}(10^2)$, while control input matrices B have size $\mathcal{O}(10^2) \times \mathcal{O}(1)$. Hence, gain matrices arising from full state control have size $\mathcal{O}(1) \times \mathcal{O}(10^2)$. When using output feedback control, instead, we have to account for measurement matrices C that, considering all measurements we can dispose of at walls, have size $\mathcal{O}(1) \times \mathcal{O}(10^2)$. Therefore, in this case gain matrices obtained through output feedback control have dimensions $\mathcal{O}(1) \times \mathcal{O}(1)$. Hence, it appears clear that output feedback control for the present purpose has much less authority than optimal state feedback, since its capability of modifying the spectrum of state matrices is strongly limited by gain size. For this reason, the design of a state estimator is made necessary.

Chapter 6

Observer-based Control

After having stated the low efficiency of output feedback control, an accurate state estimation is made necessary in order to implement active feedback control in a realistic framework, where we can dispose only of wall measures. The present chapter is organized as follows. Firstly, the state of the Art in estimation of wall-bounded flow will be described, then we will introduce the standard time-based approach to flow estimation, i.e. Kalman filter. Afterwards, we will introduce frequency-based Wiener-Hopf control technique, highlighting differences with respect to time-based approach. Then, the extension from single-input single-output (SISO) to single-input multi-output (SIMO) will be discussed considering numerical issues involved. Finally, results will be provided of parametric DNSs carried out in order to assess how control parameters affect overall performances.

6.1 State-of-the-Art review

It is surprising to notice that almost all publications that have appeared in literature concerning state estimation in wall-bounded flow adopted Kalman filter design. This solution can be found in the first approach to state estimation in a turbulent channel flow, which has appeared in [7] and [32]. In both works a linear Kalman filter has been designed leveraging Orr-Sommerfeld and Squire model in wavenumber space and a performance analysis has been carried out for a couple of wavenumbers. This approach has subsequently been extended in a second article [25] by considering an array of wavenumbers and performing estimation in a subcritical channel flow. It has been observed that linear models fail to capture the multiscale dynamics of turbulence, but they include the key terms responsible for the production of energy. As a matter of fact, the nonlinear terms in the Navier-Stokes equations scatter energy but do not directly contribute to energy production. However, in all these pioneering works, state covariance matrices appearing in Riccati equation arising from Kalman filter design have been modeled with simple identity matrices, since no preliminary assumptions on state noise were performed. This implies a constant variance of disturbances at each gridpoint and zero correlation of the disturbances at different gridpoints. Unfortunately, this covariance model does not converge to a resolved covariance distribution upon grid refinement.

In [6] a different strategy was investigated, that is model predictive estimation. This approach is based on iterative state and adjoint calculations optimizing the estimate of the state of the system so that the nonlinear evolution of the system model over a finite horizon in time matches the available measurements to the maximum extent possible. The optimization was performed iteratively using gradient information provided by calculation of an appropriately defined adjoint field driven by measurement misfits at the wall. This technique has provided noteworthy results, since in this framework it has been possible to account for the full nonlinear evolution of the system. However, this strategy has proved to be computationally expensive, as it required iterative marches of the state and adjoint fields over the time horizon of interest in order to obtain the state estimate. Due to this drawback, this approach has lost consideration in flow control literature since it is not possible to refine it in order to adapt it to practical implementation. Hence, attention has shifted towards the improvement of Kalman filter estimation.

In [27] a physical parameterization, which has been proved to converge upon grid refinement, has been introduced to properly model the external disturbances, initial conditions and measurement noises that can affect perturbed laminar flows. Results have led to the conclusion that a Kalman filter with time-varying feedback gains is necessary in order to minimize the initial transient in the estimation error when the estimation is turned on. Moreover, it has been noticed that when the flow perturbations are large enough to appreciate significant nonlinearities affecting the system, then an extended Kalman filter which incorporates the system nonlinearities into the estimator model outperforms the standard linear Kalman filter. Besides, in [11] Kalman and extended Kalman filters that were previously developed by the same group work have been tested for state estimation in a turbulent channel flow. A key step in solving the estimation problem has been the measurement of the second-order statistics of state noise through DNS. Then, this information has been used to build state covariance matrices in the estimator design phase, where all three measurements available at walls were used. As expected, the nonlinear extended Kalman filter was found to outperform the linear Kalman filter. However, it has been found that the estimated state in linear Kalman filter deteriorates more rapidly with the distance from the wall, whereas extended Kalman filter captures better the structures farther into the domain. Moreover, they observed an approximate correspondence of the performance of the extended Kalman filter with the model-predictive estimator built in [6] with a favorable computational time saving. However, in order to implement Kalman filter theory, the artificial assumption of white noise was made, thus discarding the entire time structure of the state noise.

This limitation has been overcome only in [52], where a frequency-domain approach has been suggested based on Wiener filter. As a matter of fact, in this framework it is possible to properly account for the full space-time structure of the state noise by measuring it through DNS. Furthermore, it can be proved that this filter is the best possible linear time-invariant filter to adopt for the present estimation problem, since no assumptions other than linearity of the model are introduced. Results have shown that by using a single wall measurement, Wiener filter always outperforms Kalman filter.

6.2 Kalman filter theory

Kalman filter is the most common approach adopted in literature when dealing with state estimation. For this reason, it is not surprising that it has quickly become a standard approach also in flow estimation. Since the knowledge of the actual state is unavailable the key idea is to get an estimate of the state $\hat{x}$ from the measurements available. The problem is stated as follows:

$$\begin{cases} \dot{x} = Ax + Bu + B_n n & \text{(6.1a)} \\ y = Cx + D_{yd} d & \text{(6.1b)} \end{cases}$$

$$\begin{cases} \dot{\hat{x}} = A\hat{x} + Bu + L(y - \hat{y}) & \text{(6.2a)} \\ \hat{y} = C\hat{x} & \text{(6.2b)} \end{cases}$$

where (6.1) are the equations of a LTI dynamic model, whereas equations (6.2) govern the dynamics of the state observer. In these context, matrix L represents the observer gain matrix used for the feedback of the difference between actual measures y and their estimates $\hat{y}$. Kalman filter theory provides tools to determine optimal values for this matrix. The first assumption is that state noise n and measurement noise d are uncorrelated Gaussian noise processes, which can be completely defined through their covariance matrices W_{nn} and W_{dd}, respectively. Then, after introducing the estimate error $e = x - \hat{x}$, by combining Equations (6.1) and (6.2), we get

$$\dot{e} = (A - LC)e + B_n n - LD_{yd} d \tag{6.3}$$

The variance error σ_{ee}^2 can be determined as the solution of the following Lyapunov equation:

$$(A - LC)\sigma_{ee}^2 + \sigma_{ee}^2 (A - LC)^T + B_n W_{nn} B_n^T - LD_{yd} W_{dd} D_{yd}^T L^T = 0 \tag{6.4}$$

Hence, matrix L must be chosen in order to minimize the objective function

$$J = Tr\left\{W_{ee}\sigma_{ee}^2\right\} \tag{6.5}$$

where W_{ee} is a weight matrix introduced to express the relative importance between the components of state estimate error. This problem is cast in the form of a constrained minimization, since σ_{ee}^2 must satisfy Equation (6.4), so we account for this condition by introducing a proper Lagrange multiplier:

$$J = Tr\left\{W_{ee}\sigma_{ee}^2 + \Lambda[(A-LC)\sigma_{ee}^2 + \sigma_{ee}^2(A-LC)^T + B_n W_{nn} B_n^T + LD_{yd}W_{dd}D_{yd}^T L^T]\right\} \tag{6.6}$$

The global minimum of functional J is obtained by imposing stationary conditions to its derivatives:

$$\begin{cases} \dfrac{\partial J}{\partial \Lambda} = (A-LC)\sigma_{ee}^2 + \sigma_{ee}^2(A-LC)^T + B_n W_{nn} B_n^T + LD_{yd}W_{dd}D_{yd}^T L^T = 0 & \text{(6.7a)} \\ \dfrac{\partial J}{\partial \sigma_{ee}^2} = \Lambda(A-LC) + (A-LC)^T\Lambda + W_{ee} = 0 & \text{(6.7b)} \\ \dfrac{\partial J}{\partial L} = LD_{yd}W_{dd}D_{yd}^T - \sigma_{ee}^2 C^T = 0 & \text{(6.7c)} \end{cases}$$

Then, from Equation (6.7c) we obtain

$$L = \sigma_{ee}^2 C^T (D_{yd}W_{dd}D_{yd}^T)^{-1} \tag{6.8}$$

Furthermore, through some trivial manipulations, it can be proved that we can determine σ_{ee}^2 as the solution of the following Riccati equation:

$$A\sigma_{ee}^2 + \sigma_{ee}^2 A^T - \sigma_{ee}^2 C^T R^{-1} C\sigma_{ee}^2 + Q = 0 \tag{6.9}$$

Then, gain matrix L can be easily recovered as $L = PC^T R^{-1}$.

Time-based approach is particularly appealing because of its solid theoretical framework, however it has also many drawbacks. First of all, in real physical systems noise can be rarely modeled as a random process and often we have to deal with disturbances that may present a rich structure in frequency domain. Even if it can be proved that Kalman filter is optimal even for non-Gaussian noise [68], covariance matrices are decisively inadequate and limiting in order to represent actual noise spectrum.

Besides, when Kalman filter is associated to an optimal controller, linear quadratic Gaussian (LQG) technique requires the solution of two distinct Riccati equations, one for the controller and the other for the observer, according to seperation principle, which guarantees that controller and observer have independent dynamics. Then, after having solved these two design problems, controller and observer may be combined to develop a dynamic compensator to control the flow system. However, standard Riccati solvers based on Schur-Hamilton decomposition described in Chapter 4 have a computational time that scales with the cube of the dimension of state matrix A. Hence, this approach to compensator design quickly becomes highly time-requiring as the number of states increases, i.e. as the mesh grid gets more and more refined.

For all these reasons, we implemented a control technique in frequency domain based on Youla-Kucera parameterization [75] - [76], called Wiener-Hopf control. This strategy allows to compute in a single step the compensator transfer function obtained after design of both controller and observer. This interesting feature represents for our purpose an important property, since it can provide substantial computational savings. Besides, in Wiener-Hopf control many techniques are available which scale with

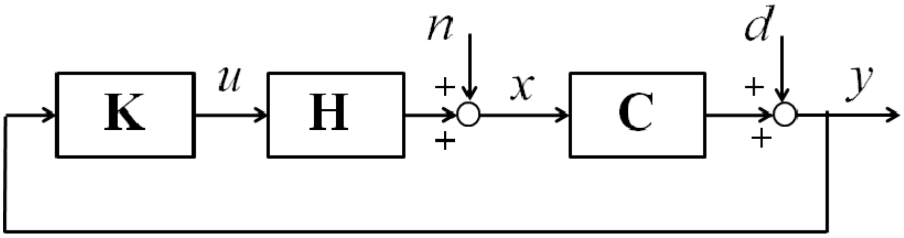

Figure 6.1: Classical closed-loop control scheme.

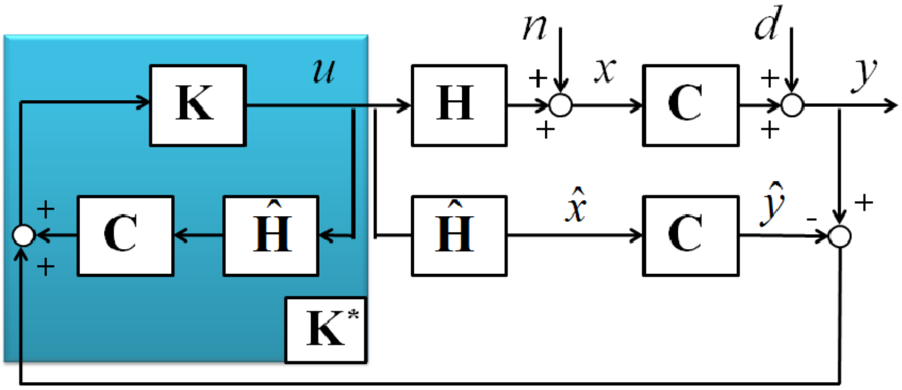

Figure 6.2: Alternative representation of closed-loop control scheme with transfer function modeling mismatch.

the square of matrix dimensions. Moreover, this frequency-based approach allows to directly exploit information concerning exact noise spectra, thus avoiding the introduction of expensive noise-shaping filters, required when using Kalman filter. Besides, if white noise is affecting the system, then the compensators calculated using LQG control approach and Wiener-Hopf theory are exactly the same. What follows, is a description of Wiener-Hopf control theory.

6.3 Wiener-Hopf optimal compensator design

Among the possible approaches to the problem, the most suitable way to define the compensator function $K(s)$ is the procedure described in [53]. The system to which we refer is represented in Figure 6.1, where with H we have indicated the input-to-state transfer function. With some manipulations it is possible to obtain an equivalent representation, as shown in Figure 6.2, where $\hat{H}$ represents the model we have realized of system transfer function. It can be easily shown by inspection that

$$e = d + Cn + C(H - \hat{H})u \tag{6.10}$$

where e represents the difference between feedback measure y and its estimate $\hat{y}$. So, if the model perfectly matches system dynamics, feedback is represented by noise com-

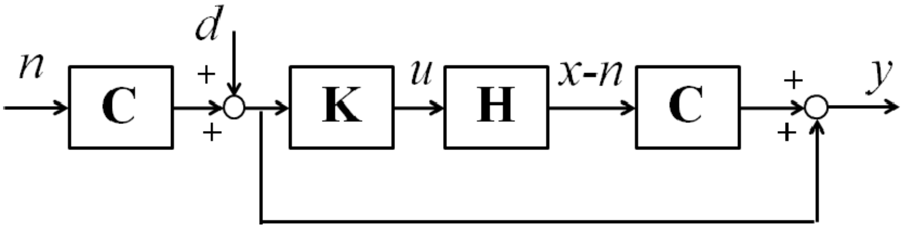

Figure 6.3: Noise-to-measure block diagram of the controlled system.

ponents alone. Then, to simplify the block-diagram we can notice that

$$u = Ky \tag{6.11}$$

$$C\hat{H}u = \hat{y} \tag{6.12}$$

By subtraction we get

$$(I - KC\hat{H})u = Ke \tag{6.13}$$

If now we introduce a new definition of control input, i.e. $u = K^* e$ and consider perfect matching between model $\hat{H}$ and actual system H, then we obtain the block-diagram shown in Figure 6.3. Compensator transfer function K can be recovered through the following relation:

$$K^* = (I - KCH)^{-1}K \tag{6.14}$$

Afterwards, we will define an objective function to be minimized, which closely reminds time-based LQR/LQG control:

$$J = \frac{1}{2}\int_{-\infty}^{\infty} \left(Tr\left\{Q\phi_{xx}\right\} + Tr\left\{R\phi_{uu}\right\}\right) df \tag{6.15}$$

where with symbol ϕ we have indicated spectral density function, whereas matrices Q and R represent state and control weights, respectively. From inspection, we can find the following relationships:

$$\begin{aligned} y &= (I + CHK^*)(Cn + d) \\ x &= HK^*d + (I + HK^*C)n \\ u &= K^*d + K^*Cn \end{aligned} \tag{6.16}$$

Spectral density functions ϕ_{xx} and ϕ_{uu} are then straightforwardly determined as

$$\begin{aligned} \phi_{xx} &= HK^*\phi_{dd}K^{*H}H^H + (I + HK^*C)\phi_{nn}(I + HK^*C)^H \\ \phi_{uu} &= K^*\phi_{dd}K^{*H} + KC\phi_{nn}C^HK^{*H} \end{aligned} \tag{6.17}$$

where superscript H denotes conjugate transpose. After substitution of Equation (6.17) into (6.15), we get

$$J = \frac{1}{2}\int_{-\infty}^{\infty} \Big(Tr\left\{ Q\phi_{nn} + QHK^{*}C\phi_{nn} + Q\phi_{nn}C^{H}K_{nn}^{*H}H^{H} + QHK^{*}C\phi_{nn}C^{H}K^{*H}H^{H} + \right. \\ \left. + QHK^{*}\phi_{dd}K^{*H}H^{H} \right\} + Tr\left\{ RK^{*}\phi_{dd}K^{*H} + RK^{*}C\phi_{nn}C^{H}K^{*H} \right\} \Big)\, df \tag{6.18}$$

However, this formulation leads to the design of a noncausal compensator, unless we enforce causality constraint by introducing an appropriate Lagrange multiplier, as follows:

$$J = \frac{1}{2}\int_{-\infty}^{\infty} \Big(Tr\left\{ Q\phi_{nn} + QHK_{+}^{*}C\phi_{nn} + Q\phi_{nn}C^{H}K_{+}^{*H}H^{H} + QHK_{+}^{*}C\phi_{nn}C^{H}K_{+}^{*H}H^{H} + \right. \\ \left. + QHK_{+}^{*}\phi_{dd}K_{+}^{*H}H^{H} \right\} + Tr\left\{ RK_{+}^{*}\phi_{dd}K_{+}^{*H} + RK_{+}^{*}C\phi_{nn}C^{H}K_{+}^{*H} \right\} + 2Tr\left\{ \Lambda_{-}K_{+}^{*} \right\} \Big)\, df \tag{6.19}$$

where subscript + indicates that only causal part has been considered. Now, if we derive Equation (6.19) with respect to K_{+}^{*H} and impose stationary conditions, we can find a closed form solution for compensator transfer function:

$$\frac{\partial J}{\partial K_{+}^{*H}} = H^{H}Q\phi_{nn}C^{H} + H^{H}QHK_{+}^{*}\phi_{dd} + H^{H}QHK_{+}^{*}C\phi_{nn}C^{H} + \\ + RK_{+}^{*}\phi_{dd} + RK_{+}^{*}C\phi_{nn}C^{H} + \Lambda_{-} = 0 \tag{6.20}$$

or, in a more elegant fashion:

$$(H^{H}QH + R)K_{+}^{*}(C\phi_{nn}C^{H} + \phi_{dd}) + \Lambda_{-} = -H^{H}Q\phi_{nn}C^{H} \tag{6.21}$$

Equation (6.21) is a Wiener-Hopf equation and different approaches, both analytical and numerical, are possible in order to solve it. What follows is a comprehensive description of the different techniques developed in literature to solve Wiener-Hopf problem.

6.3.1 Analytical solution

Mathematically speaking, Wiener-Hopf problem consists of finding two complex functions $K_{+}^{*}(j\omega)$ and $\Lambda_{-}(j\omega)$ satisfying the following relation on the imaginary axis [56]:

$$A(j\omega)K_{+}^{*}(j\omega) + \Lambda_{-}(j\omega) = B(j\omega) \tag{6.22}$$

where $A(j\omega)$ and $B(j\omega)$ are two Lipschitz-continuous functions. To solve this equation, we need to find a factorization of $A(j\omega)$ highlighting causal $A_{+}(j\omega)$ and noncausal part $A_{-}(j\omega)$, i.e.

$$A(j\omega) = \frac{A_{+}(j\omega)}{A_{-}(j\omega)} \tag{6.23}$$

After substitution in Equation (6.22), we get

$$\underbrace{A_+(j\omega)K_+^*(j\omega)}_{\phi_+(j\omega)} + \underbrace{\Lambda_-(j\omega)A_-(j\omega)}_{-\phi_-(j\omega)} = \underbrace{B(j\omega)A_-(j\omega)}_{f(j\omega)} \tag{6.24}$$

With the introduction of function $\phi(j\omega)$, Wiener-Hopf problem has been recast into a standard Hilbert problem, which can be stated as follows: let C be a smooth closed boundary, defined in complex set $\mathbb{C}$, $f(\tau)$ is a function satisfying Lipschitz condition on $\mathbb{C}$. We need to find functions $\phi_+(\tau)$ and $\phi_-(\tau)$, regular on $\mathbb{C}$ and Lipschitz continuous, satisfying

$$\phi_+(\tau) - \phi_-(\tau) = f(\tau), \quad \text{with} \quad \tau \in \mathbb{C} \tag{6.25}$$

In order to solve Hilbert problem, Plemelji provided the following formulas:

$$\begin{aligned} \phi_+(\tau) &= +\frac{1}{2}f(\tau) + \frac{1}{2\pi j}\int_C \frac{f(\xi)}{\xi - \tau}\,d\xi \\ \phi_-(\tau) &= -\frac{1}{2}f(\tau) + \frac{1}{2\pi j}\int_C \frac{f(\xi)}{\xi - \tau}\,d\xi \end{aligned} \tag{6.26}$$

By extending boundary C to infinity and letting $f(\tau) \to 0$ for $\tau \to \infty$, it is possible to consider the imaginary axis as boundary C.

However, Plemelji formulas (6.26) need the computation of a complex Cauchy integral. Solution of such integral is possible through the application of residue theorem: suppose C is a simply connected open subset of the complex plane and $a_1, \ldots, a_i, \ldots, a_n$ are finitely many points of U and f is a function which is defined and holomorphic on $U \setminus \{a_1, \ldots, a_i, \ldots, a_n\}$. If C is a rectifiable curve in U which bounds a_i, but does not meet any and whose start point equals its endpoint, then

$$\int_C f(z)\,dz = 2\pi j \sum_{i=1}^{n} Res(f, a_i) \tag{6.27}$$

where $Res(f, a_i)$ denotes the residue of f at a_i. If for a_i we consider the poles of function f and we call k_i the order of each pole, we can find a closed form for the residues:

$$Res(f, a_i) = \lim_{z \to a_o} \frac{1}{(k_i - 1)!}\frac{d^{k_i - 1}}{dz^{k_i - 1}}(z - a_i)^{k_i} f(z) \tag{6.28}$$

To our scope, these notions of complex analysis are sufficient. For further knowledge, the interested reader is referred to [1]. Then, once function $\phi_+(j\omega)$ is determined, compensator transfer function is easily recovered as

$$K_+^*(j\omega) = \frac{\phi_+(j\omega)}{A_+(j\omega)} \tag{6.29}$$

As mentioned before, this control technique leads to the same compensator obtained through LQG control design. In order to prove this statement, we will now consider, as an example, an optimal control of an industrial rigid servo-system, which is schemati-

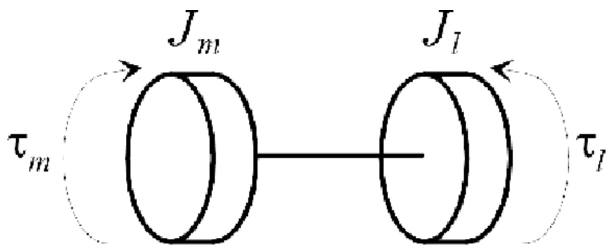

Figure 6.4: Schematic representation of an industrial rigid servo-system.

cally illustrated in Figure 6.4. Equations governing its system dynamics are:

$$\begin{cases} J_m\ddot{\theta}_m + D_m\dot{\theta}_m = \tau_m - \tau_{lm} \\ J_l\ddot{\theta}_l + D_l\dot{\theta} = n\tau_{lm} - \tau_l \\ \theta_m = n\theta_l \end{cases} \tag{6.30}$$

where subscripts m and l indicate motor and load part, respectively, whereas J is rotor inertia, D viscous damping, θ angular position, n the gear ratio and τ the torque. Then with τ_{lm} we have indicated torque exchanged between load and rotor part through the transmission. With some trivial manipulations, we can represent system dynamics with a unique equation, i.e.

$$\left(J_m + \frac{J_l}{n^2}\right)\ddot{\theta}_m + \left(D_m + \frac{D_l}{n}\right)\dot{\theta}_m = \tau_m - \frac{\tau_l}{n} \tag{6.31}$$

or, in a more compact fashion

$$J\ddot{\theta} + D\dot{\theta} = \tau_m - \tau_{lr} \tag{6.32}$$

In order to achieve state space formulation, we choose $\dot{\theta}$ as state variable x, while τ_m represents control input u, whereas τ_{lr} is considered as a torque disturbance n affecting the system. Finally, we choose to measure angular velocity $\dot{\theta}$, which is supposed to be affected by random noise d. We get:

$$\begin{cases} \dot{x} = -\frac{D}{J}x + \frac{1}{J}u + \frac{1}{J}n \\ y = x + d \\ u = -Kx \end{cases} \tag{6.33}$$

For feedback controller design, we define the following objective function:

$$J = \frac{1}{2}\int_0^\infty (qx^2 + ru^2)\,dt \tag{6.34}$$

Optimal gain K is recovered from solution of a Riccati equation:

$$\begin{aligned} A^T P + PA + Q - PBR^{-1}B^T P = 0 \\ -2\frac{D}{J}p + q - \frac{1}{rJ^2}p^2 = 0 \end{aligned} \tag{6.35}$$

We find two solutions, we take just the positive one:

$$p = JDr\left(\sqrt{\frac{q}{rD^2} + 1} - 1\right) \tag{6.36}$$

hence

$$K = R^{-1}BP = D\left(\sqrt{\frac{q}{rD^2} + 1} - 1\right) \tag{6.37}$$

For the observer we have to solve an analogous Riccati equation:

$$\begin{aligned} A\widetilde{P} + \widetilde{P}A + \widetilde{Q} - \widetilde{P}C^T\widetilde{R}^{-1}C\widetilde{P} = 0 \\ -2\frac{D}{J}\tilde{p} + \tilde{q} - \frac{1}{\tilde{r}}\tilde{p}^2 = 0 \end{aligned} \tag{6.38}$$

where $\tilde{q}$ and $\tilde{r}$ represent state and measure noise covariances, respectively. We get:

$$\tilde{p} = \frac{D\tilde{r}}{J}\left(\sqrt{\frac{\tilde{q}J^2}{\tilde{r}D^2} + 1} - 1\right) \tag{6.39}$$

hence

$$L = \widetilde{P}C^T\widetilde{R}^{-1} = \frac{D}{J}\left(\sqrt{\frac{\tilde{q}J^2}{\tilde{r}D^2} + 1} - 1\right) \tag{6.40}$$

Compensator transfer function in Laplace domain $L(s)$ then reads:

$$F(s) = K(sI - A + BK + LC)^{-1}L \tag{6.41}$$

If now we assume unitary parameters, we find:

$$F_{LQG}(s) = -\frac{(\sqrt{2}-1)^2}{j\omega + 2\sqrt{2} - 1} \tag{6.42}$$

As for Wiener-Hopf approach, the associated scalar equation is obtained by considering

$$\begin{aligned} H = (j\omega - A)^{-1}B = \frac{1}{j\omega + 1} \\ \phi_{nn} = H\tilde{q}H^H = \frac{1}{\omega^2 + 1} \end{aligned} \tag{6.43}$$

We get

$$\begin{aligned} \frac{(\omega^2+2)^2}{(\omega^2+1)^2}K_+^*(j\omega) + \Lambda_-(j\omega) = -\frac{1}{-j\omega + 1}\frac{1}{\omega^2 + 1} \\ A(j\omega)K_+^*(j\omega) + \Lambda_-(j\omega) = B(j\omega) \end{aligned} \tag{6.44}$$

Factorization of $A(j\omega)$ can be straightforwardly recovered by inspection:

$$A(j\omega) = \frac{A_+(j\omega)}{A_-(j\omega)} \qquad A_+(j\omega) = \frac{(j\omega + \sqrt{2})^2}{(j\omega + 1)^2} \qquad A_-(j\omega) = \frac{(-j\omega + 1)^2}{(-j\omega + \sqrt{2})^2} \tag{6.45}$$

Function f in Plemelji formulas (6.26) reads

$$f(j\omega) = -\frac{1}{(j\omega - \sqrt{2})^2 (j\omega + 1)} \tag{6.46}$$

Then, the associated Cauchy integral is

$$\frac{1}{2\pi j} \int_C \frac{f(z)}{z - j\omega}\, dz = \frac{1}{2\pi j} \int_{-j\infty}^{+j\infty} \frac{-1}{(z - j\omega)(z + 1)(z - \sqrt{2})}\, dz \tag{6.47}$$

This complex integrand has a pole of order 2 for $z = \sqrt{2}$ and two poles of order 1 for $z = j\omega$. In order to calculate the integral on the imaginary axis we need to define a half-circle path Γ in the right half of Gauss plane and let its radius go to infinity. As for the pole on the imaginary path, a semicircular path γ has to be followed in order to circumvent it, so:

$$\frac{1}{2\pi j} \int_C \frac{f(z)}{z - j\omega}\, dz = \frac{1}{2\pi j} \int_\Gamma \frac{f(z)}{z - j\omega}\, dz - \frac{1}{2\pi j} \int_\gamma \frac{f(z)}{z - j\omega}\, dz \tag{6.48}$$

Then

$$\frac{1}{2\pi j} \int_\Gamma \frac{f(z)}{z - j\omega}\, dz = Res(f,\, j\omega) + Res(f,\, \sqrt{2}) = -\frac{1}{(\sqrt{2} + 1)^2 (j\omega + 1)} \tag{6.49}$$

Now, we need to compute the integral over γ. Firstly, we parameterize variable z as follows:

$$z = j\omega + \varepsilon e^{j\theta}, \qquad -\frac{\pi}{2} \leq \theta \leq \frac{\pi}{2} \tag{6.50}$$

hence

$$\begin{aligned} \int_\gamma \frac{f(z)}{z - j\omega}\, dz &= \int_{-\pi/2}^{\pi/2} \frac{f(j\omega + \varepsilon e^{j\theta}) j \varepsilon e^{j\theta}}{\varepsilon e^{j\theta}}\, d\theta = \\ &= j \int_{-\pi/2}^{\pi/2} f(j\omega + \varepsilon e^{j\theta})\, d\theta \end{aligned} \tag{6.51}$$

Secondly, by letting the radius go to zero:

$$\begin{aligned} \int_{\gamma \to 0} \frac{f(z)}{z - j\omega}\, dz &= \lim_{\varepsilon \to 0} j \int_{-\pi/2}^{\pi/2} f(j\omega + \varepsilon e^{j\theta})\, d\theta = \\ &= j \int_{-\pi/2}^{\pi/2} f(j\omega)\, d\theta = j\pi f(j\omega) \end{aligned} \tag{6.52}$$

hence

$$\phi_+(j\omega) = \cancel{\frac{1}{2}f(j\omega)} - \frac{1}{(\sqrt{2}+1)^2(j\omega+1)} - \cancel{\frac{1}{2}f(j\omega)} = -\frac{1}{(\sqrt{2}+1)^2(j\omega+1)} \tag{6.53}$$

Thus, from (6.29), we get

$$K_+^*(j\omega) = -\frac{j\omega+1}{(j\omega+\sqrt{2})^2(\sqrt{2}+1)^2} \tag{6.54}$$

Finally, compensator transfer function is recovered from (6.14):

$$K_{WH}(j\omega) = -\frac{(\sqrt{2}-1)^2}{(j\omega+2\sqrt{2}-1)} \tag{6.55}$$

As can be easily observed, Equations (6.42) and (6.55) coincide.

6.3.2 Numerical solution

We have just seen how analytical solution of Wiener-Hopf equation requires long mathematical computation. Furthermore, if multiple inputs are considered, then impulse response is not scalar anymore, while if we consider multiple outputs for feedback, it is C that turns into a matrix. In these cases Wiener-Hopf equation has matrix coefficients, making analytical handling impracticable. Fortunately, numerical approach is decisively more appealing and straightforward. Starting from Wiener-Hopf equation (6.21), we apply inverse Fourier transform, obtaining the following convolution integrals:

$$\int_0^{+\infty} a(t-\tau)k_+(\tau)\,d\tau = b(t) \qquad t \geq 0 \tag{6.56}$$

$$\int_0^{+\infty} a(t-\tau)k_+(\tau)\,d\tau + \lambda_-(t) = b(t) \qquad t < 0 \tag{6.57}$$

After time discretization of the integral of (6.56), we obtain

$$\Delta t \sum_{p=1}^{n} a_{i-p}k_p = b_i \quad \text{with} \quad i = 0, \ldots, n \tag{6.58}$$

or, in matrix form

$$\Delta t \begin{bmatrix} a_0 & a_{-1} & a_{-2} & \dots & a_{-n} \\ a_1 & a_0 & a_{-1} & \dots & a_{-n+1} \\ a_2 & a_1 & a_0 & \dots & a_{-n+2} \\ \vdots & \vdots & \vdots & \vdots & \vdots \\ a_n & a_{n-1} & a_{n-2} & \dots & a_0 \end{bmatrix} \begin{bmatrix} k_0 \\ k_1 \\ k_2 \\ \vdots \\ k_n \end{bmatrix} = \begin{bmatrix} b_0 \\ b_1 \\ b_2 \\ \vdots \\ b_n \end{bmatrix} \tag{6.59}$$

$$Ak = b$$

Hence, determining the compensator transfer function simply requires the solution of a linear system. After that, vector $k(t)$ is Fourier-transformed back in frequency domain, in order to obtain $K(j\omega)$. It is to notice, however, that matrix A arisings after discretization of a SISO system has very peculiar properties, since it is always hermitian positive definite (hpd) and all terms on the same diagonal are equal. In particular, if a matrix has these particular symmetries, it is said to be in Toeplitz-like form. As for SIMO and MISO systems, instead, the elements a_i in matrix A are represented by matrices themselves, hence A is said to have a block Toeplitz structure.

This statement will be of fundamental importance for the solution of the linear system arising in Wiener-Hopf control design, since standard factorization techniques usually adopted to solve a linear system could be avoided. As a matter of fact, standard approaches to the solution of the linear system requires the factorization of LHS into two matrices, the first lower triangular, the second upper triangular. Solution is then recover after a step of forward-substitution and a subsequent step of backward-substitution. Typical factorization algorithms are mainly based on Gauss elimination method or Cholesky factorization, if the matrix is hpd. All these algorithms are able to handle nonsingular square matrices, but their computational time scales with N^3, where N is matrix dimension, whereas Toeplitz and block Toeplitz matrices, thanks to their symmetries, can be factorized with sophisticated algorithms which scale only with N^2.

Such algorithms can be broadly classified into two categories, namely Levinson-type and Schur-type. As for Levinson-type algorithms, they produce the factorization of the inverse of Toeplitz matrix, while Schur-type algorithms produce the factorization of the Toeplitz matrix itself. However, Levinson-type algorithms have the main drawback that they are limited to scalar Toeplitz matrices, while Schur-type algorithms, on the other hand, offer a greater flexibility and higher parallelization. What follows is a comprehensive description of the algorithms that have been developed in order to factorize Toeplitz matrices arising from Wiener-Hopf control theory, i.e. Cholesky and Schur factorizations.

Cholesky factorization

When a hermitian positive definite matrix needs to be factorized, the standard approach is to adopt Cholesky factorization. This straightforward algorithm is briefly outlined in the following. Let us call A the $N \times N$ hermitian positive definite matrix, a_{ij} its element in row i and column j and C its factorization. We have

$$A = C^H C \tag{6.60}$$

We first compute $c_{11} = \sqrt{a_{11}}$. Then for $i = 2, \ldots, n$ we calculate the diagonal term c_{ii} as

$$c_{ii} = \left(a_{ii} - \sum_{k=1}^{i-1} c_{ik}^2 \right)^{1/2} \tag{6.61}$$

and off-diagonal terms are evaluated as

$$c_{ij} = \left(a_{ij} - \sum_{k=1}^{j-1} c_{ik} c_{jk}^H \right) / c_{jj} \quad \text{for} \quad j = 1, \ldots, i-1 \tag{6.62}$$

As previously mentioned, the main drawback associated with this algorithm is the high computational cost, since by inspection it can be found that it requires $N^3/3$ flops, hence factorization time rapidly increases for high dimensional matrices.

Schur factorization

The Schur factorization algorithm that has been developed in the one outlined in [33]. In order to provide a description of how it works, let us consider a block Toeplitz hpd matrix A of size $mp \times mp$, where m is the size of each block, while p represents the number of blocks. The simpler case of scalar Toeplitz matrix can be readily recovered by considering $m = 1$. Now consider the first block row $\begin{bmatrix} \widehat{A}_1 & \widehat{A}_2 & \ldots & \widehat{A}_p \end{bmatrix}$. Since $\widehat{A}_1$ is a hpd matrix, we can find its Cholesky factorization $\widehat{A}_1 = C_1 C_1^H$, where C_1 is an $m \times m$ lower triangular matrix. Now, let $A_j = C_1^{-1} \widehat{A}_j$. It is easy to see that $A_1 = C_1^H$. Let us define two matrices $G_1(A)$ and $G_2(A)$ as follows:

$$\begin{aligned} G_1(A) &= \begin{bmatrix} A_1 & A_2 & A_3 & \ldots & A_p \\ 0 & A_1 & A_2 & \ldots & A_{p-1} \\ \vdots & \vdots & \vdots & \vdots & \vdots \\ 0 & 0 & \ldots & A_1 & A_2 \\ 0 & 0 & \ldots & 0 & A_1 \end{bmatrix} \\ G_2(A) &= \begin{bmatrix} 0 & A_2 & A_3 & \ldots & A_p \\ 0 & 0 & A_2 & \ldots & A_{p-1} \\ \vdots & \vdots & \vdots & \vdots & \vdots \\ 0 & 0 & \ldots & 0 & A_2 \\ 0 & 0 & \ldots & 0 & 0 \end{bmatrix} \end{aligned} \tag{6.63}$$

Then,

$$A = \begin{bmatrix} G_1^H(A) & G_2^H(A) \end{bmatrix} \begin{bmatrix} I & 0 \\ 0 & -I \end{bmatrix} \begin{bmatrix} G_1^H(A) \\ G_2^H(A) \end{bmatrix} = G^H W G \tag{6.64}$$

where

$$G = \begin{bmatrix} G_1(A) \\ G_2(A) \end{bmatrix} \quad \text{and} \quad W = \begin{bmatrix} I & 0 \\ 0 & -I \end{bmatrix} \tag{6.65}$$

Now we must search for a transformation matrix U that satisfies the property $U^H W U = W$, so that $UG = R$, where R is an upper triangular matrix. Then we have:

$$\begin{aligned} A &= G^H W G = G^H U^H W U G \\ &= \begin{bmatrix} R^H & 0 \end{bmatrix} \begin{bmatrix} I & 0 \\ 0 & -I \end{bmatrix} \begin{bmatrix} R \\ 0 \end{bmatrix} = \\ &= R^H R \end{aligned} \tag{6.66}$$

that provides the factorization of A. Since matrix G comprises two upper triangular block Toeplitz matrices, considerable computational savings can be obtained by working with a generator matrix defined using the first block rows of G_1 and G_2:

$$Gen = \begin{bmatrix} A_1 & A_2 & \dots & A_{p-1} & A_p \\ 0 & A_2 & \dots & A_{p-1} & A_p \end{bmatrix} \tag{6.67}$$

As for matrix U, due to the properties required, it has to be a hyperbolic Householder transformation since it must satisfy $U^H W U = W$, where W is a diagonal matrix whose entries are either $+1$ or -1. If this property is satisfied, then U is also claimed to be a W-unitary matrix. Furthermore, if x is a column vector such that $x^H W x \neq 0$, then U can be expressed as follows:

$$U = W - \frac{2 x x^H}{x^H W x} \tag{6.68}$$

In our algorithm, we used hyperbolic Householder transformations in order to reduce the generator matrix Gen to an upper triangular matrix by successively zeroing elements below the diagonal of columns of matrix G in (6.66). So, among the possible choices of x in Equation (6.68), we would like to find the one that, given an arbitrary column vector u, satisfies

$$Uu = -\sigma e_j \tag{6.69}$$

where e_j is a column vector whose j-th element is 1 and other elements are 0, and σ is a constant value. If we assume that $e_j^H W e_j = 1$, then by choosing

$$\begin{aligned} \sigma &= \frac{u_j}{|u_j|} \sqrt{u^H W u} \\ x &= W u + \sigma e_j \end{aligned} \tag{6.70}$$

we find that U is a hyperbolic Householder transformation mapping u to $-\sigma e_j$. This transformation will be used several times in the algorithm in order to reduce matrix

G, as will be shown later. From Equation (6.66) we obtain

$$G = \begin{bmatrix} A_1 & A_1 & A_1 & A_1 & \dots & A_p \\ 0 & A_1 & A_2 & A_3 & \dots & A_{p-1} \\ 0 & 0 & A_1 & A_2 & \dots & A_{p-2} \\ 0 & 0 & 0 & A_1 & \ddots & \vdots \\ \vdots & \vdots & \vdots & \vdots & \vdots & \vdots \\ 0 & \underline{A_2} & A_3 & A_4 & \dots & A_p \\ 0 & 0 & \underline{A_2} & A_3 & \dots & A_{p-1} \\ 0 & 0 & 0 & \underline{A_2} & \dots & A_{p-2} \\ 0 & 0 & 0 & 0 & \ddots & \vdots \\ \vdots & \vdots & \vdots & \vdots & \vdots & \vdots \end{bmatrix} \tag{6.71}$$

Now, since the first column of the generator is already in the right form we can use the generator matrix starting from the second row down. The first row of the upper submatrix of the generator will represent the first block row of the triangular factor of the Toeplitz matrix. In order to achieve full factorization, the first step involves eliminating the first diagonal in the lower half of the generator matrix. The idea is to do that while preserving Toeplitz structure of the remaining portion of the matrix. In this way, we can repeat the process on the smaller generator till we fully triangularize G. Therefore, we substitute the first block row in generator matrix with the second block row of the upper submatrix:

$$Gen = \begin{bmatrix} 0 & A_1 & A_2 & \dots & A_{p-1} \\ 0 & A_2 & A_3 & \dots & A_p \end{bmatrix} \tag{6.72}$$

Now let U_1 be the block hyperbolic Householder transformation, obtained as previously outlined using vectors that have one nonzero element in their upper half and zero elements in the lower half. Thus, we can eliminate A_2 using A_1 by applying U_1 to Gen. We get

$$U_1 Gen = \begin{bmatrix} 0 & \widetilde{A}_1 & \widetilde{A}_2 & \dots & \widetilde{A}_{p-1} \\ 0 & 0 & \widetilde{A}_3 & \dots & \widetilde{A}_p \end{bmatrix} \tag{6.73}$$

Similarly, all matrices constructed by stacking the corresponding rows in the two halves of the generator matrix are shifted versions of Gen matrix in (6.72). Hence, all the work that was needed to zero out the diagonal row of A_2 in the lower submatrix was done in the first step. At this stage, the generator matrix G has a Toeplitz submatrix

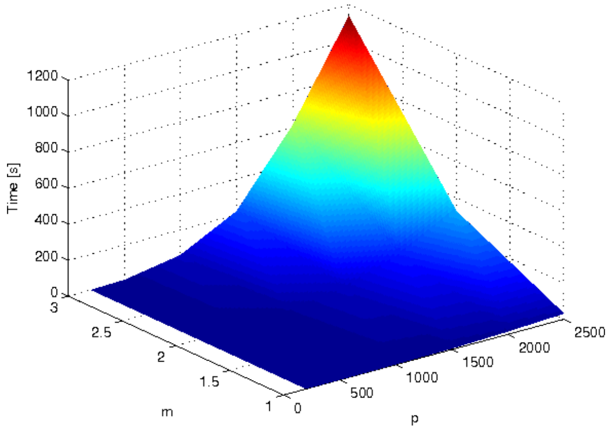

Figure 6.5: Computational time of Cholesky factorization with different values of p and m.

in its upper half and another Toeplitz submatrix in its lower half:

$$G = \begin{bmatrix} A_1 & A_2 & A_3 & A_4 & \dots & A_p \\ 0 & \widetilde{A}_1 & \widetilde{A}_2 & \widetilde{A}_3 & \dots & \widetilde{A}_{p-1} \\ 0 & 0 & \widetilde{A}_1 & \widetilde{A}_2 & \dots & \widetilde{A}_{p-2} \\ 0 & 0 & 0 & \widetilde{A}_1 & \dots & \vdots \\ \vdots & \vdots & \vdots & \vdots & \ddots & \vdots \\ 0 & 0 & \underline{\widehat{A}_3} & \widehat{A}_4 & \dots & \widehat{A}_p \\ 0 & 0 & 0 & \underline{\widehat{A}_3} & \dots & \widehat{A}_{p-1} \\ 0 & 0 & 0 & 0 & \dots & \widehat{A}_{p-2} \\ \vdots & \vdots & \vdots & \vdots & \ddots & \vdots \end{bmatrix} \qquad (6.74)$$

The second row of the upper submatrix of G is the second block row of the triangular factorization of Toeplitz matrix. The process is then repeated on the two lower right submatrices of the generator in (6.74). After $p-2$ steps the generator is completely triangularized.

Performance assessment

In order to compare the performances of Schur algorithm with respect to standard Cholesky factorization, we used both of them to factorize a $N \times N$ block Toeplitz matrix made of p blocks of size $m \times m$ on each block row, with different choices of parameters m and p. Results in Figures 6.5 - 6.6 indicates that for matrices of small size the computational time is quite the same, whereas the difference quickly becomes more relevant as parameter p increases. Then, factorization time has been measured, keeping one parameter constant and varying just the other one. What we have observed is that Cholesky factorization time has cubic convergence with respect to both parameters m and p (Figure 6.7). As a matter of fact, Cholesky algorithm

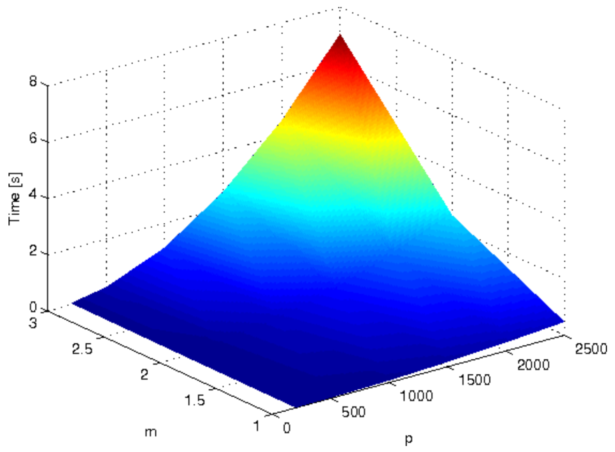

Figure 6.6: Computational time of block Toeplitz factorization with different values of p and m.

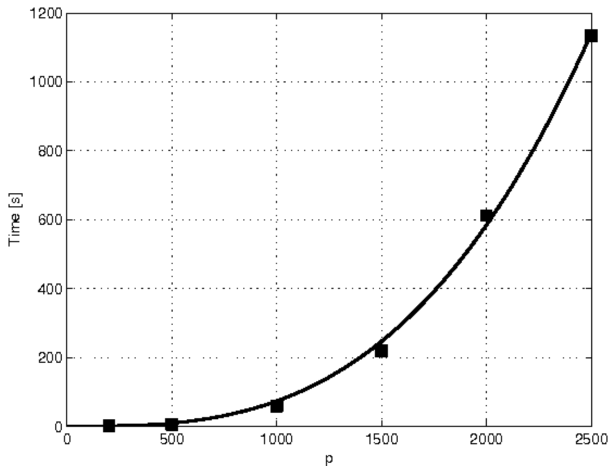

Figure 6.7: Computational time of Cholesky factorization for fixed $m = 3$, measured values (squares) and theoretical prediction Cp^3 (solid line).

does not take into account the structure of the matrix, hence it has a cubic dependence on the whole matrix dimension $N = m \times p$, as mentioned in Section 6.3.2. As for Schur factorization time, quadratical dependence has been observed on parameter p, as outlined in Figure 6.8, while time has proved to scale cubically with the block size m (Figure 6.9). This last observation is not surprising because at the beginning of Schur algorithm a Cholesky factorization step is required in order to triangularize the first block in the first block-row. However, this can not be considered a significant drawback since in the present application the size of block m is always much smaller than p, typically three orders of magnitude.

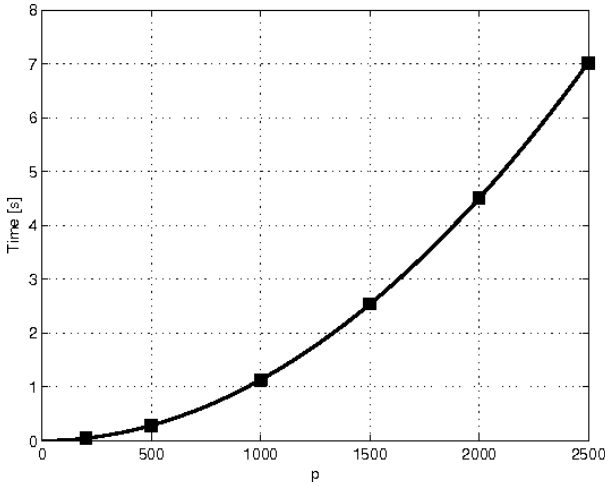

Figure 6.8: Computational time of block Toeplitz factorization for fixed $m = 3$, measured values (squares) and theoretical prediction Cp^2(solid line).

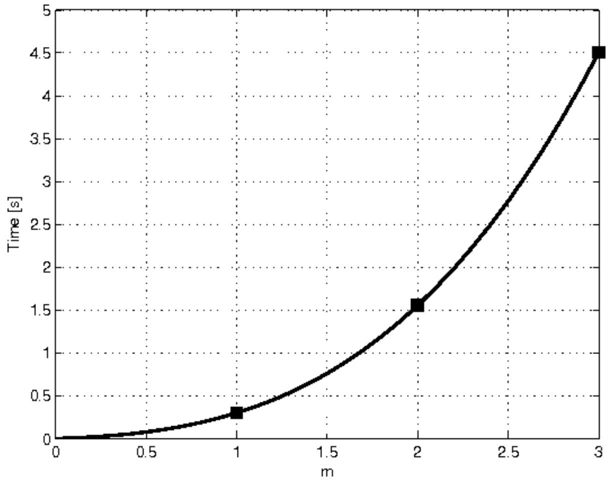

Figure 6.9: Computational time of block Toeplitz factorization for fixed $p = 2000$, measured values (squares) and theoretical prediction Cm^3 (solid line).

6.4 Impulse response measure

In order to implement Wiener-Hopf control for drag reduction in a turbulent channel flow, we need to determine the input-to-state tensorial impulse response $H_{v\,v_w}$ where the input is represented by actuator wall forcing, whereas the state vector is represented by wall-normal velocity and vorticity of the flow field. Such impulse response has been obtained with the strategy proposed in [49]. First of all, statistically stationary conditions have been considered for the turbulent flow at the same Reynolds number of the problem. Then, this flow has been perturbed through wall-normal velocity forcing v_w. Such perturbations were represented by Gaussian white noise with an amplitude of 0.000125, whose autocorrelation function reads:

$$E\{v_w(x+\Delta x,\, z+\Delta z,\, t+\Delta t)v_w(x,\, z,\, t)\} = \delta(\Delta x,\, \Delta y,\, \Delta t) \tag{6.75}$$

where δ is Dirac impulse function. Thus, as a consequence of such perturbation, state variables of the flow field could be decomposed as follows:

$$v_{TOT} = \bar{v}(x,\, y,\, z,\, t) + v(x,\, y,\, z,\, t) \tag{6.76a}$$

$$\eta_{TOT} = \bar{\eta}(x,\, y,\, z,\, t) + \eta(x,\, y,\, z,\, t) \tag{6.76b}$$

where overline indicates variables referred to the unperturbed flow field, whereas the others are related to wall forcing. Cross-correlation between input and output then reads:

$$\begin{aligned} E\{v_{TOT}(x+x',\, y,\, z+z',\, t+t')v_w^H(x',\, z',\, t')\} &= \\ &+ E\{\bar{v}(x+x',\, y,\, z+z',\, t+t')v_w^H(x',\, z',\, t')\}+ \\ &\qquad + E\{v(x+x',\, y,\, z+z',\, t+t')v_w^H(x',\, z',\, t')\} \end{aligned} \tag{6.77a}$$

$$\begin{aligned} E\{\eta_{TOT}(x+x',\, y,\, z+z',\, t+t')v_w^H(x',\, z',\, t')\} &= \\ &+ E\{\bar{\eta}(x+x',\, y,\, z+z',\, t+t')v_w^H(x',\, z'\, t')\}+ \\ &\qquad + E\{\eta(x+x',\, y,\, z+z',\, t+t')v_w^H(x',\, z',\, t')\} \end{aligned} \tag{6.77b}$$

Simplifications in (6.77) are possible by considering that no correlation exists between perturbation and unperturbed flow. Then, it is well known from signal theory that when a white noise is passed through a linear system, the cross-correlation between the input and output is proportional to the impulse response of the system, so input-to-state impulse response could be recovered by:

$$H_{x,\, v_w} = \begin{cases} H_{v\, v_w}(x,\, y,\, z,\, t) = E\{v(x+x',\, y,\, z+z',\, t+t')v_w^H(x',\, z',\, t')\} \\ H_{\eta\, v_w}(x,\, y,\, z,\, t) = E\{\eta(x+x',\, y,\, z+z',\, t+t')v_w^H(x',\, z',\, t')\} \end{cases} \tag{6.78}$$

Finally, leveraging system ergodicity led to:

$$\begin{aligned} &H_{v,\, v_w}(x,\, y,\, z,\, t) = \\ &= \frac{1}{L_x L_z}\int_0^{L_x}\int_0^{L_z}\frac{1}{T}\int_0^T v_{TOT}(x+x',\, y,\, z+z',\, t+t')v_w^H(x',\, z',\, t')\, dt'\, dx'\, dz' \end{aligned} \tag{6.79a}$$

$$\begin{aligned} &H_{\eta,\, v_w}(x,\, y,\, z,\, t) = \\ &= \frac{1}{L_x L_z}\int_0^{L_x}\int_0^{L_z}\frac{1}{T}\int_0^T \eta_{TOT}(x+x',\, y,\, z+z',\, t+t')v_w^H(x',\, z',\, t')\, dt'\, dx'\, dz' \end{aligned} \tag{6.79b}$$

With this strategy it was possible to obtain at once the whole space-time dependence of the impulse response. The numerical simulation was carried out for a turbulent channel flow at $Re = 3500$, considering a computational box having dimensions $L_x = 4\pi$,

$L_z = 4\pi/3$, while Fourier series used during FFT and IFFT transformations have been truncated at $\alpha = 96$ and $\beta = 64$ and 128 points have been used for discretization in wall-normal direction. As usual a hyperbolic tangent stretching grid was introduced. Correlations have then been measured through averaging over a time of 75000 wall-unit, considering a time step of 0.75, which is about 5 times the time step of a typical DNS at $Re = 3500$.

6.5 Results of Wiener-Hopf control for drag reduction

In order to implement a Wiener-Hopf compensator for drag reduction, impulse response is not sufficient. As a matter of fact, the knowledge of the functions of cross-correlation between the state noise and wall-measurements is required. Such statistics have been previously obtained in [52] from DNS of a turbulent channel flow at $Re = 3500$ considering the same computational domain used to measure impulse response and the same resolution for wall-normal discretization and truncation of Fourier expansions. As for time discretization, a resolution of 0.75 and a horizon of 150 wall units have been considered.

Afterwards, optimal compensators have been designed for a turbulent channel flow of size $L_x = 4\pi$, $L_z = 4\pi/3$, at $Re = 3500$ leveraging streamwise and spanwise wall shear stresses for the feedback and dissipation norm in Wiener-Hopf cost function (6.15). These choices have been motivated by results achieved in [52], where a Wiener-Hopf compensator was developed for optimal feedback of a single wall measure using two different state norms, namely turbulent kinetic energy and dissipation rate. Results showed that energy norm, which has proved to be really effective in full state control, when applied in an observer-based framework, is totally ineffective in providing drag reduction results. Furthermore, it was demonstrated that using wall pressure for feedback is equally ineffective with both state norms.

Optimal compensators have then been designed for a set of wavenumbers $\alpha \leq 12$ $-54 \leq \beta \leq 54$. Control action has been computed runtime in DNS by application of the following convolution integral:

$$\hat{v}_w(\alpha, \beta, t) = \int_0^t \widehat{K}(\alpha, \beta, \tau)\hat{m}(\alpha, \beta, t-\tau)\, d\tau \tag{6.80}$$

where $\widehat{K}$ is the impulse response of the compensator and $\hat{m}$ is the history of measurements in wavenumber space. Then, such integral has been discretized using a time resolution of 0.75 wall unit and truncated at time $T^+ = 18.75$. The spatial structure of compensator kernels obtained in this way is reported in Figures 6.10 and 6.11 for different time lags. What we can notice is that the kernel for feedback of streamwise wall shear stress is symmetric with respect to both x and z axes, whereas kernel for spanwise skin friction is symmetric for x axis and antisymmetric for z axis. Another interesting feature is that wall information required for feedback is heavily limited to

Table 6.1: Drag reduction results using SIMO Wiener-Hopf approach with different control penalties R and measurement noise covariances ϕ_{dd}.

		R		
		$2\,10^{-2}$	$3\,10^{-2}$	$4\,10^{-2}$
ϕ_{dd}	$4\,10^{-2}$	3.567	3.821	4.322
	$1\,10^{-1}$	4.467	4.567	3.891
	$2\,10^{-1}$	4.397	3.985	3.177
	$4\,10^{-1}$	2.776	3.177	2.716

the proximity of the actuator. Furthermore, by observing the sequence of frames representing kernels at different time lags, we can observe that kernel evolves downward with respect to the point of application and this is consistent with the behavior of full state convolution kernels discussed in Section 4.6.

So said, a parametric study has been carried out to find the best choice of control penalty R appearing in Wiener-Hopf formulation and the influence of measurement noise ϕ_{dd}. For this purpose, a set of more than 20 DNS have been performed using 10 AMD Opteron quad-core machines belonging to the cluster of University of Salerno. Simulations took around 4 days each for a total of 9 years of CPU time. Results have then been compared with drag reduction obtained by adopting a single-input compensator for feedback of streamwise skin friction, obtained using the scalar version of the proposed Schur factorization algorithm. What has emerged is that a maximum drag reduction of 4.6% can be achieved for $R = 0.03$ (Figure 6.12). Furthermore, such results have proved to be independent of measurement noise ϕ_{dd} for a range of covariance $4\,10^{-2} \leq \phi_{dd} \leq 5\,10^{-1}$, while for outer values performances rapidly deteriorate, as outlined in Table 6.1. As for single-output compensator, instead, a drag reduction of nearly 5.5% was observed, but performances have been showed to significantly reduce outside the range $3\,10^{-2} \leq \phi_{dd} \leq 8\,10^{-2}$. This allows the conclusion that state estimation is not improved by the use of multiple measures, but it can benefits from a higher robustness with respect to measurement uncertainty.

Finally, in order to appreciate how optimal Wiener-Hopf compensator works, in Figure 6.13 we have represented time evolution of high- and low-speed streaks. We can observe that control effectively reduces the dimensions of near-wall coherent structures. Furthermore, we can notice from Figure 6.14 that suction is applied under high-speed streaks, whereas blowing contrasts low-speed streaks. However, observer-based control reveals unable to significantly affect the regenerative process. The explanation is related to poor performances of state estimation. As a matter of fact, wall forcing appears to be applied also in portions of the flow field where no turbulent structures are present.

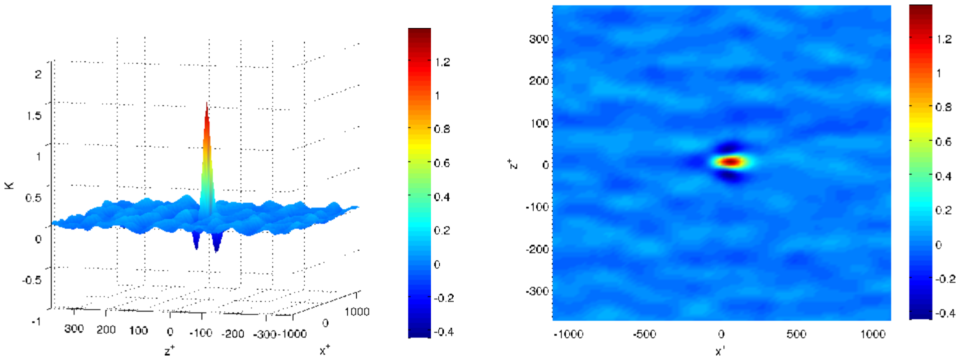

(a) *Three-dimensional view at time lag* $\tau^+ = 0$ (b) *Top view at time lag* $\tau^+ = 0$

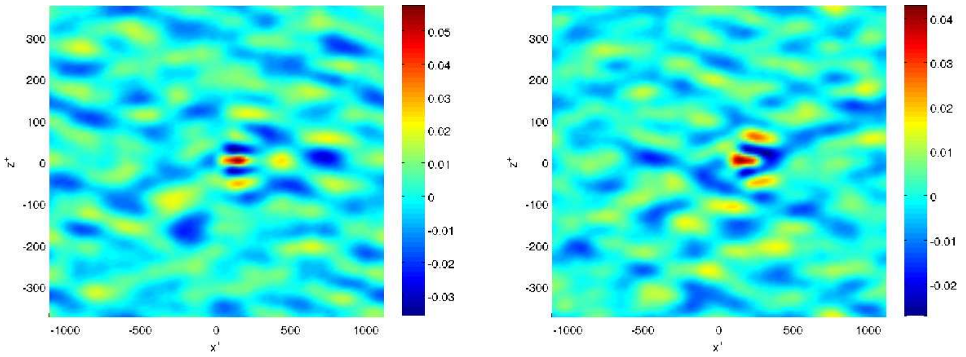

(c) *Top view at time lag* $\tau^+ = 250$ (d) *Top view at time lag* $\tau^+ = 500$

Figure 6.10: Spatial and temporal evolution of convolution kernel for SIMO streamwise wall shear stress τ_{x_w} feedback, obtained through Wiener-Hopf control design at $Re = 3500$ by using dissipation norm, $R = 0.03$ and $\phi_{dd} = 0.1$.

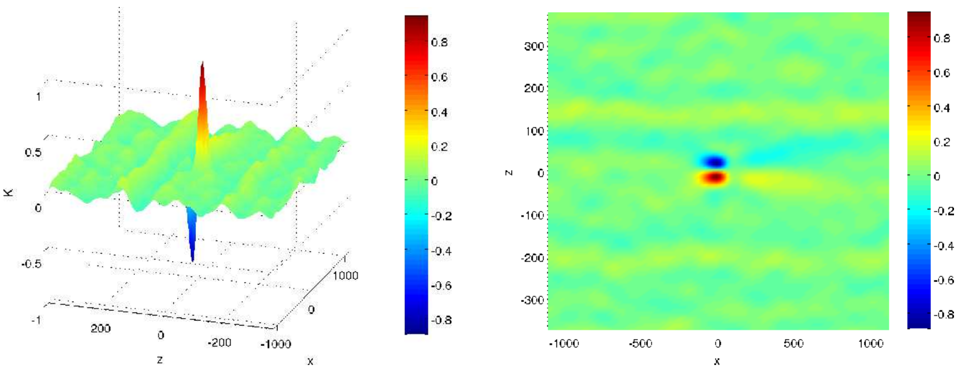

(a) *Three-dimensional view at time lag* $\tau^+ = 0$ (b) *Top view at time lag* $\tau^+ = 0$

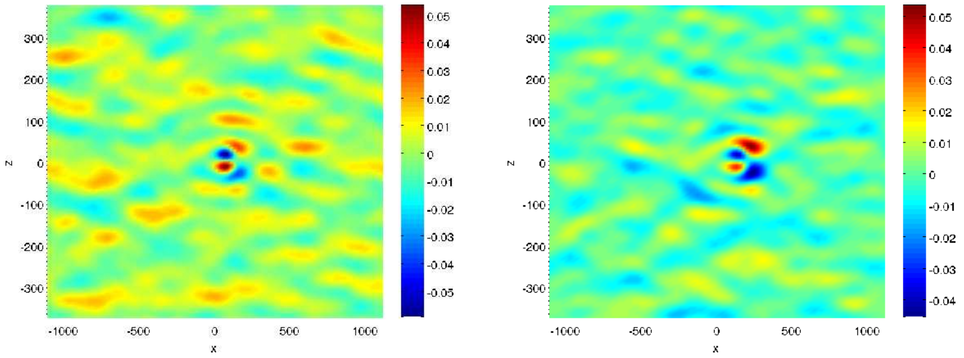

(c) *Top view at time lag* $\tau^+ = 250$ (d) *Top view at time lag* $\tau^+ = 500$

Figure 6.11: Spatial and temporal evolution of convolution kernel for SIMO spanwise wall shear stress τ_{z_w} feedback, obtained through Wiener-Hopf control design at $Re = 3500$ by using dissipation norm, $R = 0.03$ and $\phi_{dd} = 0.1$.

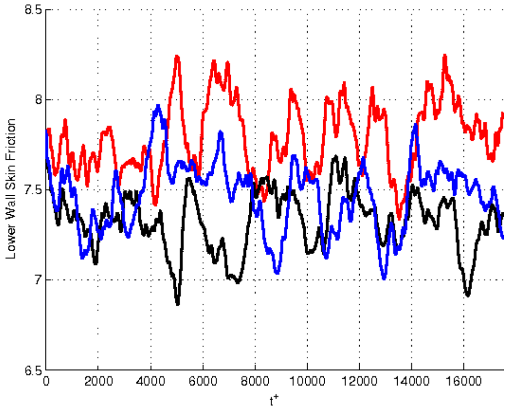

(a) *Lower wall skin friction*

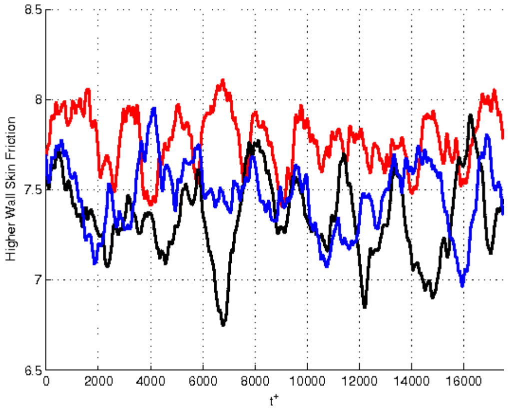

(b) *Higher wall skin friction*

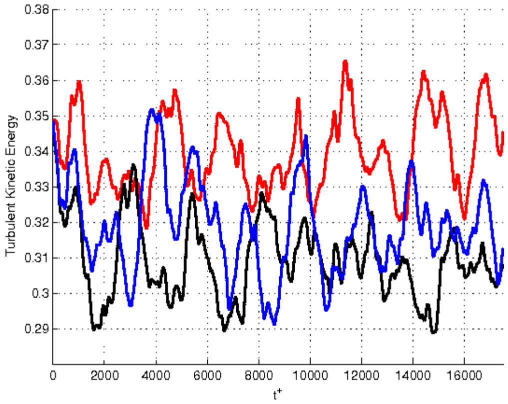

(c) *Turbulent kinetic energy*

Figure 6.12: Main statistics of the uncontrolled (red line) and controlled flow at $Re = 3500$ using dissipation norm for the feedback of streamwise wall shear stress (black line) and both stresses(blue line) with the best choice of control parameters.

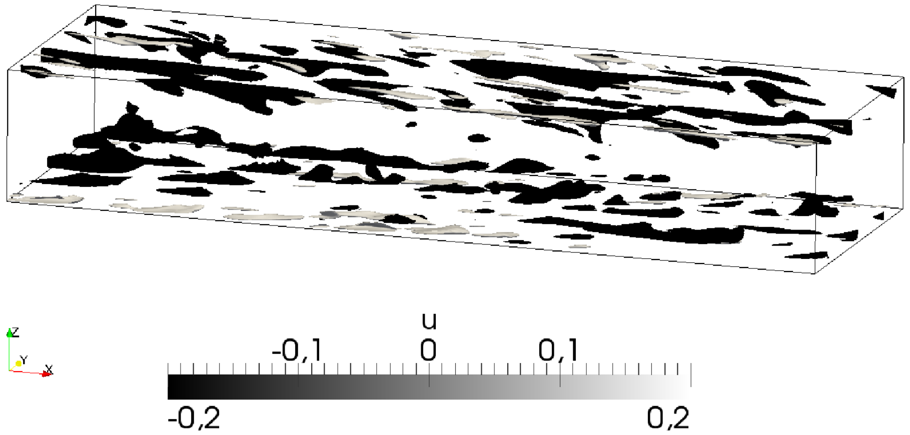

(a) *Initial flow state*

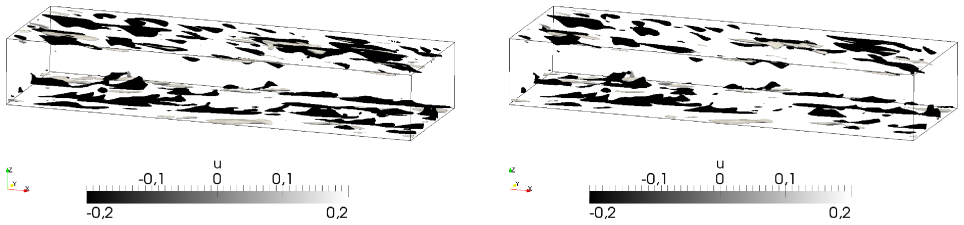

(b) *Uncontrolled flow at* $t^+ = 250$ **(c)** *Controlled flow at* $t^+ = 250$

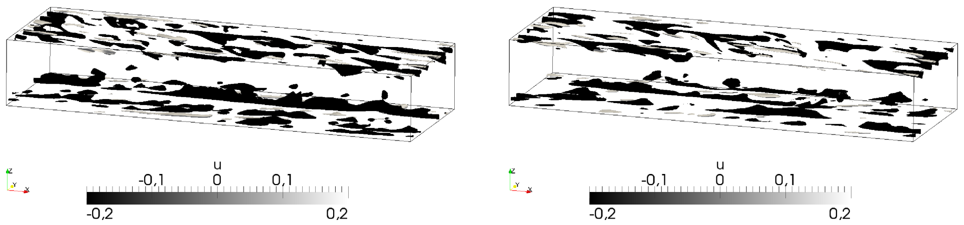

(d) *Uncontrolled flow at* $t^+ = 750$ **(e)** *Controlled flow at* $t^+ = 750$

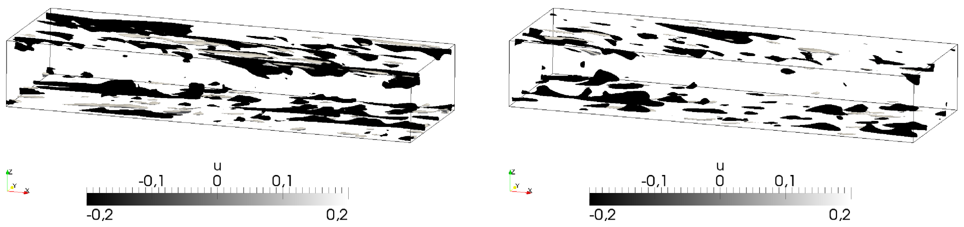

(f) *Uncontrolled flow at* $t^+ = 2500$ **(g)** *Controlled flow at* $t^+ = 2500$

Figure 6.13: Three-dimensional view of a turbulent channel flow uncontrolled and controlled with SIMO Wiener-Hopf compensator at $Re = 3500$ by using dissipation norm, $R = 0.03$ and $\phi_{dd} = 0.1$: visualized are high- (light) and low- (dark) speed streaks at 30% of bulk velocity.

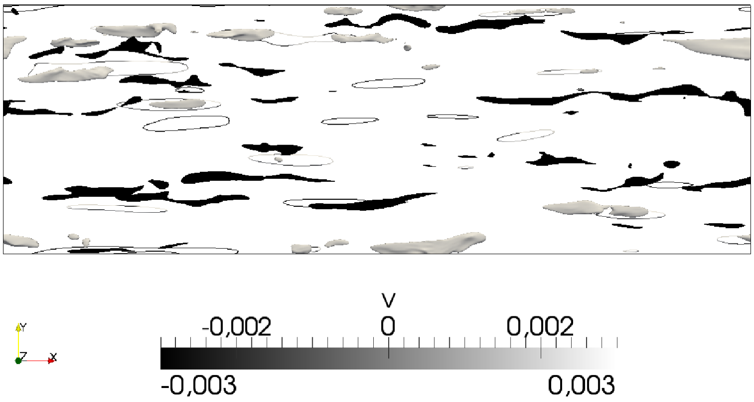

(a) *Frame at* $t^+ = 250$

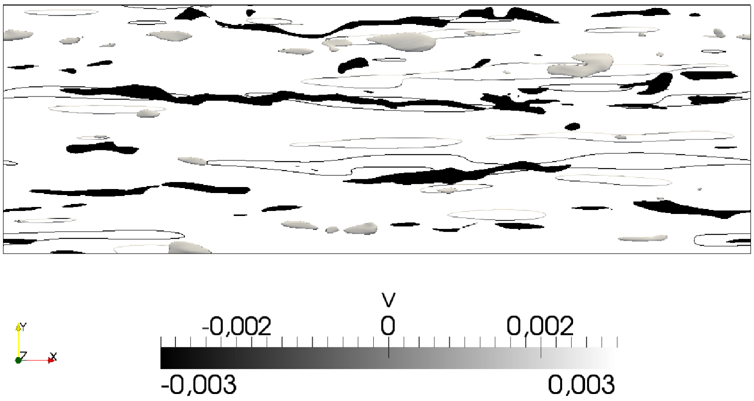

(b) *Frame at* $t^+ = 750$

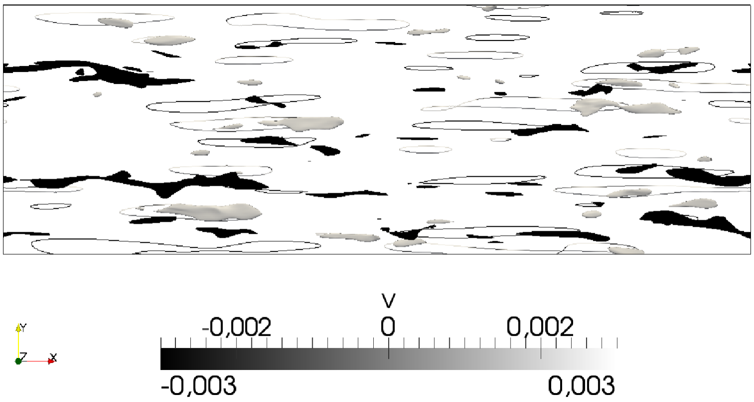

(c) *Frame at* $t^+ = 2500$

Figure 6.14: Top view at different time steps of the lower half of a turbulent channel flow uncontrolled and controlled with SIMO Wiener-Hopf approach at $Re = 3500$ by using dissipation norm, $R = 0.03$ and $\phi_{dd} = 0.1$: visualized are high- (light) and low- (dark) speed streaks at 30% of bulk velocity. At wall control actuation is represented by contours graduated according to the legend.

Chapter 7

Conclusions and Future Developments

The present work has addressed the problem of reducing the friction drag in a turbulent channel flow, by applying optimal feedback control through zero-net-mass-flux blowing/suction MEMS actuators and sensors at walls. Our results have shown that when knowledge of the whole flow state is available, optimal control leads to very good performances, provided an optimal set of tuning parameters is adopted. The most important conclusion is that the norm of the state used in the definition of optimal control cost function has a strong impact on the overall performances, with the norm based on turbulent kinetic energy yielding the best results. Moreover, Direct Numerical Simulations carried out at $Re = 1500$ with feedback control applied through wall boundary conditions have succeded in achieving full relaminarization. As far as we know, this result has been obtained with a constant-gain LQR controller for the first time in this work. Furthermore, this outcome has been demonstrated to be independent of the initial conditions of the flow field and of saturation effects of the MEMS actuators. Then, for a higher Reynolds number, namely $Re = 3500$, relevant drag and net drag reduction was achieved using the same norm in a slightly modified fashion. Besides, results have been proved to be independent of the choice of control penalty in optimal control cost function, suggesting that for higher Reynolds numbers the effect of nonlinearities strongly limits the performances of linear controllers.

Then, we have turned to considering a control scheme in a more realistic scenario, i.e. where wall-measurement information alone is available. The first attempt has concerned the design of a compensator based on optimal output feedback control theory. Results based on H_2 and H_∞ norms of disturbance-to-state transfer functions have shown that the performances are quite limited if compared to LQR control approach. For this reason, the implementation of a state observer was made necessary. Therefore, a frequency-based Wiener-Hopf approach has been followed for the design of a single-input multi-output compensator for the feedback of streamwise and spanwise wall shear stresses using dissipation norm of the state, which has proved to perform better than energy norm in an observer-based control framework. The approach uses a properly defined and measured impulse response of the system as the system model. A fast Schur solver has been developed in order to efficiently factorize the block Toeplitz matrix of the linear system arising from time discetization of the associated Wiener-Hopf matrix equation. Results have shown that performances degrade significantly with respect to full-information control. Furthermore, comparison with an optimal compensator exploiting just streamwise skin friction revealed that SIMO compensator leads to the same drag reduction but it benefits from a higher robustness with respect to the measurement noise.

The limitations of optimal linear control theory applied to turbulent drag reduction have been underlined throghout this work. We think that future developments are possible only by abandoning linear system theory, e.g. by considering a feedback linearization of the nonlinear terms neglected by the linear representation of the flow. As for the design of a compensator based on wall measurements, performances have been proved to be strongly affected by the time span used for the discretization of the Wiener-Hopf equation. Hence, it would be of interest to consider a smaller time step, even though this would result in a significantly higher computational cost during the phase of kernel design. Moreover, we suggest that further improvements are possible by accounting for the actual nonlinear impulse response of the flow subject to wall-forcing. As a matter of fact, in the present work only the linear part has been considered, which corresponds in Wiener nonlinear systems theory to the first-order convolution kernel relating system input to system output. Then, knowledge of higher-order Wiener kernels can be straightforwardly accounted for in Wiener-Hopf optimal control theory, leading to kernels which are optimal for the actual turbulent flow.

Appendix A

Proof of Bewley Conjecture

In [3] it has been conjectured that the lowest sustainable drag of an incompressible constant mass-flux channel flow, when controlled via a distribution of zero-net-mass-flux blowing/suction over a no-slip channel walls, is exactly that of the laminar flow. The proof of this conjecture starts with the definition of the sustainable drag ([4]):

$$\langle D\rangle_\infty = \lim_{T\to\infty} \langle D(t)\rangle_T = \lim_{T\to\infty} \int_0^T \frac{1}{T}\int_0^T D(t)\,dt = \lim_{T\to\infty} -\frac{\mu}{T}\int_0^T \int_{\Gamma_2^\pm} \frac{\partial u}{\partial n}\,d\mathbf{x}\,dt \quad (A.1)$$

where n is the wall-normal, $\Gamma_2^\pm$ is the boundary set grouping upper and lower walls. Then, incompressible Navier-Stokes equations are considered, highlighting the mean pressure gradient P_x:

$$\begin{cases} \dfrac{\partial \mathbf{U}}{\partial t} + u\nabla\mathbf{U} = \nabla P + iP_x + \Delta\mathbf{U} & \text{(A.2a)} \\ \nabla\mathbf{U} = 0 & \text{(A.2b)} \end{cases}$$

where i indicates unit vector in streamwise direction. The mean pressure gradient in the streamwise direction is then chosen so to maintain a constant bulk velocity:

$$U_B = \frac{1}{V}\int_\Omega \mathbf{U}(\mathbf{x},\, t)\,d\mathbf{x} = \text{constant} \quad (A.3)$$

where Ω is the rectangular domain of the problem $(0,\, L_x)\times(-1,\, 1)\times(0,\, L_z)$ and $V = 2L_xL_z$ is the volume of such domain. Then, we choose the laminar Poiseuille solution for the reference velocity profile $U(y)$. Blowing/suction control can be analytically represented as $u(x,\, t) = -\phi(\mathbf{x},\, t)\, n$. So, by integrating Navier-Stokes equations over space multiplied by velocity U, then integrating by parts, applying boundary conditions and finally taking the time average, we find an expression for $\langle D\rangle_\infty$:

$$\langle D\rangle_\infty U_B V = \langle \nu\|\nabla U\|_2^2\rangle_\infty - \left\langle \int_{\Gamma_2^\pm} \phi(p + \phi^2/2)\,dx \right\rangle_\infty \quad (A.4)$$

where the quantity $\left\langle \int_{\Gamma_2^\pm} \phi(p+\phi^2/2)\,dx \right\rangle_\infty$ is the time-averaged power input applied at walls, while the quantity $\langle D\rangle_\infty U_B V$ represents the time-averaged power required to maintain the unsteady controlled flow by the bulk pressure gradient. If we now consider the laminar drag D_L of the corresponding laminar channel flow with the same dimensions, viscosity and bulk velocity, then by integrating the wall-normal derivative of the laminar velocity profile, i.e. $\bar{U}(y)$ over Ω, we find:

$$D_L U_B V = \nu L_x L_z \int_{-1}^{1} U'^2\,d\mathbf{x} \tag{A.5}$$

where the quantity $D_L U_B V$ may be interpreted as the power required to maintain the laminar flow by the bulk pressure gradient. Finally, we split the velocity field in Navier-Stokes equations in its mean and fluctuating components, namely $\bar{\mathbf{U}}$ and $\mathbf{u}$, then, following the same analytical manipulations that led to A.4, we find

$$\|\nabla\mathbf{U}\|_2^2 = L_x L_z \int_{-1}^{1} U'^2 dy + \|\mathbf{u}\|_2^2 \tag{A.6}$$

After combining Equations A.4, A.5 and A.6, we come to the fundamental relation, which has appeared for the first time in [8]:

$$\left\langle \int_{\Gamma_2^\pm} \phi(p+\phi^2/2)dx \right\rangle_\infty - [D_L U_B V] = \left\langle \nabla\mathbf{v}_2^2 \right\rangle_\infty > 0 \tag{A.7}$$

A quick analysis of A.7 allows us to assert that when $\langle D\rangle_\infty < D_L$, i.e. sublaminar drag is achieved, then the power of the applied control input is always larger than any possible power saved due to drag reduction for any possible control distribution $\phi(\mathbf{x}, t)$. For this reason relaminarization is the highest result that can be achieved through blowing/suction wall actuation with a positive net power saving.

Ringraziamenti

Concludo ringraziando, nella lingua che più apre il cuor della gente, tutte quelle persone che in questi anni mi hanno sostenuto ed aiutato e senza le quali oggi non sarei quello che sono.

Voglio ringraziare il professor Maurizio Quadrio per il continuo supporto, l'amicizia e la disponibiltà mostrata durante tutta l'attività di tesi, ma sopra tutte queste cose lo ringrazio per l'influenza che ha avuto sulla mia crescita professionale, progredita di pari passo con lo sviluppo di questo lavoro. Allo stesso modo voglio ringraziare Fulvio per i continui confronti e scambi di idee. In più gli auguro una brillante carriera, ne ha tutte le facoltà. Ringrazio inoltre il professor Paolo Luchini, che non ho avuto la fortuna di conoscere personalmente ma che ha messo a dispozione le risorse di calcolo dell'Università di Salerno. Ringrazio poi l'ingegner Francesco Braghin, che al contrario conosco molto bene, per la disponibilità mostrata ogni volta.

Un ringraziamento immenso va poi alla mia famiglia, in particolar modo ai miei genitori, i quali non hanno mai mancato di sostenere in ogni modo le mie scelte e senza i cui sacrifici non avrei raggiunto tutti i miei traguardi ed avuto quella vita serena e felice che finora mi è stata concessa. Per tutto questo, e per tanto altro, non finirò mai di esservi debitore. Ringrazio poi i miei fratelli, Davide e Lorenzo, per le giornate passate in allegria ed auguro loro una vita sfolgorante e piena soddisfazioni.

Ringrazio infine tutti i miei amici, quelle persone speciali che sanno farti divertire in ogni attimo della giornata e risollevare il morale nei momenti più grigi. Voglio ringraziare Mitch per il supporto di alto livello tanto nei momenti di cazzeggio quanto in quelli di grande sbattimento. A lui auguro una vita al top, perché la classe non è acqua. Allo stesso modo ringrazio Gennaro, compagno di studi e scorribande nonché insostituibile amico, perché sa sempre strappare un sorriso, a volte anche solo con una parola. Un grazie va anche a Giuseppe, per le interminabili chiacchierate notturne e perché dalle casse del suo pc non esce nulla che non sia un pezzo rap. In una parola, yo. Ringrazio poi gli amici del paese, il Casta, Michele e la Marina su tutti, perché sin dall'infanzia li ricordo sempre al mio fianco e mi scuso con loro per essere mancato troppe volte di questi tempi. Recupereremo, non preoccupatevi. Ringrazio poi Enrico per la sua grande amicizia e per quel suo sorrisone scacciapensieri che ha sempre stampato sul viso.

Un ringraziamento va infine ai miei coinquilini, Domenico e Marco, che con pazienza infinita hanno sopportato gli orari folli che ho tenuto in questi mesi. Dico solo che con voi mi sono sempre sentito come a casa. Allo stesso modo voglio ringraziare gli amici del Collegio di Milano per i tre fantastici anni passati insieme.

E più mi guardo indietro più mi accorgo che se questi anni sono volati è anche grazie a voi. E' a tutti voi quindi che va quindi un profondo e sincero grazie.

Bibliography

[1] L. Ahlfors. *Complex Analysis.* Mc Graw-Hill, 1979.

[2] Bartels. R. and Stewart. G. Solution of the matrix equation AX +XB = C. *Comm. ACM*, 15:820–826, 1972.

[3] T. Bewley. Flow Control: New Challenges for a New Renaissance. *Prog. Aerosp. Sci.*, 37:21–58, 2001.

[4] T. Bewley and O.M. Aamo. A 'win-win' mechanism for low-drag transients in controlled two-dimensional channel flow and its implications for sustained drag reduction. *J. Fluid Mech.*, 499:183–196, 2004.

[5] T. Bewley, P. Moin, and R. Temam. DNS-based predictive control of turbulence: an optimal benchmark for feedback algorithms. *J. Fluid Mech.*, 447:179–225, 2001.

[6] T. Bewley and B. Protas. Skin friction and pressure: the "footprints" of turbulence. *Physica D*, 2004.

[7] T. R. Bewley and S. Liu. Optimal and robust control and estimation of linear paths to transition. *J. Fluid Mech.*, 365:305–349, 1998.

[8] T.R. Bewley. A fundamental limit on the balance of power in a transpiration-controlled channel flow. *J. Fluid Mech.*, 632:443–446, 2009.

[9] K.S. Breuer, J. Park, and C. Henoch. Actuation and control of a turbulent channel flow using Lorentz forces. *Phys. Fluids*, 16(4):897–907, 2004.

[10] C. Canuto, M.Y. Hussaini, A. Quarteroni, and T.A. Zang. *Spectral Methods in Fluid Dynamics.* Springer-Verlag, Berlin, Germany, 1988.

[11] M. Chevalier, J. Höpffner, T. R. Bewley, and D.S. Henningson. State estimation in wall-bounded flow systems. Part 2. Turbulent flows. *J. Fluid Mech.*, 552:167–187, 2006.

[12] H. Choi, P. Moin, and J. Kim. Active turbulence control for drag reduction in wall-bounded flows. *J. Fluid Mech.*, 262:75–110, 1994.

[13] K.-S. Choi. Near-wall structure of turbulent boundary layer with spanwise-wall oscillation. *Phys. Fluids*, 14(7):2530–2542, 2002.

[14] K-S. Choi and M. Graham. Drag reduction of turbulent pipe flows by circular-wall oscillation. *Phys. Fluids*, 10(1):7–9, 1998.

[15] B. N. Datta. *Numerical Methods for Linear Control Systems.* Elsevier, 2004.

[16] Y. Du and G. E. Karniadakis. Suppressing Wall Turbulence by Means of a Transverse Traveling Wave. *Science*, 288:1230–1234, 2000.

[17] Y. Du, V. Symeonidis, and G. E. Karniadakis. Drag reduction in wall-bounded turbulence via a transverse travelling wave. *J. Fluid Mech.*, 457:1–34, 2002.

[18] R.E. Falco. The Production of Turbulence Near a Wall. *AIAA Paper No. 80-1356, New York*, 1980.

[19] R.P. Feynman. *Miniaturization.* Reinhold Publishing, New York, 1961.

[20] M. Gad-el Hak. *Flow Control – Passive, Active and Reactive Flow Management.* Cambridge University Press, Cambridge, 2000.

[21] M. Gad-el Hak. *The MEMS Handbook.* CRC Press, 2002.

[22] M. Gad-el Hak, R.F. Blackwelder, and J.J. Riley. *Visualization Techniques for Studying Transitional and Turbulent Flows*, volume Flow Visualization III. Hemisphere, Washington, D.C., 1985.

[23] M. Grant and S. Boyd. CVX: Matlab software for disciplined convex programming. 2010.

[24] A. Hanifi, P.J. Schmid, and D.S. Henningson. Transient Growth in compressible boundary layer flow. *Phhys. Fluids*, 8:826–836, 1996.

[25] M. Högberg, T.R. Bewley, and D. Henningson. Linear feedback control and estimation of transition in plane channel flow. *J. Fluid Mech.*, 481:149–175, 2003.

[26] M. Högberg, T.R. Bewley, and D. Henningson. Relaminarization of $Re_\tau = 100$ turbulence using gain scheduling and linear state-feedback control. *Phys. Fluids*, 15(11):3572–3575, 2003.

[27] J. Höpffner, M. Chevalier, T. R. Bewley, and D.S. Henningson. State estimation in wall-bounded flow systems. Part 1. Perturbed laminar flows. *J. Fluid Mech.*, 534:263–294, 2005.

[28] W. Huang and D. M. Sloan. The Pseudospectral Method for Solving Differential Eigenvalue Problems. *Journal Comp. Phys.*, 111:399–409, 1994.

[29] N. Hutchins and I. Marusic. Large-Scale influences in near-wall turbulence. *Phil. Trans. R. Soc. Lond.*, 365:647–664, 2007.

[30] Stuart A. Jacobson and William C. Reynolds. Active control of streamwise vortices and streaks in boundary layers. *Journal of Fluid Mechanics*, 360:179–211, 1998.

[31] S.S. Joshi, J.L. Speyer, and J. Kim. A system theory approach to the feedback stabilization of infinitesimal and finite-amplitude perturbations in plane Poiseuille flow. *J. Fluid Mech.*, 332:157–184, 1997.

[32] S.S. Joshi, J.L. Speyer, and J. Kim. Finite-dimensional optimal control of Poiseuille flow. *J. Guidance, Control, Dynamics*, 22:340–348, 1999.

[33] K.A. Gallivan, S. Thirumalai, P. Van Dooren, and V. Vermaut. High performance algorithms for Toeplitz and block Toeplitz matrices. *Linear algebra and its applications*, 1996.

[34] G.E. Karniadakis and K.-S. Choi. Mechanisms on Transverse Motions in Turbulent Wall Flows. *Ann. Rev. Fluid Mech.*, 35:45–62, 2003.

[35] N. Kasagi, Y. Suzuki, and K. Fukagata. Microelectromechanical systems-based feedback control of turbulence for drag reduction. *Annu. Rev. Fluid Mech.*, 41:231–251, 2009.

[36] J. Kim and J. Lim. A linear process in wall-bounded turbulent flows. *Phys. Fluids*, 12(8):1885–1888, 2000.

[37] J. Kim, P. Moin, and R. Moser. Turbulence statistics in fully developed channel flow at low Reynolds number. *J. Fluid Mech.*, 177:133–166, 1987.

[38] L. Cortelezzi and J. Speyer. Robust reduced-order controller of laminar boundary layer transition. *Phys. Rev. E*, 1998.

[39] F. Laadhari, L. Skandaji, and R. Morel. Turbulence reduction in a boundary layer by a local spanwise oscillating surface. *Phys. Fluids*, 6 (10):3218–3220, 1994.

[40] A.J. Laub. A Schur method for solving algebraic Riccati equations. *IEEE Trans. Autom. Control*, AC-24:913–921, 1979.

[41] C. Lee, J. Kim, D. Babcock, and R. Goodman. Application of neural networks to turbulence control for drag reduction. *Phys. Fluids*, 9:1740–1747, 1997.

[42] K.H. Lee, L. Cortelezzi, J. Kim, and J. Speyer. Application of reduced-order controller to turbulent flows for drag reduction. *Phys. Fluids*, 13(5), 2001.

[43] T. Lee, M. Fisher, and W:H. Schwarz. Inverstigation of the Effects of a Compliant Surface on Boundary-Layer Stability. *J. Fluid Mech.*, (288):37–58, 1995.

[44] S.K. Lele. Compact Finite Difference Schemes with Spectral-like Resolution. *J. Comp. Phys.*, 103:16–42, 1992.

[45] W.S. Levine and Athans M. On the Determination of the optimal constant output feedback gains for linear multivariable systems. *IEEE Trans. Autom. Control*, AC-15(1):44–48, 1970.

[46] W.S. Levine, T.L. Johnson, and M. Athans. Optimal limited state variable feedback controllers for linear systems. *IEEE Trans. Autom. Control*, 16(6):785–793, 1971.

[47] C. Liu, T. Tsao, G.B. Lee, J. Leu, and Y. Yi. Out-of-plane magnetic actuators with electroplated permalloy for fluid dynamics control. *Sens. Actuators*, 78:190–197, 1999.

[48] P. Luchini and M. Quadrio. A low-cost parallel implementation of direct numerical simulation of wall turbulence. *J. Comp. Phys.*, 211(2):551–571, 2006.

[49] P. Luchini, M. Quadrio, and S. Zuccher. Phase-locked linear response of a turbulent channel flow. *Phys. Fluids*, 18(121702):1–4, 2006.

[50] J.L. Lumley. Drag Reduction in Turbulent Flow by Polymer Additives. *J. Polym. Sci.*, 7:263–290, 1973.

[51] J.L. Lumley. Drag reduction in two-phase and polymer flows. *Physics of Fluids*, 20(10):64–71, 1977.

[52] F. Martinelli. *Feedback Control of Turbulent Wall Flows.* PhD thesis, Department of Aerospace Engineering, Politecnico di Milano, 2009.

[53] F. Martinelli, M. Quadrio, and P. Luchini. Wiener-Hopf design of feedback compensators for drag reduction in turbulent channels. XX AIDAA Conference, 2009.

[54] R. Mathis, N. Hutchins, and I. Marusic. Large-scale amplitude modulation of the small-scale structures in turbulent boundary layers. *J. Fluid Mech.*, 2009.

[55] T. Min, S.M. Kang, J.L. Speyer, and J. Kim. Sustained sub-laminar drag in a fully developed channel flow. *J. Fluid Mech.*, 558:309–318, 2006.

[56] B. Noble. *Methods based on the Wiener-Hopf technique for solution of partial differential equations.* International series of monographs in pure and applied mathematics. Pergamon press, 1958.

[57] J. Pang and K.-S. Choi. Turbulent drag reduction by Lorentz force oscillation. *Phys. Fluids*, 16(5):L35–L38, 2004.

[58] T. Penzl. A cyclic low-rank Smith Method for large sparse Lyapunov Equations. *SIAM, J. Sci. Comput.*, 21(4):1401–1418, 2000.

[59] M. Quadrio, F. Auteri, A. Baron, M. Belan, and A. Bertolucci. Experimental assessment of turbulent drag reduction by wall traveling waves. In B. Eckhardt, editor, *Advances in Turbulence XII, Proc. 12th EUROMECH Eur. Turbul. Conf.*, volume 132. Springer Proceedings in Physics, 2009.

[60] M. Quadrio and P. Ricco. The laminar generalized Stokes layer and turbulent drag reduction. *Submitted to J. Fluid Mech.*, 2010.

[61] M. Quadrio, P. Ricco, and C. Viotti. Streamwise-traveling waves of spanwise wall velocity for turbulent drag reduction. *J. Fluid Mech.*, 627:161–178, 2009.

[62] R. Rathnasingham and K.S. Breuer. Active control of turbulent boundary layers. *J. Fluid Mech.*, 495:209–233, 2003.

[63] P. Ricco and M. Quadrio. Wall-oscillation conditions for drag reduction in turbulent channel flow. *Int. J. Heat Fluid Flow*, 29:601–612, 2008.

[64] S. K. Robinson. Coherent motions in the turbulent boundary layer. *Ann. Rev. Fluid Mech.*, 23:601–639, 1991.

[65] P.J. Schmid and D.S. Henningson. *Stability and Transition in Shear Flows.* Springer, 2001.

[66] W. Schoppa and F. Hussain. Coherent structure generation in near-wall turbulence. *J. Fluid Mech.*, 453:57–108, 2002.

[67] G. Schrauf. Key Aerodynamic Technologies for Aircraft Performance Improvement. In 5th Community Aeronautics Days, 2006.

[68] D. Simon. *Optimal State Estimation Kalman H Infinity and Nonlinear Approaches.* John Wiley & Sons, 2006.

[69] R. A. Smith. Matrix Equation XA+BX=C. *SIAM J. Appl. Math.*, 16(1), 1968.

[70] L.H. Thomas. The stability of plane Poiseuille flow. *Phys. Rev.*, 91(4):780–783, 1953.

[71] F. Waleffe. Exact Coherent Structures in Channel Flow. *J. Fluid. Mech.*, 435:93–102, 2001.

[72] J.A.C. Weideman and S.C. Reddy. A Matlab Differentiation Matrix Suite. *ACM Trans. Math. Soft.*, 26(4):465–519, 2000.

[73] T. Yamagami, Y. Suzuki, and N. Kasagi. Development of feedback control system of wall turbulence using MEMS devices. In *Proc. 6th Symp. Smart Control Turbul.*, pages 135–141, Tokyo: Cent. Smart Control Turbul., 2005.

[74] T. Yoshino, Y. Suzuki, and N. Kasagi. Feedback control of turbulence air channel flow with distributed micro-sensors and actuators. *J. Fluid Sci. Technol.*, 3:137–148, 2008.

[75] D.C. Youla, J.J. Bongiorno, and H.A. Jabr. Modern Wiener-Hopf design of Optimal Controllers. Part I: The Single-Input-Output Case. *IEEE Trans. Autom. Control*, ac-21(1):3–13, 1976.

[76] D.C. Youla, H.A. Jabr, and J.J. Bongiorno. Modern Wiener-Hopf design of Optimal Controllers. Part II: The Multivariable Case. *IEEE Trans. Autom. Control*, ac-21(3):319–338, 1976.